



UvA-DARE (Digital Academic Repository)

Characterizations of many-body localization

Buijsman, W.

Publication date

2021

Document Version

Final published version

License

Other

[Link to publication](#)

Citation for published version (APA):

Buijsman, W. (2021). *Characterizations of many-body localization*. [Thesis, fully internal, Universiteit van Amsterdam].

General rights

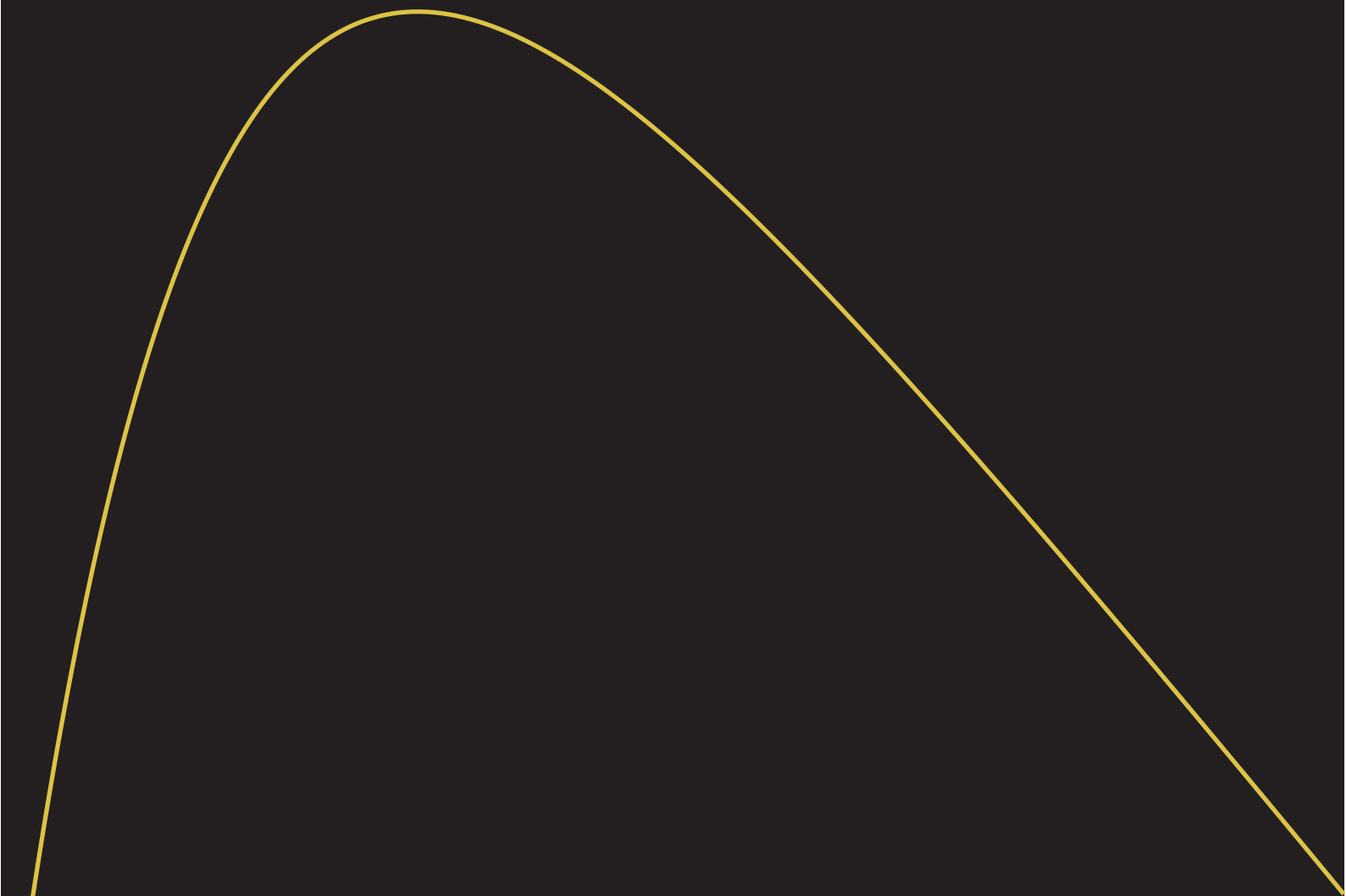
It is not permitted to download or to forward/distribute the text or part of it without the consent of the author(s) and/or copyright holder(s), other than for strictly personal, individual use, unless the work is under an open content license (like Creative Commons).

Disclaimer/Complaints regulations

If you believe that digital publication of certain material infringes any of your rights or (privacy) interests, please let the Library know, stating your reasons. In case of a legitimate complaint, the Library will make the material inaccessible and/or remove it from the website. Please Ask the Library: <https://uba.uva.nl/en/contact>, or a letter to: Library of the University of Amsterdam, Secretariat, Singel 425, 1012 WP Amsterdam, The Netherlands. You will be contacted as soon as possible.

Characterizations of many-body localization

Wouter Buijsman

A yellow parabolic curve is drawn on a black background. The curve starts at the bottom left, rises to a peak, and then descends towards the bottom right. The peak is located in the upper left quadrant of the lower half of the page.

Characterizations of many-body localization

Characterizations of many-body localization

ACADEMISCH PROEFSCHRIFT

ter verkrijging van de graad van doctor

aan de Universiteit van Amsterdam

op gezag van de Rector Magnificus

prof. dr. ir. K.I.J. Maex

ten overstaan van een door het College voor Promoties ingestelde commissie,

in het openbaar te verdedigen in de Agnietenkapel

op donderdag 14 januari 2021, te 10:00 uur

door

Wouter Buijsman

geboren te Hoorn

Promotiecommissie

Promotor:	prof. dr. J.-S. Caux	Universiteit van Amsterdam
Copromotores:	dr. V. Gritsev	Universiteit van Amsterdam
	dr. V. Cheianov	Universiteit Leiden
Overige leden:	prof. dr. M.S. Golden	Universiteit van Amsterdam
	prof. dr. C.J.M. Schoutens	Universiteit van Amsterdam
	prof. dr. C.W.J. Beenakker	Universiteit Leiden
	dr. R. Sprik	Universiteit van Amsterdam
	dr. M.S.M. Titov	Radboud Universiteit Nijmegen

Faculteit der Natuurwetenschappen, Wiskunde en Informatica

List of publications

This dissertation is based on the following publications:

- [1] W. Buijsman, V. Gritsev, and V. Cheianov, Many-body localization in the Fock space of natural orbitals, *SciPost Phys.* **4**, 038 (2018).
- [2] W. Buijsman, V. Cheianov, and V. Gritsev, Random Matrix Ensemble for the Level Statistics of Many-Body Localization, *Phys. Rev. Lett.* **122**, 180601 (2019).
- [3] W. Buijsman, V. Gritsev, and V. Cheianov, Gumbel statistics for entanglement spectra of many-body localized eigenstates, *Phys. Rev. B* **100**, 205110 (2019).

Other publications by the author:

- [4] W. Buijsman and M. Sheinman, Efficient fold-change detection based on protein-protein interactions, *Phys. Rev. E* **89**, 022712 (2014).
- [5] W. Buijsman, V. Gritsev, and R. Sprik, Nonergodicity in the Anisotropic Dicke Model, *Phys. Rev. Lett.* **118**, 080601 (2017).

Contents

1	Preface	4
1.1	Setting the stage	4
1.2	Outline and main results	4
1.3	Conventions and notations	5
2	Many-body localization	6
2.1	Introduction	6
2.2	Anderson localization	6
2.3	From Anderson to many-body localization	8
2.4	Phenomenology of many-body localization	9
2.5	Signatures of many-body localization	10
2.6	Standard model of many-body localization	13
3	Random matrix theory	15
3.1	Introduction	15
3.2	Gaussian invariant ensembles	15
3.3	Eigenvalue statistics	17
3.4	Circular ensembles	20
3.5	Probing eigenvalue statistics	21
3.6	Fixed-trace Wishart ensembles	25
4	Level statistics across the many-body localization transition	29
4.1	Introduction	29
4.2	Literature review	30
4.3	Gaussian beta ensemble	32
4.4	Eigenvalue statistics for intermediate beta	33
4.5	Agreement with intermediate level statistics	35
4.6	Breaking time-reversal symmetry	42
4.7	Longer-range statistics	45

4.8	Discussion and outlook	49
5	Spectral form factor and level repulsion	51
5.1	Introduction	51
5.2	Spectral form factor	51
5.3	Constraint by level repulsion	53
5.4	Thouless time	54
5.5	Proposal for a new probe	55
5.6	Numerical illustration	57
5.7	Discussion and outlook	59
6	Many-body localization in the Fock space of natural orbitals	61
6.1	Introduction	61
6.2	One-particle density matrices	61
6.3	Fock space of natural orbitals	64
6.4	Localization in Fock space	65
6.5	Model and parameters	68
6.6	Numerical implementation	69
6.7	Probing crossovers	70
6.8	Discussion and outlook	76
7	Gumbel statistics for many-body localized eigenstates	79
7.1	Introduction	79
7.2	Literature review	80
7.3	Gumbel statistics	81
7.4	Entanglement spectra	83
7.5	Physical setup	86
7.6	Results	88
7.7	Discussion and outlook	90
A	Matrix model for the Gaussian beta ensemble	92
A.1	Introduction	92
A.2	Tridiagonal matrices	92
A.3	Gaussian beta ensemble	93
A.4	Derivation for the Gaussian orthogonal ensemble	94

B Computational aspects	96
B.1 Introduction	96
B.2 Iterative diagonalization	96
B.3 QR diagonalization	99
B.4 Determinants	100
Bibliography	102
Popular scientific summary	111
Polulair-wetenschappelijke samenvatting	112
Acknowledgements	113

Preface

1.1 Setting the stage

Quantum systems consisting of many interacting particles typically thermalize, loosely meaning that information confined to a (small) part of the system will eventually spread out uniformly over all available space. The question under which conditions thermalization happens and how it can be avoided has been a challenge for a long time. This question attracted considerable interest in recent years, mainly triggered by the discovery of many-body localization by Basko, Aleiner, and Altshuler in 2006 [6].

Many-body localization occurs in disordered one-dimensional interacting quantum many-body systems, where emergent conserved quantities (local integrals of motion) make the system behaving as if it is integrable [7]. Currently, many-body localization is the only known robust mechanism by which interacting many-body systems can avoid thermalization [8]. Despite significant progress towards a complete understanding of the phenomenon, many questions remain open.

This dissertation discusses a number of explorations on many-body localization. In a broad sense, the focus is on the statistical properties of both the energy levels and the eigenstates of models possessing many-body localization. As for the majority of works on many-body localization, the approach is mainly numerical.

1.2 Outline and main results

One can divide this dissertation in three parts. The first part, covering chapters 2 and 3, discusses the background knowledge required for the investigations discussed thereafter. The second part consists of chapters 4 and 5, focusing on the statistics of energy levels. The final part is covered by chapters 6 and 7, which focuses on the statistics of eigenstates. The main results obtained in the works discussed in this dissertation are summarized below.

Chapter 4 Level statistics provide a common diagnostic for ergodicity in quantum many-body systems. This chapter studies the level spacing statistics across the many-

body localization transition, and compares them with the level statistics of the Gaussian beta random matrix ensemble. This ensemble provides a smooth interpolation between Poissonian and Wigner-Dyson level statistics with only a single parameter. Near-perfect agreement over the full crossover range from the thermal to the many-body localized phase is observed.

Chapter 5 Spectral form factors can be used to quantify long-range spectral correlations that are not visible when studying level spacing statistics. In this chapter, it is indicated that the time-integrated value of the spectral form factor depends on the spectral self-correlation, which could strongly affect the interpretation. A new use of the spectral form factor as a probe for ergodicity is proposed.

Chapter 6 The eigenstates of fermionic many-body systems are naturally characterized by the one-particle occupation matrix. This chapter numerically studies many-body localization in the Fock space constructed out of the natural orbitals. Focusing on the participation ratio, a crossover at a disorder strength significantly below the many-body localization transition is identified.

Chapter 7 Entanglement is fully characterized by the entanglement spectrum. Motivated by physical considerations, this chapter studies the extreme value statistics of entanglement spectra of many-body localized eigenstates. The main result is the observation of Gumbel statistics, which provides a parameter-free characterization of the many-body localized phase.

1.3 Conventions and notations

This dissertation adapts units in which the Boltzmann constant $k_B \approx 1.38 \times 10^{-23}$ J/K and the reduced Planck constant $\hbar \approx 1.05 \times 10^{-34}$ J s are both set to unity. For summations and integrations, the range is sometimes omitted for notational convenience when it is clear from the context.

Many-body localization

2.1 Introduction

Many-body localization is a relatively recently discovered phase of matter which distinguishes itself by the fact that it can not be described by conventional statistical physics. Many-body localization can be seen as a generalization of the real-space Anderson localization to the many-body Fock space. This chapter aims to introduce the subject by discussing a number of selected topics.

Anderson localization is briefly reviewed in section 2, followed by a discussion of the generalization to many-body localization in section 3. Often, many-body localization is interpreted by using a phenomenological model, which is discussed in section 4. Section 5 reviews a number of key signatures of many-body localization. Finally, section 6 introduces a ‘standard model’ in the field of many-body localization, which is studied in parts of the remainder of this dissertation.

Arguably the most profound topics in the literature on many-body localization that are not covered in this chapter are the many-body localization transition separating the many-body localized phase from the thermal phase, the non-trivial phenomena such as anomalous diffusion and Griffiths effects at the thermal side of the many-body localization transition, and experimental realizations in for example cold atom-experiments. For a recent review of these topics, the reader is referred to ref. [8].

2.2 Anderson localization

Anderson localization is a phenomenon of disorder-induced localization for non-interacting quantum systems, discovered over sixty years ago [9]. As in the original work cited above, consider the tight-binding lattice Hamiltonian

$$H = -t \sum_{i=1}^{L-1} \left[c_i^\dagger c_{i+1} + c_{i+1}^\dagger c_i \right] + \sum_{i=1}^L V_i c_i^\dagger c_i. \quad (2.1)$$

The operator c_i^\dagger (c_i) creates (annihilates) a particle on site i , and obeys the fermionic anticommutation relations

$$\{c_i^\dagger, c_j\} = \delta_{ij}, \quad (2.2)$$

$$\{c_i^\dagger, c_j^\dagger\} = \{c_i, c_j\} = 0. \quad (2.3)$$

The first term of the Hamiltonian (proportional to t) describes the hopping of spinless fermions between neighboring sites, the second term describes an onsite site-dependent potential V_i . The total number of particles is conserved. In the context of Anderson localization, the potential terms V_i are given by independent random variables, representing disorder. The focus is on potential terms that are sampled from the probability distribution

$$P(x) = \begin{cases} 1/(2W) & \text{if } |x| \leq W, \\ 0 & \text{if } |x| > W, \end{cases} \quad (2.4)$$

corresponding to a uniform distribution ranging over the interval $[-W, W]$. It should be remarked that, even though it is conventional to sample V_i from probability distribution given in eq. (2.4), the physics does not depend strongly on the characteristics of the probability distribution.

Ref. [9] shows that the presence of disorder induces interference effects leading to the spatial localization of *all* single-particle eigenstates for *any* value $W/t > 0$ when considering the thermodynamic limit $L \rightarrow \infty$. Spatial localization of a single-particle eigenstate (or more general, a single-particle state) can be quantified by the overlaps with the spatially localized basis states

$$|i\rangle = c_i^\dagger |0\rangle, \quad (2.5)$$

where $|0\rangle$ is the zero-particle (vacuum) state. Here, the spatial localization of a state $|\phi\rangle$ means that there exist i and σ such that the envelope of $|\phi\rangle$ obeys the asymptotic scaling

$$|\langle\phi|x\rangle|^2 \sim \exp\left[-\left(\frac{i-x}{\sigma}\right)^2\right]. \quad (2.6)$$

Note that this scaling differs qualitatively from the scaling $|\langle\phi|x\rangle|^2 \sim 1/L$ for extended (delocalized) states. Scaling arguments [10] show that a similar phenomenology holds for two-dimensional systems, while in three dimensions there is a mobility edge above (below) which eigenstates are delocalized (localized). At the transition point, non-trivial phenomena such as multifractality of eigenstates have been observed [11].

This section only pointed out some basic aspects of Anderson localization. A more throughout pedagogical introduction is provided in for example ref. [12]. A review of relatively recent developments is provided in ref. [13].

2.3 From Anderson to many-body localization

Considerable interest has been devoted to the robustness of Anderson localization against interactions [6, 14, 15]. Consider an L -site lattice model of non-interacting spinless fermions, and let d_i^\dagger (d_i) denote the operators creating (annihilating) the single-particle eigenstate $|\phi_i\rangle$ from the zero-particle state $|0\rangle$, meaning that

$$d_i^\dagger|0\rangle = |\phi_i\rangle, \quad d_i|\phi_i\rangle = |0\rangle. \quad (2.7)$$

In terms of these operators and the eigenvalues ϵ_i associated with the single-particle eigenstates $|\phi_i\rangle$, the Hamiltonian H takes the diagonal form

$$H = \sum_{i=1}^L \epsilon_i d_i^\dagger d_i. \quad (2.8)$$

An eigenstate $|\psi_{\vec{n}}\rangle$ labeled by the indices $\vec{n} = \{i_1, i_2, \dots, i_N\}$ of the N occupied single-particle eigenstates is given by the *Slater determinant* (see for example ref. [16]) reading

$$|\psi_{\vec{n}}\rangle = \frac{1}{\sqrt{N}} \sum_{i_1, i_2, \dots, i_N} \left(\det \{ \phi_{n_j}(i_k) \}_{j,k=1,2,\dots,N} \right) |i_1\rangle \otimes |i_2\rangle \otimes \dots \otimes |i_N\rangle, \quad (2.9)$$

where $\phi_i(j) = \langle \phi_i | j \rangle$ and all summed indices run over $1, 2, \dots, L$. The eigenstate satisfies the fermionic antisymmetry property due to the determinantal structure of the expansion. The collection of all multi-particle eigenstates spans a basis for the *Fock space* constructed out of the single-particle eigenstates.

The concept of spatial localization for single-particle states can not be extended to systems of interacting particles in a trivial way. An arguably natural generalization is provided by *many-body localization* [6]. For spinless fermions, interacting systems are described in general by Hamiltonians of the form $H = H_0 + H_{\text{int}}$, where

$$H_0 = \sum_i \epsilon_i c_i^\dagger c_i, \quad (2.10)$$

$$H_{\text{int}} = \sum_{ij} J_{ij}^{(1)} c_i^\dagger c_j + \sum_{ijkl} J_{ijkl}^{(2)} c_i^\dagger c_j^\dagger c_k c_l. \quad (2.11)$$

The first and second term represent respectively the diagonal and the off-diagonal part of the Hamiltonian, meaning that $J^{(n)} = 0$ if the first and last n indices are identical. An eigenstate of H is said to be *many-body localized* if it is localized in the Fock space, meaning that it can be obtained by a perturbative treatment of the non-diagonal part H_{int} . Many-body localization can be viewed as a generalization of the real-space Anderson localization to Fock space.

Many-body localization was first established by Basko, Aleiner, and Altshuler in 2006 for a model with weak two-body interaction terms [6]. It was found that this model has a mobility edge below (above) which all eigenstates are localized (delocalized).

2.4 Phenomenology of many-body localization

The generalization of Anderson localization to many-body localization has been established for a model with weak two-body interactions in ref. [6]. Using numerical techniques, it was suggested first by Oganesyan and Huse in 2007 [17] that many-body localization persists even in the non-perturbative regime. Since then, a lot of evidence in favor of this statement has been reported [18].

A well-adapted qualitative phenomenological model for many-body localization in a beyond-perturbative setting has been proposed by Huse, Nandkishore, and Oganesyan in 2014 [7]. Consider a system of N spin-1/2 particles (which can be mapped to a system of spinless fermions by a Jordan-Wigner transformation). The starting point is the notion that, in general, there exist a set of (not necessarily local) pseudospin operators inducing a basis in which all eigenstates of the Hamiltonian are product states. Let the pseudospin operators be given by

$$\tau_i^x = \frac{1}{2} \begin{pmatrix} 0 & 1 \\ 1 & 0 \end{pmatrix}, \quad \tau_i^y = \frac{1}{2} \begin{pmatrix} 0 & -i \\ i & 0 \end{pmatrix}, \quad \tau_i^z = \frac{1}{2} \begin{pmatrix} 1 & 0 \\ 0 & -1 \end{pmatrix}, \quad (2.12)$$

with $\tau_i^{x,y,z}$ acting only on the pseudoparticle with index $i \in \{1, 2, \dots, N\}$, leaving the others unaffected. The Hamiltonian H is diagonal in the basis induced by the pseudospin operators, implying that the number of independent elements equals $\dim(H) = 2^N$. In terms of the pseudospin operators, the Hamiltonian takes the diagonal form

$$H = J^{(0)} + \sum_i J_i^{(1)} \tau_i^z + \sum_{i>j} J_{ij}^{(2)} \tau_i^z \tau_j^z + \dots + \sum_{i>j>k>\dots} J_{ijk\dots}^{(N)} \tau_i^z \tau_j^z \tau_k^z \dots \quad (2.13)$$

The Hamiltonian is diagonal in the basis induced by the τ_i^z ($i = 1, 2, \dots, N$), which follows from the observation that $[H, \tau_i^z] = 0$ for all i . It can be verified easily that the number of expansion coefficients in eq. (2.13) equals the dimension of the Hilbert space by using the combinatorial relation

$$\sum_{i=0}^N \binom{N}{i} = 2^N. \quad (2.14)$$

Remark that finding the expansion coefficients in eq. (2.13) is a non-trivial task. As far as the author is aware, no direct formula in terms of the eigenvalues of H is known.

The phenomenological model discussed in this section applies to Hamiltonians H for which *all* eigenstates are many-body localized. It proposes that the expansion of the Hamiltonian in the form of eq. (2.13) has the non-generic property that the pseudospins are spatially localized. More precisely, supposing that the τ_i^z are spatially ordered (meaning that τ_{i+1}^z is located at the right side of τ_i^z), one finds

$$J_{ij}^{(2)} \sim e^{-|j-i|/\xi}, \quad J_{ijk}^{(3)} \sim e^{-|k-i|/\xi}, \quad J_{ijkl}^{(4)} \sim e^{-|l-i|/\xi} \quad (2.15)$$

et cetera, where ξ is the localization length depending on the details of the system. The prefactor in front of the exponential is comparable for all orders.

For the purpose of an analytical study on many-body localization, the phenomenological model was formulated more precisely by Imbrie in 2016 [19, 20]. Adapting the definition used in ref. [20], many-body localization is equivalent to *all* of the following properties of the eigenvalues and eigenstates of the Hamiltonian:

1. The Hamiltonian can be diagonalized by a sequence of unitary basis transformations, each acting only on a spatially localized region. Each basis transformation is generated by quasi-local operators, meaning that a transformation generator involving n spins is exponentially small in n with high probability. These transformations define a way to deform the original basis states into the exact eigenstates.
2. Resonant regions where the required transformations are far from the identity are dilute; the probability that two sites a distance ℓ apart are in the same resonant region decays faster than any power law of ℓ . It is the violation of this property that suggests many-body localization to be unstable in dimensions $d \geq 2$ [21].
3. Away from resonant regions, each eigenstate resembles the basis state it came from in terms of the physical spins. This physical basis state can be used to label the eigenstate. The pseudo-spins can be thought of as ‘dressed’ physical spins, and many-body localization can be thought of as a phenomenon of emergent integrability.

Several attempts to identify the pseudospins (sometimes referred to as ‘local integrals of motion’ or ‘local conserved charges’) have been undertaken. An example is provided in ref. [22].

2.5 Signatures of many-body localization

Many-body localized systems can be distinguished from delocalized (ergodic) ones in various ways. This section aims to provide a (non-exhaustive) list of diagnostics for many-body localization that are encountered in the literature. The selection is partially guided by the similar list in a relatively recent review by Alet and Laflorencie [23].

2.5.1 Poissonian level statistics

Many-body localized and delocalized many-body systems are characterized by different statistics for the spacings between consecutive energy levels, known as respectively *Poissonian* and *Wigner-Dyson* [24]. Let

$$\{E_i\}_{i=1}^N, \quad E_1 \leq E_2 \leq \dots \leq E_N \quad (2.16)$$

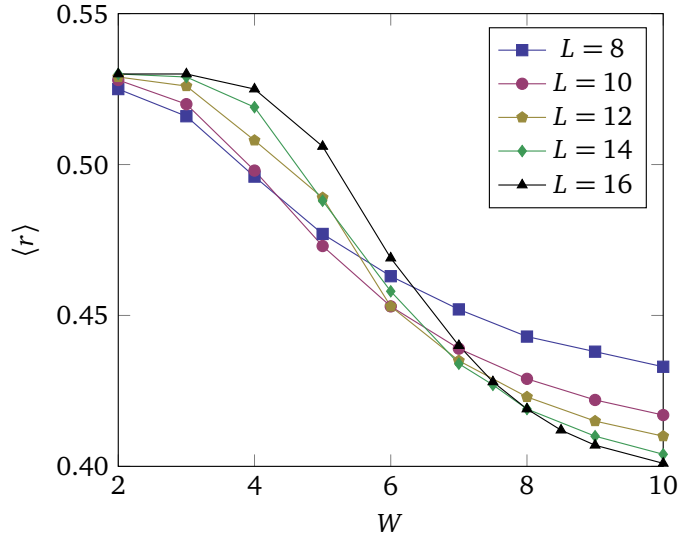


Fig. 2.1: The average ratio of consecutive level spacings for a one-dimensional model of strongly interacting spinless fermions with disorder. The parameters W and L give the disorder strength and chain length, respectively. The data presented in this figure is extracted from ref. [17], in which also details on the model can be found.

denote an energy spectrum, with the elements sorted in ascending order. An in the field of many-body localization often used diagnostic to discriminate between Poissonian and Wigner-Dyson level spacing statistics is provided by the average ratio $\langle r \rangle$ of consecutive level spacings [25],

$$\langle r \rangle = \frac{1}{N-2} \sum_{i=1}^{N-2} r_i, \quad r_i = \min \left(\frac{E_{i+2} - E_{i+1}}{E_{i+1} - E_i}, \frac{E_{i+1} - E_i}{E_{i+2} - E_{i+1}} \right). \quad (2.17)$$

For localized and delocalized systems, it follows from random matrix theory arguments (discussed in chapters 3 and 4) that the average ratio of consecutive level spacings acquires a value $\langle r \rangle \approx 0.386$ and $\langle r \rangle \approx 0.530$, respectively. It is convenient to perform additional averaging over disorder realizations.

The use of level statistics to diagnose localization can be illustrated with the results reported by Oganesyan and Huse cited above [17]. The focus is on a one-dimensional disordered lattice with strongly interacting spinless fermions. Fig. 2.1 shows $\langle r \rangle$ as a function of the disorder strength W and chain length L . The average $\langle r \rangle$ is computed from full spectra (meaning that considering infinite temperature) and additionally averaged over a large number of disorder realizations.

With increasing system size, one observes a drift of $\langle r \rangle$ towards the value for localized systems at strong enough disorder, which is interpreted as a hint for the existence of a many-body localized phase in the thermodynamic limit $L \rightarrow \infty$. Additional evidence based on level statistics has been provided for example in refs. [26, 27].

2.5.2 Area-law scaling of eigenstate entanglement entropy

Entanglement is a concept used to quantify the connectedness of different parts of a system. It plays an important role in the field of condensed matter physics, including many-body localization [28]. Consider the generic setting of a system decomposed in subsystems A and B . Let

$$\{|a_i\rangle\}_{i=1}^M, \quad \{|b_i\rangle\}_{i=1}^N \quad (2.18)$$

denote basis states for the respective subsystems, without loss of generality labeled such that $M \geq N$. A pure state $|\psi\rangle$ is associated with a density matrix $\rho = |\psi\rangle\langle\psi|$. Taking the partial trace of the density matrix over the basis states of subsystem A , one obtains the reduced density matrix

$$\rho_B = \text{Tr}_A(|\psi\rangle\langle\psi|) \quad (2.19)$$

of subsystem B . This matrix encodes all information accessible by performing measurements on subsystem B only. A common (but not unique [29]) measure for the degree of entanglement between subsystems A and B is provided by the entanglement entropy

$$S_{\text{ent}} = -\text{Tr} \left[\rho_B \ln(\rho_B) \right] \quad (2.20)$$

$$= -\sum_{i=1}^N \lambda_i \ln(\lambda_i) \quad (2.21)$$

with λ_i ($i = 1, 2, \dots, N$) denoting the eigenvalues of ρ_B . The entanglement entropy takes a value bounded from below by $S_{\text{ent}} = 0$ for unentangled states corresponding to $\{\lambda_i\} = \{1, 0, 0, \dots, 0\}$, and bounded from above by $S_{\text{ent}} = \ln(n)$ for maximally entangled states corresponding to $\{\lambda_i\} = \{1/N, 1/N, \dots, 1/N\}$.

Many-body localization is believed to be a phase of matter that can be observed in one-dimensional systems only [21]. Consider a one-dimensional chain of L (spin-1/2) particles divided into parts A and B covering respectively the first L_A and last $L_B = L - L_A$ sites, with $L_B \leq L_A$ to ensure $M \geq N$. It was established in refs. [30, 31] that the entanglement entropy for many-body localized eigenstates obeys the area-law scaling

$$S_{\text{ent}} \sim \text{constant}. \quad (2.22)$$

Note that a similar scaling can be observed for single-particle eigenstates of Anderson localized systems. Remark that this scaling contrasts with the volume-law scaling $S_{\text{ent}} \sim L_B$ observed for ergodic states [32].

2.5.3 Logarithmic growth of entanglement entropy

A hallmark of many-body localization is logarithmic growth of the entanglement entropy in time. This phenomenon has been observed first by Žnidarič, Prosen and Prelovšek in 2008 [33], but only attracted significant attention after a more systematic

investigation by Bardarson, Pollmann and Moore in 2012 [34] and a phenomenological explanation by Serbyn, Papić and Abanin in 2013 [35].

The setup in which this phenomenon is observed consists of a one-dimensional system in a many-body localized phase, splitted in two subsystems covering the left- and right-hand sides, and prepared in the (unentangled) Neél state. Let $|\psi(t)\rangle$ denote the state of the system at time t , obtained from the initial state $|\psi(0)\rangle$ by applying the time-evolution operator,

$$|\psi(t)\rangle = e^{iHt}|\psi(0)\rangle \quad (2.23)$$

with H denoting the Hamiltonian of the system. The focus is on the ensemble-average of the entanglement entropy $\langle S_{\text{ent}}(t) \rangle$ as a function of time. Here, the ensemble average is taken over disorder realizations. It has been observed [33, 34] that after a short transient period, the ensemble-average of the entanglement entropy displays a slow growth

$$\langle S_{\text{ent}}(t) \rangle \sim \ln(t), \quad (2.24)$$

being in sharp contrast with $\langle S_{\text{ent}}(t) \rangle \sim t$ for thermal systems. This growth is believed to persist up to $t \rightarrow \infty$ in the thermodynamic limit of large system sizes. This observation is understood as being a consequence of dephasing between remote local integrals of motion, which is a distinguishing property of many-body localization [35].

2.6 Standard model of many-body localization

This section introduces a ‘standard model’ of many-body localization, which is studied in parts of the remainder of this dissertation. The model can be seen as an extension of the Anderson-localized model discussed in section 2.2 with interactions. The expression for the Hamiltonian H reads

$$H = \sum_{i=1}^L \left[S_i^x S_{i+1}^x + S_i^y S_{i+1}^y + S_i^z S_{i+1}^z + h_i S_i^z \right], \quad (2.25)$$

where periodic boundary conditions $S_{L+1}^{x,y,z} \equiv S_1^{x,y,z}$ are imposed. The Hamiltonian describes an L -site spin-1/2 XXX-chain appended by a site-dependent onsite potential h_i . The spin-1/2 operators in which it is formulated are given by

$$S_i^x = \frac{1}{2} \begin{pmatrix} 0 & 1 \\ 1 & 0 \end{pmatrix}, \quad S_i^y = \frac{1}{2} \begin{pmatrix} 0 & -i \\ i & 0 \end{pmatrix}, \quad S_i^z = \frac{1}{2} \begin{pmatrix} 1 & 0 \\ 0 & -1 \end{pmatrix}, \quad (2.26)$$

with $S_i^{x,y,z}$ acting only on site $i \in \{1, 2, \dots, L\}$, leaving the others unaffected. As for the Anderson-localized model discussed in section 2 of this chapter, the onsite potentials h_i represent disorder. As before, the potentials are sampled independently from the probability distribution

$$P(x) = \begin{cases} 1/(2W) & \text{if } |x| \leq W, \\ 0 & \text{if } |x| > W, \end{cases} \quad (2.27)$$

corresponding to the uniform distribution ranging over the interval $[-W, W]$. Observe that, apart from the interaction term $S_i^z S_{i+1}^z$, the Hamiltonian is equivalent to the one given in eq. (2.1) for $t = 1$ by a Jordan-Wigner transformation as given in eq. (6.24) below.

For the Hamiltonian given in eq. (2.25), the total spin projection

$$S^z = \sum_{i=1}^L S_i^z \quad (2.28)$$

is a conserved quantity, meaning that $[H, S^z] = 0$. It is convenient to consider L even and restrict the focus to the $S^z = 0$ sector. The dimension of this symmetry sector of the Hamiltonian is given by $\binom{L}{L/2}$, scaling exponentially in L for large system sizes. For $L = 10, 12, 14$ and 16 one finds the respective Hilbert space dimensions 252, 924, 3432 and 12970. Standard modern computer facilities allow for the exact diagonalization of Hamiltonians up to size $L = 16$.

The physics of the model discussed in this section is dependent on the energy density (not to be confused with the density of states). Let $\{E_i\}_{i=1}^{\dim(H)}$ denote the set of eigenvalues of the Hamiltonian for a given disorder realization, and let $E_{\min} = \min_i(E_i)$ and $E_{\max} = \max_i(E_i)$ denote the lowest and the highest energy level, respectively. The energy density $\epsilon_i \in [0, 1]$ corresponding to an energy level E_i is given by

$$\epsilon_i = \frac{E_i - E_{\min}}{E_{\max} - E_{\min}}. \quad (2.29)$$

A careful numerical study by Luitz, Laflorencie, and Alet from 2015 [27] strongly suggests that in the thermodynamic limit $L \rightarrow \infty$, the model is in a many-body localized phase at $\epsilon = 0.5$ for disorder strengths $W \gtrsim 3.6$, while it is in a thermal phase at weaker disorder. Remark that, contrary to most other branches of condensed matter physics, the focus is typically on highly-excited states at nonzero energy density.

Random matrix theory

3.1 Introduction

The first connection between physics and random matrix theory was established mainly by Wigner and Dyson in a number of studies on spacings between energy levels for heavy atomic nuclei (see for example refs. [36, 37]). The motivation to study the spectral properties of such systems using random matrix theory is two-fold [38]:

1. Heavy nuclei consist of ~ 100 strongly interacting particles. The resulting complicated structures of the associated Hamiltonians does not allow for analytical studies both technically (diagonalizing) and physically (interpreting).
2. The statistics of the spacings between consecutive energy levels appear to be independent of the specific constitution of the nucleus that is studied, suggesting the use of a statistical approach.

Similar considerations led to the discovery of many more connections between (condensed matter) physics and random matrix theory [39, 40]. This chapter reviews some connections between random matrix theory and the statistical properties of ergodic (in the context of many-body localization, delocalized) systems, serving as an introduction to the following chapters on localization.

Sections 2 and 3 random matrix models for Hamiltonians of ergodic systems. Section 4 discusses the circular ensembles, serving as random matrix models for Floquet operators as discussed in chapter 5. Section 5 discusses a number of probes for eigenvalue statistics of random matrices. Section 6 discuss the universal statistics of entanglement ergodic systems obey. The content of this chapter is also covered in most standard reference works on random matrix theory, such as ‘Random Matrices’ by Mehta [24] or ‘Log-Gases and Random Matrices’ by Forrester [41].

3.2 Gaussian invariant ensembles

This section discusses part of the content covered in sections 1.1 and 1.3 of the book ‘Log-Gases and Random Matrices’ by Forrester [41]. For a system obeying time-reversal

symmetry, the Hamiltonian can be expressed as a real symmetric matrix. Random matrix models for such matrices are given by samples from the Gaussian orthogonal ensemble. This ensemble consist of real symmetric matrices for which the diagonal and upper triangular elements are sampled independently from probability distributions

$$P(x) = \frac{1}{\sqrt{2\pi}} e^{-x^2/2}, \quad P(x) = \frac{1}{\sqrt{\pi}} e^{-x^2}, \quad (3.1)$$

respectively. The diagonal elements are sampled from a Gaussian distribution with mean 0 and variance 1, while the upper triangular elements are sampled from a Gaussian distribution with mean 0 and variance 1/2. The joint probability distribution for the elements X_{ij} ($i, j = 1, 2, \dots, N$) of a matrix X of dimension N is given by

$$P(X) = \prod_{i=1}^N \frac{1}{\sqrt{2\pi}} e^{-X_{ii}^2/2} \prod_{j<i} \frac{1}{\sqrt{\pi}} e^{-X_{ij}^2} \quad (3.2)$$

$$= \frac{1}{C_N} \prod_{i,j=1}^N \exp\left[-\frac{1}{2} X_{ij}^2\right] \quad (3.3)$$

$$= \frac{1}{C_N} \exp\left[-\frac{1}{2} \sum_{i,j=1}^N X_{ij}^2\right] \quad (3.4)$$

$$= \frac{1}{C_N} \exp\left[-\frac{1}{2} \text{Tr}(X^2)\right] \quad (3.5)$$

with C_N denoting a normalization constant. The motivation to construct the ensemble in this particular way follows from inspection of eq. (3.5). A basis transformation $X \rightarrow \tilde{X} = OXO^{-1}$ for an orthogonal $N \times N$ matrix O leaves $P(X)$ invariant, as

$$\text{Tr}(X^2) \rightarrow \text{Tr}(\tilde{X}^2) \quad (3.6)$$

$$= \text{Tr}(OXO^{-1}OXO^{-1}) = \text{Tr}(O(XX)O^{-1}) = \text{Tr}(X^2). \quad (3.7)$$

The invariance of $P(X)$ under transformations of the basis means that the ensemble has no preferred basis, which can be interpreted as ‘maximal randomness’ of the ensemble. The eigenstates are said to be *ergodic*.

Next to the Gaussian orthogonal ensemble there exist the Gaussian unitary and symplectic ensembles, which are invariant under unitary and symplectic basis transformations, respectively. The former serves as a random matrix model for Hamiltonians with broken time-reversal symmetry. It consist of Hermitian matrices (meaning that elements are related by the relation $X_{ij} = \bar{X}_{ji}$). The diagonal elements (which are real-valued) are sampled independently from the probability distribution

$$P(x) = \frac{1}{\sqrt{\pi}} e^{-x^2}, \quad (3.8)$$

corresponding to a Gaussian distribution with mean 0 and variance 1/2, while the upper triangular elements $x = u + iv$ with $u, v \in \mathbb{R}$ real-valued are sampled independently

from the probability distribution

$$P(x) = \frac{2}{\pi} e^{-2(u^2+v^2)} = \frac{2}{\pi} e^{-2|x|^2}, \quad (3.9)$$

representing a complex Gaussian with 0 and variance 2. As for the Gaussian orthogonal ensemble, the joint probability distribution for the elements X_{ij} ($i, j = 1, 2, \dots, N$) of a matrix X is given by

$$P(X) = \prod_{i=1}^N \frac{1}{\sqrt{\pi}} e^{-X_{ii}^2/2} \prod_{j<i} \frac{2}{\pi} e^{-2|X_{ij}|^2} \quad (3.10)$$

$$= \frac{1}{C_N} \exp\left[-\frac{1}{2} \text{Tr}(X^2)\right], \quad (3.11)$$

again for a normalization constant C_N . The invariance $P(UXU^{-1}) = P(X)$ for any unitary matrix U follows as before.

The Gaussian symplectic ensemble is not discussed separately as it has no direct application in the context of this dissertation. It will be incorporated in the general description of the Gaussian invariant ensembles discussed in section 4.3 of the next chapter.

3.3 Eigenvalue statistics

The universality of level spacing statistics mentioned in the introduction of this chapter extends to a broad range of physical systems. These statistics are known as *Wigner-Dyson*, and have been conjectured to apply generally to systems that are non-integrable in the semiclassical limit ($\hbar \rightarrow 0$) by Bohigas, Giannoni, and Schmit 1984 [42]. This section discusses these statistics.

3.3.1 Joint probability distribution

The content of the below discussion is covered in sections 1.2 and 1.3 of the book ‘Log-Gases and Random Matrices’ by Forrester [41]. An arguably natural representation of a random matrix ensemble is given by the joint probability distribution for the matrix elements X_{ij} , as for example in eq. (3.5). Alternatively, one might consider the representation in terms of the joint probability distribution for the eigenvalues λ_i and the remaining variables p_i , which are linear combinations of the independent elements of the eigenvectors. Let $\{q_i\}$ denote the union of $\{\lambda_i\}$ and $\{p_i\}$. For the Gaussian invariant ensembles of dimension N , the joint probability distribution for the elements q_i reads

$$P(\{q_i\}) = \exp\left[-\frac{1}{2} \sum_{i=1}^N \lambda_i^2\right] |J|, \quad (3.12)$$

where the first term on the right hand-side is equal to $\exp[-\text{Tr}(X^2)/2]$ in the basis in which X is diagonal, and J is the Jacobian relating the coordinates $\{X_{ij}\}$ to $\{q_i\}$ given by

$$J = \begin{pmatrix} \frac{\partial X_{11}}{\partial q_1} & \frac{\partial X_{12}}{\partial q_1} & \cdots & \frac{\partial X_{NN}}{\partial q_1} \\ \frac{\partial X_{11}}{\partial q_2} & \frac{\partial X_{12}}{\partial q_2} & \cdots & \frac{\partial X_{NN}}{\partial q_2} \\ \vdots & \vdots & \ddots & \vdots \\ \frac{\partial X_{11}}{\partial q_{N(N+1)/2}} & \frac{\partial X_{12}}{\partial q_{N(N+1)/2}} & \cdots & \frac{\partial X_{NN}}{\partial q_{N(N+1)/2}} \end{pmatrix}. \quad (3.13)$$

Remark that a symmetric matrix of dimension N has $N(N+1)/2$ degrees of freedom, of which are N required to fix the eigenvalues and $N(N-1)/2$ to fix the eigenvectors.

The Gaussian random matrix ensembles discussed in the previous section were indicated to be invariant under basis transformations. This suggests that the joint probability distribution for the λ_i and the p_i factorizes in parts depending on either the λ_i or the p_i . Indeed, the evaluation of the Jacobian for the Gaussian orthogonal ensemble yields the factorized expression

$$J = \prod_{i < j} |\lambda_i - \lambda_j| f(p_1, p_2, \dots, p_{N(N-1)/2}), \quad (3.14)$$

where f is some function only depending on the elements of $\{p_i\}$. The joint distribution for the eigenvalues is obtained by integrating out the p_i from $P(\{\lambda_i\}, \{p_i\})$. The value of the integral over the p_i can be absorbed in a normalization constant, resulting in the joint distribution for the eigenvalues of the Gaussian orthogonal ensemble is given by

$$P(\lambda_1, \lambda_2, \dots, \lambda_N) = \frac{1}{C_N} \exp\left[-\frac{1}{2} \sum_{i=1}^N \lambda_i^2\right] \prod_{i < j} |\lambda_i - \lambda_j| \quad (3.15)$$

with C_N denoting a normalization constant. A derivation can be found in appendix A. The exponent strongly suppresses the probability to find configurations in which some eigenvalues are very far from the origin, while the product factor strongly suppresses the probability to find configurations in which two eigenvalues are very close to each other. As a consequence, the eigenvalues are strongly correlated.

The above discussion of the Gaussian orthogonal ensemble can be generalized to the unitary and symplectic ensembles. For this, one introduces the *Dyson index*

$$\beta = \begin{cases} 1 & \text{(Gaussian orthogonal ensemble),} \\ 2 & \text{(Gaussian unitary ensemble),} \\ 4 & \text{(Gaussian symplectic ensemble).} \end{cases} \quad (3.16)$$

The Dyson index, first introduced by Dyson in 1962 [37], gives the number of degrees of freedom per matrix element (1 for real numbers, 2 for complex numbers, 4 for quaternionic numbers). It can be shown that the joint probability distribution for

the eigenvalues of the Gaussian orthogonal ensemble as given in eq. (3.15) can be generalized to

$$P(\lambda_1, \lambda_2, \dots, \lambda_N) = \frac{1}{C_{N,\beta}} \exp\left[-\frac{1}{2} \sum_{i=1}^N \lambda_i^2\right] \prod_{i<j} |\lambda_i - \lambda_j|^\beta, \quad (3.17)$$

where β is the Dyson index and $C_{N,\beta}$ is a normalization constant.

3.3.2 Coulomb gas analogy

This section discusses part of the content covered in section 1.4 of the book ‘Log-Gases and Random Matrices’ by Forrester [41]. Eq. (3.17) can be interpreted as the Boltzmann factor of a so-called 1-dimensional *Coulomb gas* at inverse temperature $\beta = 1/T$,

$$P(\lambda_1, \lambda_2, \dots, \lambda_N) = \frac{1}{\mathcal{Z}} e^{-\beta \mathcal{V}[\lambda_i]}. \quad (3.18)$$

Here, λ_i are the positions of fictitious particles, $\mathcal{V}[\lambda_i]$ is the configuration energy, and $\mathcal{Z} = C_{N,\beta}$ is the partition function which is equal to the normalization constant. Generically, one can identify a joint eigenvalue distribution with a Boltzmann factor if it can be written in the form of eq. (3.18) for some β -independent potential $\mathcal{V}[\lambda_i]$. For eq. (3.17), one has

$$\mathcal{Z} = \int_0^\infty \left(\prod_{i=1}^n d\lambda_i \right) e^{-\beta \mathcal{V}[\lambda_i]}, \quad (3.19)$$

$$\mathcal{V}[\lambda_i] = \frac{1}{2} \sum_{i=1}^n \lambda_i^2 - \sum_{i<j} \ln |\lambda_i - \lambda_j|. \quad (3.20)$$

The gas is in equilibrium under the competing effect of a quadratic one-particle potential and pairwise repulsion. The quadratic potential is attractive towards the origin.

A Coulomb gas (sometimes called a *logarithmic gas*) is characterized by an interaction potential between particles i and j scaling as $\ln |\lambda_i - \lambda_j|$. Coulomb gas particles can be thought of as infinitely long parallel oriented rods with an uniform charge density, for which the Coulomb force is described by a logarithmic potential [43].

3.3.3 Wigner’s semicircle law

The physical interpretation of the eigenvalue distribution for the Gaussian invariant ensembles given in eq. (3.17) as the Boltzmann factor of a Coulomb gas allows one to use techniques from statistical physics. By making a continuum approximation, the Boltzmann factor function can be rewritten in terms of the charge density

$$\rho(\lambda) = \left\langle \sum_{i=1}^N \delta(\lambda - \lambda_i) \right\rangle, \quad (3.21)$$

where $\langle \cdot \rangle$ denotes an ensemble average. Determining the associated partition function \mathcal{Z} and minimizing the free energy $F = -\beta^{-1} \ln(\mathcal{Z})$ gives the equilibrium charge density.

A lengthy but straightforward calculation (see for example section 4.2 of the book ‘Introduction to Random Matrices’ by Livan, Novaes, and Vivo [44]) shows that for the Gaussian invariant ensembles, one finds

$$\lim_{N \rightarrow \infty} \sqrt{\beta N} \rho(\sqrt{\beta N} \lambda) = \frac{1}{\pi} \sqrt{2 - x^2} \quad (3.22)$$

for $x \in [-\sqrt{2\beta N}, \sqrt{2\beta N}]$, which has the form of a semicircle. This result is known as *Wigner’s semicircle law*, first found for the Gaussian unitary ensemble of infinite dimension by Wigner in 1958 [45]. Qualitative agreement of the charge density with the semicircle law can be observed already for small matrix dimensions $N \sim 100$ at all allowed values of β [46].

Physical systems are ‘maximally random’ often only *locally* (on a finite, microscopic energy window). Consequently, the semicircle law of eq. (3.22) does typically not hold for physical systems, even though Wigner-Dyson level statistics can be observed [47]. Local level statistics are known to be largely independent of the smooth part of the density of states as given in eq. (3.21) [48].

3.4 Circular ensembles

This section discusses the circular random matrix ensembles, introduced by Dyson in 1962 [37]. The circular ensembles are random matrix models for unitary matrices, having eigenvalues $\{\lambda_j\}$ lying on the unit circle centered at the origin in the complex plane, meaning that they are parametrizable as $\lambda_j = \exp(i\theta_j)$ with $\theta_i \in [0, 2\pi)$. This section is based on parts of section 2.2 of the book ‘Log-Gases and Random Matrices’ by Forrester [41].

Similar to the case of the Gaussian random matrix ensembles, one distinguishes the circular orthogonal, unitary, and symplectic ensembles. Let

$$O(N) := \{N \times N \text{ complex-valued symmetric unitary matrices}\} \quad (3.23)$$

$$U(N) := \{N \times N \text{ complex-valued unitary matrices}\} \quad (3.24)$$

$$\text{Sp}(2N) := \{N \times N \text{ real quaternionic unitary matrices}\}. \quad (3.25)$$

The circular unitary ensemble of dimension N contains elements from $U(N)$ sampled uniformly with respect to the Haar measure. Again, this means that the ensemble is invariant under basis transformations.

The spaces of real and quaternion valued unitary matrices do not form groups under multiplication. For example, the product of two complex-valued symmetric unitary matrices is not necessarily symmetric again. This implies that the circular orthogonal and symplectic ensembles can not be defined in a similar fashion as the circular unitary

ensemble. As the focus below is only on the eigenvalues (and not the eigenvectors), the construction of these ensembles is not discussed here.

As for the Gaussian invariant ensembles, the circular ensembles can be labeled by the Dyson index β as introduced in eq. (3.16). Analogously, let $\beta = 1, 2, 4$ for respectively the circular orthogonal, unitary, and symplectic ensembles. In terms of β , the joint probability distribution for the eigenvalues $\{\exp(i\theta_j)\}_{j=1}^N$ for matrices of dimension N is proportional to

$$\prod_{j < k} |e^{i\theta_j} - e^{i\theta_k}|^\beta, \quad (3.26)$$

with an explicitly known normalization constant. Trivially, the density of states for the circular ensembles is uniform.

The elements of unitary matrices are correlated, such that no (simple) description of the ensembles in terms of the matrix elements can be formulated. Numerical algorithms to sample from the circular ensembles are described in for example ref. [49].

3.5 Probing eigenvalue statistics

Level spacing statistics are used to discriminate between ergodic (semiclassically non-integrable) and non-ergodic (semiclassically integrable) systems. For the latter, it has been conjectured by Berry and Tabor in 1977 [50] that the energy levels are uncorrelated, implying that the spacings between consecutive energy levels are Poissonian distributed. Nowadays, the occurrence of Poissonian level spacing statistics is often adapted as a *definition* of quantum integrability [51].

3.5.1 Level spacing distribution

A convenient diagnostic for local level statistics is given by the level spacing distribution [24]. Let

$$\{E_i\}_{i=1}^N, \quad E_1 \leq E_2 \leq \dots \leq E_N \quad (3.27)$$

denote an energy spectrum, with the elements sorted in ascending order. Because correlations decay on microscopic windows (only a few levels apart as illustrated below), the level spacings

$$s_i = E_{i+1} - E_i, \quad (i = 1, 2, \dots, N-1) \quad (3.28)$$

can essentially be treated as independent random variables when considering statistics. Considering a spectrum with an uniform density of states scaled such that the average level spacing

$$\langle s \rangle = \frac{1}{N-1} \sum_{i=1}^{N-1} s_i \quad (3.29)$$

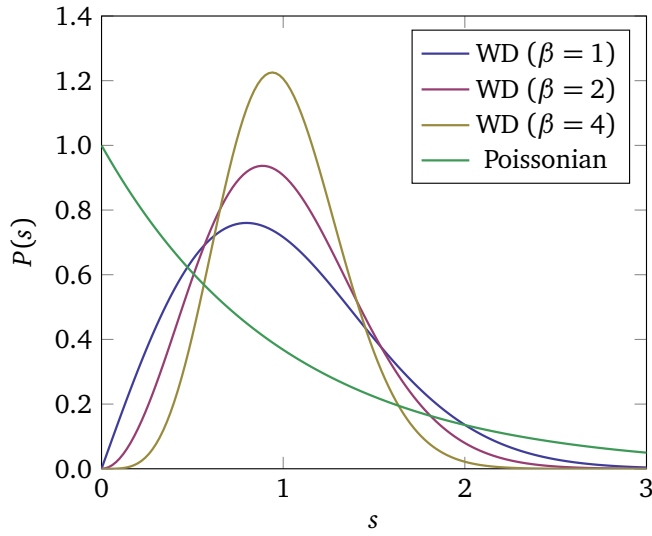


Fig. 3.1: The level spacing distribution for Wigner-Dyson (WD) and Poissonian level statistics. The curves for Wigner-Dyson level statistics represent eq. (3.31).

is unity, a direct result with standard results from random matrix theory can be made. If a spectrum has a non-uniform density of states $\rho(E)$, this can be acquired by an appropriate scaling

$$E_i \rightarrow \tilde{E}_i = \int_{-\infty}^{E_i} \frac{1}{\rho(\epsilon)} d\epsilon \quad (3.30)$$

of the spectrum, a procedure known as *unfolding* (see for example section 4.8 the book ‘Quantum Signatures of Chaos’ by Haake [52]).

An arguably surprising result is that the probability distributions $P(s)$ for the level spacings can be approximated qualitatively well by considering random matrices of dimension 2×2 . The resulting probability distributions for the level spacings are known as the *Wigner surmise*, and can be read off from eq. (3.17) with $N = 2$ directly as

$$P(s) = a_\beta s^\beta e^{-b_\beta s^2}, \quad (3.31)$$

where a_β and b_β are constants fixing both the normalization and average level spacing to 1. For integrable systems, the energy levels are uncorrelated, due to which the level spacing distribution is Poissonian, $P(s) = \exp(-s)$.

Fig. 3.1 shows $P(s)$ as given by eq. (3.31) and for Poissonian distributed level spacings. A qualitative difference between the curves is the scaling of $P(s)$ near $s = 0$. One observes $P(0) = 0$ for Wigner-Dyson level statistics, which is called *level repulsion* originating from the Coulomb gas analogy as discussed in section 3.3.2.

3.5.2 Distribution of ratios of consecutive level spacings

The distribution of the ratios of consecutive level spacings was first proposed by Oganesyanyan and Huse in 2007 [17] as an alternative for the level spacing distribution to discriminate between Poissonian and Wigner-Dyson level statistics. Because of the important role in the remainder of this dissertation, this probe is discussed in a separate section. The motivation to consider ratios of consecutive level spacings is two-fold:

1. Determining the level spacing distribution requires an energy spectrum to be unfolded, meaning that the spacings between consecutive energy levels are scaled such that the average equals 1 in every part of the spectrum. Determining ratios of consecutive level spacings does not require a spectrum to be unfolded.
2. The *average* ratio of consecutive level spacings (see also section 2.5.1) provides a natural statistic to quantify intermediate level statistics in between Poissonian and Wigner-Dyson.

Both points are clarified in the remainder of this section.

The distribution of the ratios of consecutive level spacings was first investigated by Atas, Bogomolny, Giraud, and Roux in 2013 [25]. Following this reference, the focus is on an energy spectrum

$$\{E_i\}_{i=1}^N \quad (E_1 \leq E_2 \leq \dots \leq E_N) \quad (3.32)$$

with the elements sorted in ascending order. The ratios of consecutive level spacings r_i ($i = 1, 2, \dots, N - 2$) are defined as

$$r_i = \min\left(\tilde{r}_i, \frac{1}{\tilde{r}_i}\right), \quad \tilde{r}_i = \frac{E_{i+2} - E_{i+1}}{E_{i+1} - E_i}. \quad (3.33)$$

For the eigenvalues of the Gaussian invariant ensembles, the distribution of the ratios of consecutive level spacings can be evaluated analytically only for small values of N [53], as might be expected.

Consider the Gaussian invariant ensembles with $N = 3$, such that $P(E_1, E_2, E_3)$ is given by eq. (3.17) for the appropriate value of β . The probability distribution for \tilde{r} (note the tilde) is then given by

$$P(\tilde{r}) = \int_{-\infty}^{\infty} dE_2 \int_{-\infty}^{E_2} dE_1 \int_{E_2}^{\infty} dE_3 P(E_1, E_2, E_3) \delta\left(\tilde{r} - \frac{E_3 - E_2}{E_2 - E_1}\right). \quad (3.34)$$

The distributions of $P(\tilde{r})$ and $P(1/\tilde{r})$ are trivially the same. It can be shown that this statement holds generically in the bulk of a spectrum, where boundary effects are negligible. From a mathematical viewpoint, this means that

$$P(\tilde{r}) = \frac{1}{\tilde{r}^2} P\left(\frac{1}{\tilde{r}}\right). \quad (3.35)$$

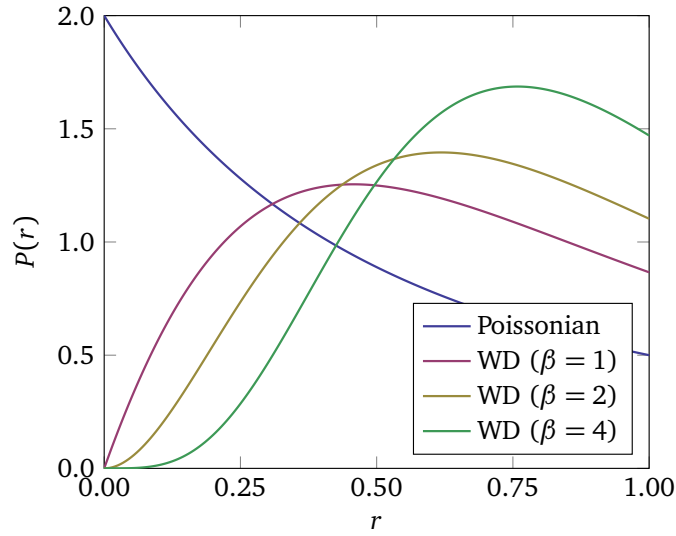


Fig. 3.2: The distribution of the ratios of consecutive level spacings for Wigner-Dyson (WD) and Poissonian level statistics. The curves for Wigner-Dyson level statistics represent eq. (3.31).

from which it follows that $P(r) = 2P(\tilde{r})\Theta(1-r)$ where Θ denotes the Heaviside step function. Note that $r \in [0, 1]$. Evaluating the integral in eq. (3.34) and substituting the result in eq. (3.35) gives the Wigner-like surmise (in the sense that it is evaluated for the smallest possible matrix dimension) reading

$$P(r) = \frac{1}{C_\beta} \frac{(r+r^2)^\beta}{(1+r+r^2)^{1+(3/2)\beta}}, \quad (3.36)$$

where C_β is again a normalization constant. For Poissonian level statistics, one finds trivially $P(r) = 1/(1+r)^2$. Fig. 3.2 shows plots of eq. (3.36) for $\beta \in \{1, 2, 4\}$ as well as the expression for Poissonian level statistics. These curves are rather accurate (less than 1% deviation) for the statistics of the Gaussian invariant ensembles at $N = 1000$, as is verified numerically in the reference.

The distribution of the ratios of consecutive level spacings for the Wigner-like surmise obeys two non-generic properties. For small values of r , a scaling $P(r) \sim r^\beta$ can be observed. It has been argued that this scaling holds for generic N in ref. [53]. Next, the relation $P(r) = r^{-2}P(r^{-1})$ as established in eq. (3.35) relates $P(r)$ and the derivative with respect to r at $r = 1$. Taking the derivative of with respect to r on both sides of this equation yields

$$\frac{d}{dr}P(r) = -\frac{1}{r^4} \left[rP\left(\frac{1}{r}\right) + \frac{d}{dr}P\left(\frac{1}{r}\right) \right] \quad (3.37)$$

$$\implies P(1) = -\left. \frac{d}{dr}P(r) \right|_{r=1}. \quad (3.38)$$

Note that also this property is valid for generic values of N .

	Poissonian	WD ($\beta = 1$)	WD ($\beta = 2$)	WD ($\beta = 4$)
$\langle r \rangle$ ($N = 3$)	0.38629	0.53590	0.60266	0.67617
$\langle r \rangle$ ($N = 1000$)	0.38629	0.5307(1)	0.5996(1)	0.6744(1)

Table 3.1: The average ratio of consecutive level spacings $\langle r \rangle$ for Poissonian and Wigner-Dyson (WD) statistics, the latter being obtained from the eigenvalues of random matrices sampled from the Gaussian invariant ensembles. The data is obtained from ref. [25]. Results for matrices of dimension $N = 10^5$ obtained by the author can be found in table 4.1 below.

The density of states does not vary within small windows for large-dimensional random matrices, while it obviously does for matrices of dimension $N = 3$. In view of this, the close agreement between $P(r)$ for matrices of dimensions $N = 3$ and $N = 1000$ can be seen as surprising.

As mentioned above and illustrated in section 2.5.1, the average ratio of consecutive level spacings given by

$$\langle r \rangle = \int_0^1 r P(r) dr \quad (3.39)$$

can be used as a probe to distinguish between Poissonian and Wigner-Dyson level statistics. Table 3.5.2 shows $\langle r \rangle$ determined for matrices sampled from the Gaussian invariant ensembles of dimension $N = 3$ and $N = 1000$, the latter obtained numerically. Notice the close agreement for $N = 3$ and $N = 1000$, illustrating the accuracy of the $N = 3$ expression (‘Wigner-like surmise’) of eq. (3.36).

3.6 Fixed-trace Wishart ensembles

As discussed in section 2 of this chapter, the Gaussian orthogonal, unitary, and symplectic ensembles are invariant under rotations of the basis. As a consequence, the elements of a single eigenvector can be considered as independent samples from a Gaussian distribution with mean zero, subject to the normalization constraint. An application of random matrix theory for the statistics of eigenstates is encountered in the context of entanglement.

3.6.1 Schmidt spectra

This section discusses part of the content covered in section 3.3.4 of the book ‘Log-Gases and Random Matrices’ by Forrester [41]. Consider a quantum system divided into subsystems A and B with respective Hilbert space dimensions M and N . A state $|\psi\rangle$ of the composite system can be expanded in basis states $|a_i\rangle$ and $|b_i\rangle$ for the respective

subsystems as

$$|\psi\rangle = \sum_{i,j} X_{ij} |a_i\rangle \otimes |b_j\rangle, \quad (3.40)$$

where X is an $M \times N$ matrix. Labeling the subsystems such that $M \geq N$, a Schmidt decomposition of X uniquely expands $|\psi\rangle$ as a linear combination of product states over the subsystems as

$$|\psi\rangle = \sum_{i=1}^N \sqrt{\lambda_i} |v_i^A\rangle \otimes |v_i^B\rangle, \quad (3.41)$$

where $|v_i^A\rangle$ and $|v_i^B\rangle$ are basis states for respectively subsystems A and B , and λ_i is the *Schmidt spectrum*. The Schmidt spectrum fully encodes the entanglement between subsystems A and B . Details on the procedure can be found in section 7.4 below.

In physical terms (see also section 2.5.2), the Schmidt spectrum can be interpreted as set of eigenvalues of the reduced density matrix of subsystem B . Again, consider a state $|\psi\rangle$. This state is associated with the reduced density matrix $\rho = |\psi\rangle\langle\psi|$. Tracing out the degrees of freedom of subsystem A gives the reduced density matrix ρ_B of subsystem B given by

$$\rho_B = \text{Tr}_A(|\psi\rangle\langle\psi|). \quad (3.42)$$

The reduced density matrix ρ_B of subsystem B encodes all physical information accessible by a measurement on subsystem B only. The elements λ_i ($i = 1, 2, \dots, N$) of the Schmidt spectrum give the probability to find the system in the associated eigenstate. Consequently, the Schmidt spectrum obeys

$$\sum_{i=1}^N \lambda_i = 1, \quad (3.43)$$

which is known as the *fixed-trace* constraint on reduced density matrices.

3.6.2 Wishart ensembles

This section discusses part of the content covered in section 3.2.3 of the book ‘Log-Gases and Random Matrices’ by Forrester [41]. Matrices of the form $X^\dagger X$ with the entries X_{ij} given by independent samples from a Gaussian distribution with mean zero are known as Wishart matrices. These matrices are samples from the Wishart random matrix ensembles, sometimes referred to as the Wishart-Laguerre random matrix ensembles. Similar as for the Gaussian random matrix ensembles discussed above, the Dyson index β as given in eq. (3.16) labels three types of Wishart ensembles. One distinguishes the Wishart orthogonal ($\beta = 1$), unitary ($\beta = 2$), and symplectic ($\beta = 4$) ensembles, obtained for respectively real, imaginary, or symplectic elements X_{ij} .

It can be shown that the joint probability distribution for the eigenvalues λ_i ($i = 1, 2, \dots, N$) of matrices sampled from the Wishart ensembles is given by

$$P(\lambda_1, \lambda_2, \dots, \lambda_N) = \frac{1}{C_{a,\beta,N}} \prod_{i=1}^N \lambda_i^{\beta a/2} e^{-\beta \lambda_i/2} \prod_{j < k} |\lambda_j - \lambda_k|^\beta \quad (3.44)$$

with $\lambda_i \geq 0$, where $a = M - N + 1 - 2/\beta$, and $C_{a,\beta,N}$ a normalization constant. Eq. (3.44) can be interpreted as the partition function of a Coulomb gas (see section 3 of this chapter) at inverse temperature β , for which the partition function \mathcal{Z} is given by

$$\mathcal{Z} = \int_0^\infty d\lambda_i e^{-\beta \mathcal{V}[\lambda_i]}, \quad (3.45)$$

$$\mathcal{V}[\lambda_i] = \frac{1}{2} \sum_{i=1}^N \lambda_i + \frac{1}{2} \left(M - N - 1 + 2/\beta \right) \sum_{i=1}^N \log \lambda_i - \sum_{i < j} \log |\lambda_i - \lambda_j|. \quad (3.46)$$

The gas is in equilibrium under the competing effect of a linear potential, a logarithmic potential, and pairwise electrostatic repulsion. The linear potential is attractive towards the origin. The logarithmic potential is repulsive if $\beta \geq 2/(1 + N - M)$, and attractive otherwise. The density of states in the limit $m, n \rightarrow \infty$ at fixed $c = M/N$ obeys Marčenko-Pastur law [54] discussed below.

3.6.3 Fixed-trace constraint

In the context of entanglement as sketched above, the fixed-trace constraint imposes that the elements λ_i of a Schmidt spectrum sum up to unity. The Schmidt spectra obtained from eigenstates of matrices sampled from the Gaussian invariant ensembles are thus given by sets of eigenvalues of Wishart matrices, having a joint probability distribution

$$\left[\text{eq. (3.44)} \right] \times \delta \left(\sum_{i=1}^N \lambda_i - 1 \right). \quad (3.47)$$

Remark that the fixed-trace constraint alters the normalization constant in the expression of eq. (3.44).

The effect of the fixed-trace constraint in the joint probability distribution of eq. (3.47) can be studied by considering the probability for a sample

$$\{\lambda_i\}_{i=1}^N, \quad \lambda_i = (1 + c) \lambda'_i \quad (3.48)$$

having a trace tunable by the parameter c . Elementary mathematical manipulations show that the probabilities $P(\lambda_1, \lambda_2, \dots, \lambda_n)$ and $P(\lambda'_1, \lambda'_2, \dots, \lambda'_N)$ are proportional to each other by a factor only depending on c ,

$$P(\lambda_1, \lambda_2, \dots, \lambda_N) = \left[e^{Nc} c^{\beta a N/2} c^{\beta N(N-1)} \right] P(\lambda'_1, \lambda'_2, \dots, \lambda'_N). \quad (3.49)$$

Remark that the proportionality factor does not depend on the λ'_i . This proportionality relation shows that samples from eq. (3.47) can be obtained from samples from eq. (3.44) by a proper rescaling of the λ_i [55].

3.6.4 Marčenko-Pastur law

This section uses section 14.1 of the book ‘Introduction to Random Matrices’ by Livan, Novaes, and Vivo [44] as the main reference. As for Wigner’s semicircle law for the Gaussian invariant ensembles, the eigenvalue density for the Wishart ensembles can be obtained by making a continuum approximation. The eigenvalue density $\rho(x)$ given by

$$\rho(x) = \sum_{i=1}^N \delta(x - \lambda_i) \quad (3.50)$$

converges in the limit $n, m \rightarrow \infty$ with $c = n/m$ kept fixed after proper rescaling to

$$\rho(x) = \begin{cases} \frac{1}{2\pi x} \sqrt{(x - \xi_-)(\xi_+ - x)} & \text{if } x \in [\xi_-, \xi_+], \\ 0 & \text{if } x \notin [\xi_-, \xi_+], \end{cases} \quad (3.51)$$

where $\xi_{\pm} = (1 \pm c^{-1/2})^2$. Eq. (3.51) is known as the Marčenko-Pastur law [54]. The Marčenko-Pastur law can be for example to estimate the entanglement entropy of ergodic states [32]. Note that for $c < 1$ (meaning that $N \neq M$) there is a lower value ξ_- below which no eigenvalues are found.

Level statistics across the many-body localization transition

4.1 Introduction

In the thermodynamic limit of large system sizes, many-body localized and ergodic phases are believed to be separated by a phase transition known commonly referred to as the many-body localization transition, as suggested by finite-size scaling analysis [8, 27]. At finite system sizes, the transition becomes a crossover, leading to the observation of intermediate phenomena [8, 18]. This chapter focuses on level statistics along the crossover from an ergodic to a many-body localized phase. The results presented in this chapter are published in ref. [2].

Apart from the potential intrinsic interest and technical convenience, there are several motivations to consider level statistics when studying crossovers from ergodic to many-body localized phases, including:

1. Level statistics do not depend on the basis in which the Hamiltonian is formulated. As a result, level statistics provide an ‘agnostic’ probe. Some aspects of basis dependence in the context of many-body localization are discussed in chapter 6.
2. Typically, eigenvalues of matrices can be obtained at a significantly lower computational costs than eigenvectors (see appendix B for a discussion). Level statistics are thus relatively computationally cheap to obtain.

In the context of many-body localization, intermediate level statistics have been studied rather extensively (see section 4.2 below for a review).

This chapter proposes the Gaussian beta ensemble [56] as a one-parameter random matrix model for the intermediate level statistics along the crossover from the ergodic to the many-body localized phase for the ‘standard model of many-body localization’, discussed in section 2.6. At the level of eigenvalues, the Gaussian beta ensemble is a generalization of the Gaussian invariant random matrix ensembles from the discrete set of Dyson indices $\beta \in \{1, 2, 4\}$ to the continuous range $\beta \in (0, \infty)$. The level statistics of this ensemble, providing a smooth interpolation between Poissonian and Wigner-Dyson, are interpreted as generalized Wigner-Dyson level statistics.

Section 2 briefly reviews existing results on intermediate level statistics along crossovers from ergodic to many-body localized phases. The Gaussian beta ensemble is introduced in sections 3 and 4. The eigenvalue statistics of this ensemble are compared with the intermediate level statistics in sections 5 – 7. A discussion of the results and proposals for future research are discussed in section 8.

4.2 Literature review

Historically, the problem of intermediate level statistics was studied first in the context of heavy atomic nuclei [57]. Concerning the level spacing distribution, a simple interpolation between Poissonian and Wigner-Dyson level statistics was proposed by Brody in 1973 [58]. On phenomenological grounds, it is argued that the intermediate level statistics of unfolded spectra approximately obey

$$P(s) = a_\beta s^\beta \exp\left[-b_\beta s^{\beta+1}\right], \quad (4.1)$$

where a_β and b_β fix the normalization and average level spacing to unity, and β (in the reference denoted by ω) is a fitting parameter tuning the degree of level repulsion. For $\beta = 0$ one recovers Poissonian level statistics, while for $\beta = 1$ the expression coincides with Wigner's surmise as given in eq. (3.31). This distribution was shown to match experimental data at a qualitative level [59].

For the crossover from ergodic to many-body localized phases, intermediate level statistics have been investigated by Serbyn and Moore in 2016 [60]. In this work, a Coulomb gas picture as discussed in section 3.3.2 of the energy spectra is adapted. In intermediate phases, the potential energy due to interactions between two particles (energy levels) at positions λ_1 and λ_2 is argued to scale as

$$U \sim |\lambda_1 - \lambda_2|^{-\gamma}, \quad (4.2)$$

where $\gamma \leq 1$ is a parameter. Remark that this potential strictly does not describe a Coulomb gas as the potential does not scale logarithmically. Compared to the scaling $U \sim \ln|\lambda_1 - \lambda_2|$ for Wigner-Dyson statistics, the interactions described by this potential are short-ranged. At the same time, it is qualitatively different from the scaling $U \sim \text{constant}$ for many-body localized phases (Poissonian level statistics).

It is argued that the distribution of level spacings capturing these characteristics can be approximated by a generalization of eq. (4.1) reading

$$P(s) = a_\beta s^\beta \exp\left[-b_\beta s^{2-\gamma_p}\right], \quad (4.3)$$

where γ_p (allowed to differ from γ) is a second fitting parameter. Qualitative numerical evidence for the validness of eq. (4.3) is provided. Motivated by the suggestion that U is short-ranged at the transition point from the ergodic to the many-body localized phase,

it is conjectured that the many-body localization transition are ‘critical’, different from Poissonian and Wigner-Dyson, in analogy with Anderson [61] and certain topological [62] transitions.

A different approach was adapted by Kravtsov, Khaymovich, Cuevas, and Amini in 2015 [63]. The starting point is a generalization of the Gaussian invariant ensembles proposed by Rosenzweig and Porter [57]. For the Gaussian orthogonal ensemble, the generalization of consists of real symmetric matrices for which the diagonal and upper triangular elements are sampled independently from probability distributions

$$P(x) = \frac{1}{\sqrt{2\pi}} e^{-x^2/2}, \quad P(x) = \frac{1}{\sqrt{\pi}} e^{-(x/\sigma)^2}, \quad (4.4)$$

respectively. The diagonal elements are sampled from a Gaussian distribution with mean 0 and variance 1, while the upper triangular elements are sampled from a Gaussian distribution with mean 0 and variance $\sigma/2$. Note that for $\sigma = 1$ the Gaussian orthogonal ensemble as defined in eq. (3.15) is recovered. The parameter σ is parametrized as

$$\sigma = 2\lambda^2/N^\gamma \quad (4.5)$$

with N denoting the dimension of the matrices, where λ is a constant, and γ is a control parameter. It is shown that in the limit $N \rightarrow \infty$ this random matrix ensemble exhibits 2 transitions:

1. At $\gamma = 2$, there is a transition from localized ($\gamma > 2$) to extended eigenstates. These eigenstates are spread out over a large but non-extensive number of basis states.
2. At $\gamma = 1$, there is a transition from extended to ergodic eigenstates that spread out over an extensive number of basis states.

It is proposed that the ergodic, intermediate, and many-body localized phases obey the statistics of the phases found for respectively $\gamma \leq 1$, $1 < \gamma \leq 2$, and $\gamma > 2$. At the level of eigenvalues, it was observed numerically by Sierant and Zakrzewski in 2019 [64] that this picture is correct at a qualitative level.

The above-cited work by Sierant and Zakrzewski [64] puts forward a yet different view on intermediate level statistics. A Coulomb gas model in which β is a random variable to account for sample-to-sample variations in the disorder is proposed. As for the model proposed by Serbyn and Moore, the intermediate phase is characterized by short-ranged interactions, although inspired by a short-range plasma model proposed by Bogomolny, Gerland, and Schmit in 2001 [65] and thus of a different form than eq. (4.2). The model is shown to be quantitatively correct, although this could be related to the relatively large number of fitting parameters.

example ref. [37]). Before the appearance of the work by Dumitriu and Edelman [56], no random matrix ensembles with the joint eigenvalue distribution given by eq. (4.6) were known.

2. The invariance of the Gaussian invariant ensembles under rotations of the basis (see section 3.2) does not hold for the Gaussian beta ensemble. Thus, the Gaussian beta ensemble can *not* be thought of as a full generalization of the Gaussian invariant ensembles.

It is a potentially interesting and (to the knowledge of the author) open question if a natural generalization of the Gaussian invariant ensembles beyond $\beta \in \{1, 2, 4\}$ for the eigenvectors can be constructed.

It was proven by Benaych-Georges and P ech e in 2015 [66] that the eigenvalues of the Gaussian beta ensemble are uncorrelated in the combined limit

$$\beta \rightarrow 0, \quad N \rightarrow \infty, \quad N\beta \rightarrow 0 \quad (4.10)$$

on windows in which the density of states is uniform, meaning that Poissonian level statistics are obeyed. From this, one can conclude that the Gaussian beta ensemble provides an interpolation between Poissonian ($\beta \rightarrow 0$) and Wigner-Dyson ($\beta \in \{1, 2, 4\}$) level statistics. Additional numerical evidence is provided below.

An intuition for the occurrence of Poissonian level statistics for $\beta \rightarrow 0$ can be obtained from the notion that β gives the number of degrees of freedom per upper triangular matrix element for the Gaussian invariant ensembles. This suggests that $\beta = 0$ corresponds to an ensemble of diagonal matrices, characterized by uncorrelated eigenvalues. A similar intuition could be obtained from the interpretation of the joint eigenvalue distribution of the Gaussian beta ensemble as the Boltzmann factor of a Coulomb gas (outlined in section 3.3.2), where β is an inverse temperature.

4.4 Eigenvalue statistics for intermediate beta

The Gaussian beta ensemble provides a random matrix model for intermediate level statistics, smoothly interpolating between Poissonian ($\beta \rightarrow 0$) and Wigner-Dyson ($\beta \in \{1, 2, 4\}$). This section numerically explores the eigenvalue statistics for the Gaussian beta ensemble for the intermediate values $\beta \in (0, 1)$.

4.4.1 Numerical implementation

Eigenvalue statistics of the Gaussian beta ensemble are obtained by numerically diagonalizing matrices T sampled from the matrix model discussed in section 4.3. Alternatively, data could for example be obtained by Monte Carlo simulations. Aiming to minimize finite-size (boundary) effects, the focus is restricted to elements near the middle of the eigenvalue spectra.

Matrices are diagonalized using an iterative algorithm based on the inverse power method [67]. For a general introduction to iterative inverse algorithms in the context of many-body localization, the reader is referred to ref. [68]. The inverse power method works in two steps:

1. The inverse matrix T^{-1} is considered. The eigenvalues of T^{-1} are given by the reciprocals of the eigenvalues of T . The eigenvalues of interest can thus be computed from the largest-modulus eigenvalues of T^{-1} .
2. The power method is used to find the largest-modulus eigenvalues of T^{-1} , from which the corresponding smallest-modulus eigenvalues of T are computed. This method utilizes that the iterative application of a random vector on T^{-1} yields the (unnormalized) eigenvector corresponding to the largest-modulus eigenvalue.

When properly implemented, the inverse power method does not require the actual computation of T^{-1} , which is in computational costs comparable to full diagonalization. Instead, solving a matrix equation of the form $T\vec{x} = \vec{y}$ at each iteration is sufficient. A more detailed discussion of the inverse power method and the implementation can be found in section 2 of appendix B.

Matrix diagonalizations are performed using the `eigs` function (default options) of MATLAB release 2017a [69], which uses the ARPACK library. For each value of β , statistics are obtained from at least 10^4 matrix realizations of dimension $N = 10^5$. For each matrix realization, the focus is restricted to the 100 eigenvalues closest to 0. Per value of β , the data is obtained in $\mathcal{O}(10)$ hours of computational time on a desktop computer. The default random number generator is used.

For each of the results presented below, only negligible deviations can be observed when comparing with results for matrices of dimension 10^4 . As for the Gaussian invariant ensembles, the density of eigenstates obeys Wigner's semicircle law as discussed in section 3.3.3 [46]. Aiming to maximize the accuracy of the results, unfolding according to Wigner's semicircle law by using eq. (3.30) is performed before analysis.

4.4.2 Evaluations

As discussed in section 3.5.2, the average ratio of consecutive level spacings can be used as a measure for how close level statistics are to Poissonian or Wigner-Dyson. For n ascendingly ordered eigenvalues $\{\lambda_i\}_{i=1}^N$ ($\lambda_1 \leq \lambda_2 \leq \dots \leq \lambda_N$) of a matrix realization, the average ratio of consecutive level spacings $\langle r \rangle$ is given by

$$\langle r \rangle = \frac{1}{N-2} \sum_{i=1}^{N-2} r_i, \quad r_i = \min\left(\frac{\lambda_{i+2} - \lambda_{i+1}}{\lambda_{i+1} - \lambda_i}, \frac{\lambda_{i+1} - \lambda_i}{\lambda_{i+2} - \lambda_{i+1}}\right). \quad (4.11)$$

Additional averaging over matrix realizations is performed. Fig. 4.1 shows $\langle r \rangle$ for several $\beta \in [0, 1]$. One observes a one-to-one correspondence between β and $\langle r \rangle$. In the remainder of this chapter, β is estimated from $\langle r \rangle$ when comparing the level

β	0.00	0.01	0.05	0.10	0.15	0.20
$\langle r \rangle$	0.3863	0.389(0)	0.398(4)	0.408(9)	0.410(1)	0.429(5)
β	0.25	0.30	0.35	0.40	0.45	0.50
$\langle r \rangle$	0.438(1)	0.446(2)	0.453(6)	0.461(7)	0.469(3)	0.475(8)
β	0.55	0.60	0.65	0.70	0.75	0.80
$\langle r \rangle$	0.482(6)	0.489(0)	0.494(6)	0.500(8)	0.505(8)	0.511(2)
β	0.85	0.90	0.95	1.00	2.00	4.00
$\langle r \rangle$	0.516(4)	0.521(5)	0.526(2)	0.530(2)	0.599(7)	0.673(9)

Table 4.1: The average ratio $\langle r \rangle$ of consecutive level spacings as a function of β for the Gaussian beta ensemble. See the main text for computational details.

statistics of the physical model with the eigenvalue statistics of the Gaussian beta ensemble. For this purpose, the data displayed in the figure is shown in table 4.1.

Next, the distributions of the level spacings and the ratios of consecutive level spacings are considered. For N ascendingly ordered eigenvalues $\{\lambda_i\}_{i=1}^N$ ($\lambda_1 \leq \lambda_2 \leq \dots \leq \lambda_N$) of a matrix realization, the probability distributions for the level spacings $s_i = \lambda_{i+1} - \lambda_i$ and the ratios of consecutive level spacings r_i are given respectively by

$$P(s) = \frac{1}{N-1} \sum_{i=1}^{N-1} \delta(s_i - s), \quad P(r) = \frac{1}{N-2} \sum_{i=1}^{N-2} \delta(r_i - r). \quad (4.12)$$

As before, additional averaging over a large number of matrix realizations is performed. Figs. 4.2 and 4.3 show respectively $P(s)$ and $P(r)$ for several values of $\beta \in [0, 1]$. Because of the limited number of samples, some noise can be observed. The curves for $\beta = 0$ (Poissonian statistics) are plotting the exact expressions $P(s) = \exp(-s)$ and $P(r) = 1/(1+r)^2$ as given respectively below eqs. (3.31) and (3.36). Note that the average level spacing equals 1 as a result of the unfolding.

4.5 Agreement with intermediate level statistics

This chapter aims to argue that the intermediate level statistics along the crossover from the ergodic to the many-body localized phase for the ‘standard model of many-body localization’ discussed in section 2.6 are captured by the eigenvalue statistics of the Gaussian beta ensemble. Below, a number of comparisons between the eigenvalue statistics of the Gaussian beta ensemble and the level statistics of the physical model are discussed.

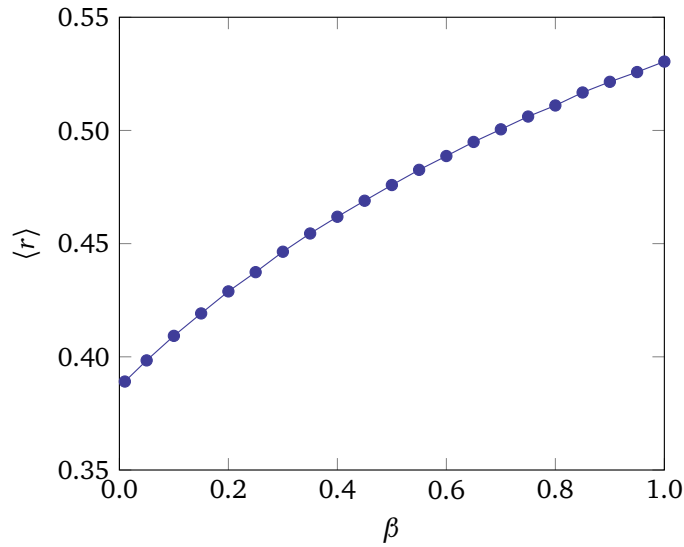


Fig. 4.1: The average ratio of consecutive level spacings for the Gaussian beta ensemble at several $\beta \in [0, 1]$. The line connecting the data points serves as a guide to the eye. Error bars are significantly smaller than the marker size. See the main text for computational details.

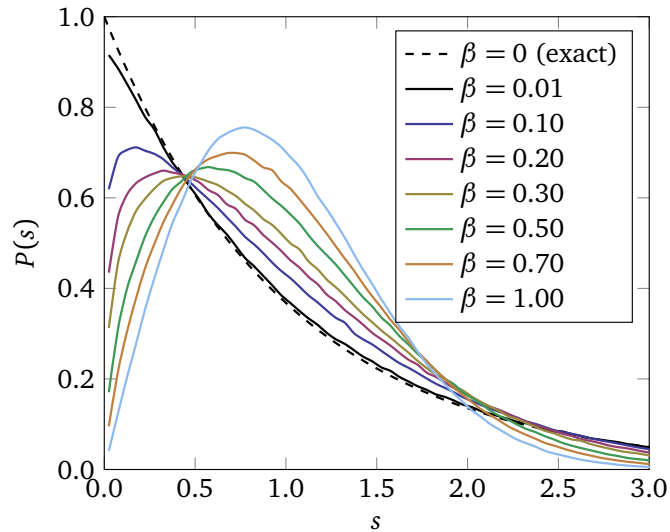


Fig. 4.2: The level spacing distribution for the unfolded Gaussian beta ensemble at several $\beta \in [0, 1]$. The curve for $\beta = 0$ (Poissonian statistics) is obtained analytically. Because of the limited number of samples, some noise can be observed. See the main text for computational details.

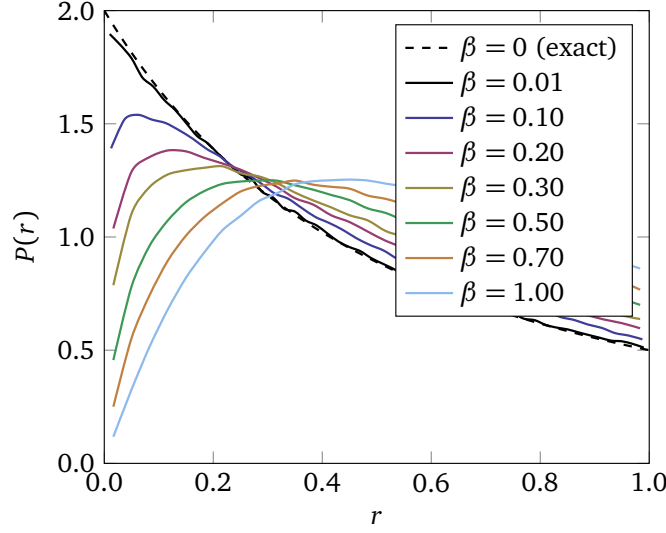


Fig. 4.3: The distribution of the ratios of consecutive level spacings for the Gaussian beta ensemble at several $\beta \in [0, 1]$. The curve for $\beta = 0$ (Poissonian statistics) is obtained analytically. Because of the limited number of samples, some noise can be observed. See the main text for computational details.

4.5.1 Model and parameters

The focus is on the ‘standard model of many-body localization’ discussed in section 2.6. The motivation to consider this model is that it allows for a comparison of the results with what is known from the literature. Recapitulating, the model describes a spin-1/2 XXX-chain appended by random onsite disorder. The Hamiltonian H is given by

$$H = \sum_{i=1}^L \left[S_i^x S_{i+1}^x + S_i^y S_{i+1}^y + S_i^z S_{i+1}^z + h_i S_i^z \right], \quad (4.13)$$

where L is the total number of sites. The spin-1/2 operators $S_i^{x,y,z}$ are defined in eq. (2.26). Periodic boundary conditions $S_{L+1}^{x,y,z} \equiv S_1^{x,y,z}$ are imposed. The total spin $S^z = \sum_{i=1}^L S_i^z$ is a conserved quantity, meaning that $[H, S^z] = 0$. The focus is on the $S^z = 0$ symmetry sector. The onsite potentials h_i ($i = 1, 2, \dots, L$) are sampled independently from the probability distribution

$$P(x) = \begin{cases} 1/(2W) & \text{if } |x| \leq W, \\ 0 & \text{if } |x| > W, \end{cases} \quad (4.14)$$

which corresponds to the uniform distribution ranging over the interval $[-W, W]$. The phase diagram for this model indicating ergodic and many-body localized phases has been established numerically in ref. [27].

Unless stated otherwise, all results in this chapter are for $L = 16$, which is the largest possible system size for which exact diagonalization methods (discussed below) can

be used to obtain statistics over sufficiently many disorder realizations (≥ 1000) in a reasonable amount of time. The disorder strength W (defined in eq. (4.14)) is used as a tuning parameter enabling one to explore the phase diagram.

The focus is restricted to the middle part of the energy spectra. Let $E_i^{(j)}$ denote the i -th element of the energy spectrum obtained for the j -th disorder realization. The index i runs over $1, 2, \dots, \dim(H)$ whereas j runs over $1, 2, \dots, N$ with N denoting the total number of disorder realizations. At the ensemble level, the density of states $\rho(E)$ is given by

$$\rho(E) = \frac{1}{\dim(H) \times N} \sum_{i,j} \delta(E_i^{(j)} - E_i). \quad (4.15)$$

Remark that for $N \rightarrow \infty$ the density of states becomes independent of N . The data analysis below is concerned only with energy levels in the interval $[E_{\min}, E_{\max}]$ defined implicitly by

$$\int_{-\infty}^{E_{\min}} \rho(E) dE = 0.45, \quad \int_{-\infty}^{E_{\max}} \rho(E) dE = 0.55. \quad (4.16)$$

Roughly, the selection matches the selection of states with an energy density (defined in eq. (2.29)) ϵ in the range $\epsilon \in [0.45, 0.55]$. The motivation not to adapt the energy density as a selection criterion is that it is arguably too strongly dependent on the values of the energies associated with the ground state and the highest excited state. The bandwidth is chosen such that level statistics are uniform over the full band at a qualitative level.

4.5.2 Numerical implementation

Energy spectra are obtained by exact diagonalization of Hamiltonians using the `eig` function (default options) of MATLAB version 2017a [69], which uses the ARPACK library. The computational algorithm is based on the QR diagonalization scheme [70], which is discussed in section 3 of appendix B. Contrary to the algorithm used to find the eigenvalues of matrices sampled from the Gaussian beta ensemble, the QR diagonalization scheme is designed to find all eigenvalues of a matrix. There are two motivations to consider full spectra:

1. The Hamiltonian for the physical model can not be trivially represented as a tridiagonal matrix, contrary to realizations of the Gaussian beta ensemble. Presumably related to this (see also the appendix referred to above), the loss in computational complexity of using an iterative inverse algorithm turns out to be limited.
2. In the evaluation of level spacing distributions, unfolding is applied. It appears that the numerical procedure for this yields proper results only when a significantly larger part of the spectrum than is analyzed is available, which advocates in favor of using an algorithm designed to find full spectra.

For each disorder strength W , at least 1000 disorder realizations are considered. On a desktop computer, this diagonalization task requires $\mathcal{O}(1 \text{ week})$ of computational time.

4.5.3 Evaluations

The first step in comparing the level statistics of the physical model with the eigenvalue statistics of the Gaussian beta ensemble is to estimate the value of β corresponding to a given disorder strength W . As indicated above, β is estimated from the average ratio of consecutive level spacings. Analog to eq. (4.17), the average ratio $\langle r \rangle$ of consecutive level spacings for an ascendingly ordered set of energy levels $\{E_i\}_{i=1}^N$ ($E_1 \leq E_2 \leq \dots \leq E_N$) is given by

$$\langle r \rangle = \frac{1}{N-2} \sum_{i=1}^{N-2} r_i, \quad r_i = \min \left(\frac{E_{i+2} - E_{i+1}}{E_{i+1} - E_i}, \frac{E_{i+1} - E_i}{E_{i+2} - E_{i+1}} \right). \quad (4.17)$$

As before, additional averaging over disorder realizations is performed. The dependence of $\langle r \rangle$ on β is given in table 4.1. The value of $\langle r \rangle$ for β intermediate between two data points is estimated from an interpolation by a third order polynomial. Only tiny deviations in the estimated value of β are observed when interpolating with polynomials of order 1, 2, or 4.

The first comparison between the level statistics of the physical model and the eigenvalue statistics of the Gaussian beta ensemble is made by focusing on the distribution of the ratios of consecutive level spacings, for the $\{r_i\}_{i=1}^{N-2}$ mentioned above analog to eq. (4.12) given by

$$P(r) = \frac{1}{N-2} \sum_{i=1}^{N-2} \delta(r - r_i). \quad (4.18)$$

Also here, additional averaging over disorder realizations is performed. Fig. 4.4 shows $P(r)$ for the energy levels of the physical model (solid lines) and the eigenvalues of the Gaussian beta ensemble (dashed lines). The estimated values of β are indicated in the legend. One observes good agreement for all values of W , which marks the main result presented in this chapter.

The second comparison is made by focusing on the level spacing distribution. For a fair comparison between the level spacing distributions of the physical model and the Gaussian beta ensemble, spectra need to be unfolded. A spectrum $\{E_i\}_{i=1}^N$ with a smoothed density of states $\rho(E)$ is unfolded by the transformation

$$E_i \rightarrow \tilde{E}_i = \int_{-\infty}^{E_i} \frac{1}{\rho(\epsilon)} d\epsilon. \quad (4.19)$$

Supposing that the elements of the spectrum are labeled such that $\tilde{E}_1 \leq \tilde{E}_2 \leq \dots \leq \tilde{E}_N$, the level spacings $\{s_i\}_{i=1}^{N-1}$ and the mean level spacing $\langle s \rangle$ are given analog to eq. (3.28)

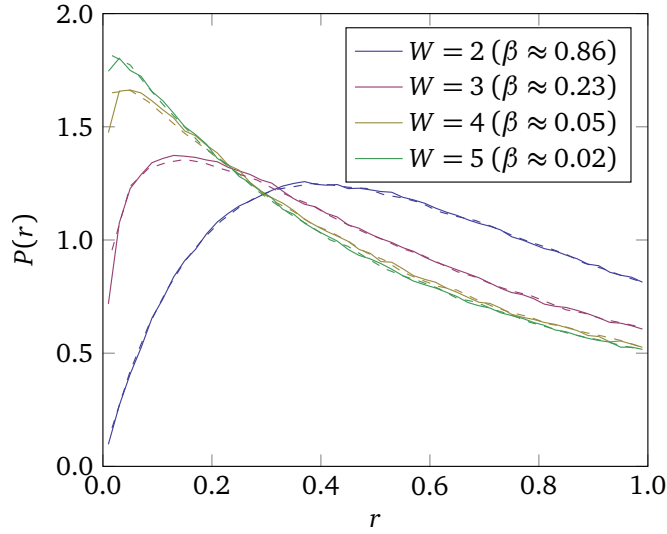


Fig. 4.4: The distribution of the ratios of consecutive level spacings for the physical model at several W (solid lines) combined with corresponding distributions for the Gaussian beta ensemble (dashed lines). Solid and dashed lines obey the same color scheme. The estimated values of β are indicated in the legend.

by

$$s_i = \tilde{E}_{i+1} - \tilde{E}_i, \quad \langle s \rangle = \sum_{i=1}^{N-1} s_i, \quad (4.20)$$

with $\langle s \rangle = 1$ due to the unfolding. For the Gaussian beta ensemble, the smoothed density of states is known to be well approximated by the Wigner semicircle (see section 4.4.1).

Unfolding is accomplished using the function `SmoothKernelDistribution` of the mathematical software package `MATHEMATICA` version 10.0 [71]. For a collection $\{x_i\}_{i=1}^N$ of samples, this function returns an estimate of the smoothed probability distribution

$$P(x) = \left\langle \sum_{i=1}^n \delta(x_i - x) \right\rangle, \quad (4.21)$$

where $\langle \cdot \rangle$ denotes an ensemble average. As an illustrative example, the function is expected to return a function resembling $P(x) = (\sqrt{2\pi}\sigma)^{-1} \exp[-(x - \mu)^2 / (2\sigma^2)]$ if the x_i are sampled from the Gaussian distribution with mean μ and variance σ^2 .

Energy spectra originating from different disorder realizations are unfolded separately. For disorder strengths $W = 2$ and $W = 3$, the function is used with bandwidth specification `{‘‘Adaptive’’, Automatic, 1}`, `‘‘Biweight’’`, while for $W = 4$ and $W = 5$ `{‘‘Adaptive’’, Automatic, 1}` is used as specification. The bandwidth specifications are tuned such that agreement between the level spacing distributions for the physical model and the Gaussian beta ensemble is optimal. Remark that the ambiguity of the

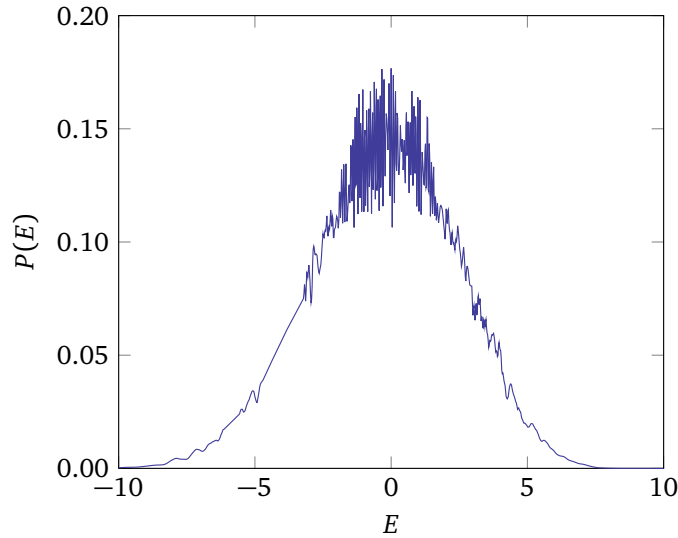


Fig. 4.5: The estimated density of states $\rho(E)$ for a single (representative) realization of the physical model for $W = 2$. See the main text for computational details.

level spacing distribution due to the unfolding makes that one can only draw conclusions up to a limited extent (see also ref. [72] for some examples of mis-interpretations due to improper unfolding).

In view of the study of longer-range statistics in section 7 of this chapter, the unfolding procedure is illustrated before presenting the main result. Fig. 4.5 shows the density of states as estimated for a single (representative) realization of the physical model with disorder strength $W = 2$. Two observations can be made:

1. The density of states appears to fluctuate rapidly, in particular near the center of the spectrum. This shows that the density of states needs to be estimated separately for each disorder realization. Averaged over disorder realizations, one expects $\rho(E)$ to be close to a Gaussian.
2. Because the average onsite disorder is different from 0 for this particular disorder realization, the Gaussian shape is shifted to the left when comparing with a Gaussian with the same variance but mean value 0. Again, this indicates that the density of states needs to be estimated separately for each disorder realization.

As a further illustration, fig. 4.6 shows the estimated density of states for three different (representative) realizations of the physical model in the vicinity of the middle of the spectra, on a window containing roughly 900 levels. This window roughly matches the window set by eq. (4.16), which is concerned in the analysis. One observes that the density of states apparently can not be fitted by a low-order polynomial.

Taking into account the considerations above, the level spacing distributions for the physical system and the Gaussian beta ensemble can be compared. Fig. 4.7 shows $P(s)$ for the energy levels of the physical model (solid lines) and the eigenvalues of the

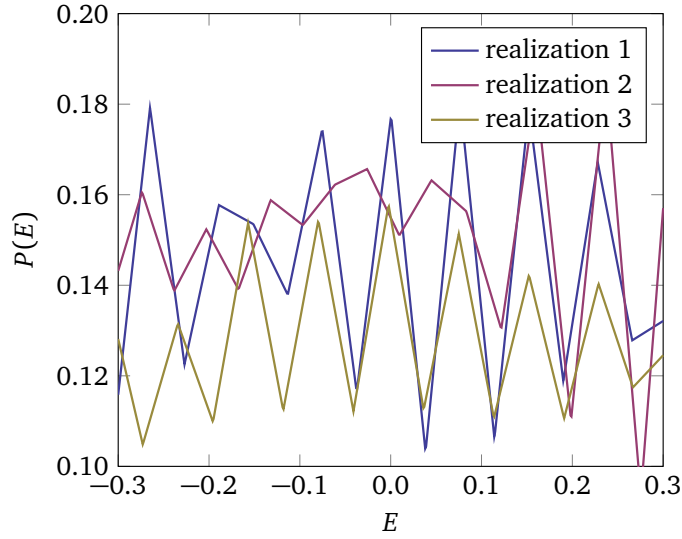


Fig. 4.6: The estimated density of states $\rho(E)$ around the middle of the spectra for some (representative) realization of the physical model for $W = 2$. Note that the vertical axis does not start at zero.

Gaussian beta ensemble (dashed lines). As in fig. 4.4, one observes good agreement for all values of W .

4.6 Breaking time-reversal symmetry

An arguably interesting question is whether the agreement observed in the former section holds beyond Dyson indices $\beta \in [0, 1]$. The Gaussian unitary ensemble, corresponding to $\beta = 2$, is a random matrix model for ergodic systems with broken time-reversal symmetry (see section 3.2). This section compares the level statistics for an extension of the ‘standard model of many-body localization’ having broken time-reversal symmetry with the eigenvalue statistics of the Gaussian beta ensemble.

In the most general form (see for example section 2.3 of ref. [52]), a time-reversal operator T can be represented as $T = UK$, where U is unitary ($UU^{-1} = \mathbb{1}$) and K performs complex conjugation. The Hamiltonian of the physical model under consideration is written down in terms of the spin-1/2 operators

$$S_i^x = \frac{1}{2} \begin{pmatrix} 0 & 1 \\ 1 & 0 \end{pmatrix}, \quad S_i^y = \frac{1}{2} \begin{pmatrix} 0 & -i \\ i & 0 \end{pmatrix}, \quad S_i^z = \frac{1}{2} \begin{pmatrix} 1 & 0 \\ 0 & -1 \end{pmatrix} \quad (4.22)$$

acting only on site i , as given in eq. (2.26). Trivially, the time-evolution operator can be expanded as a sum of terms T_i over $i \in \{1, 2, \dots, L\}$ with T_i acting only on site i . It is conventional to take $T_i = \exp(i\pi S_i^y) K$, such that all spin operators transform

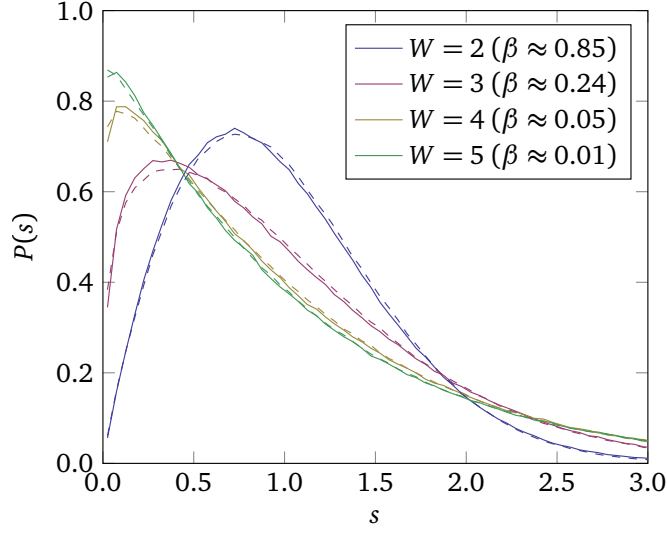


Fig. 4.7: The level spacing distribution for the physical model at several W (solid lines) combined with corresponding distributions for the Gaussian beta ensemble (dashed lines). Solid and dashed lines obey the same color scheme. The estimated values of β (as in fig. 4.4) are indicated in the legend.

similarly as $S_i^{x,y,z} \rightarrow -S_i^{x,y,z}$ under time reversal,

$$S_i^{x,y,z} \rightarrow T_i S_i^{x,y,z} T_i \quad (4.23)$$

$$= \exp(i\pi S_i^y) K S_i^{x,y,z} K \exp(-i\pi S_i^y). \quad (4.24)$$

Notice that here T_i can equivalently be written as $T_i = 2i S_i^y K$, and that $T_i^{-1} = -2i S_i^y K$ implying that $T_i^{-1} = -T_i$.

Let $\tilde{H} = THT^{-1}$ denote the Hamiltonian for the ‘standard model of many-body localization’ given in eq. (4.13) with reversed time obtained by using the time-reversal operator discussed above. One observes that $\tilde{H} \neq H$, naively suggesting broken time-reversal symmetry:

$$\tilde{H} = THT^{-1} \quad (4.25)$$

$$= \sum_{i=1}^L \left[S_i^x S_{i+1}^x + S_i^y S_{i+1}^y + S_i^z S_{iT+1}^z - h_i S_i^z \right]. \quad (4.26)$$

Remark that $\tilde{H} \neq H$ does not imply that time-reversal symmetry is broken, although the opposite statement that there is time-reversal symmetry when $\tilde{H} = H$ holds. The Hamiltonian can be shown to be time-reversal invariant by setting $T_i = K$, such that the operators $S_i^{x,y,z}$ transform under time-reversal as

$$S_i^x \rightarrow S_i^x, \quad S_i^y \rightarrow -S_i^y, \quad S_i^z \rightarrow S_i^z. \quad (4.27)$$

Breaking time-reversal symmetry can be accomplished by adding a term H' to the original Hamiltonian such that $H \neq \tilde{H}$ for every choice of U_i . Ref. [73] proposes the

use of

$$H' = \sum_{i=1}^L \vec{S}_i \cdot (\vec{S}_{i+1} \times \vec{S}_{i+2}), \quad (4.28)$$

where $\vec{S}_i = (S_i^x, S_i^y, S_i^z)$. Note that H' preserves the conservation of the total spin S^z given in eq. (2.28), meaning that $[H', S^z] = 0$. In the work cited above, a term H' of this form is claimed to be experimentally relevant.

In this section, the focus is on the level statistics of the Hamiltonian $H + H'$ with H and H' given by respectively eqs. (4.13) and (4.28). The comparison with the eigenvalue statistics of the Gaussian beta ensemble is made by focusing on the distribution of the ratios of consecutive level spacings as defined in eq. (4.18). As pointed out in section 3.5.2, determining the distribution of the ratios of consecutive level spacings does not require unfolding, thus allowing for an unambiguous comparison.

As before, β is estimated from the average ratio $\langle r \rangle$ of consecutive level spacings given in eq. (4.17). The correspondence between β and $\langle r \rangle$ for the Gaussian beta ensemble with $\beta > 1$ is deduced from the Wigner-like surmise given in eq. (3.36). Explicitly, for a given value of β , the average ratio of consecutive level spacings for the Gaussian beta ensemble is approximated by

$$\langle r \rangle \approx \frac{1}{C_\beta} \int_0^1 \frac{(r + r^2)^{\beta+1}}{(1 + r + r^2)^{1+(3/2)\beta}} dr, \quad C_\beta = \int_0^1 \frac{(r + r^2)^\beta}{(1 + r + r^2)^{1+(3/2)\beta}} dr. \quad (4.29)$$

Fig. 4.8 shows $\langle r \rangle$ versus β for the Gaussian beta ensemble and the Wigner-like surmise, where the data of the former is obtained from table 4.1 presented before. One observes that the Wigner-like surmise gives a reasonable good estimate of $\langle r \rangle$ when $\beta \gtrsim 1$ is large enough. A more accurate correspondence could be obtained by extending table 4.1, which is not done here in view of the associated computational costs.

Fig. 4.9 shows the distribution $P(r)$ as defined in eq. (4.18) of the ratios of consecutive level spacings for the Hamiltonian $H + H'$. The procedure followed to obtain the data is identical to the one followed in section 4.5.3, except that here additionally the disorder strength $W = 3.9$ is studied aiming to study agreement for $\beta \approx 1$ and the estimation of β is obtained by using eq. (4.29). One can make a number of observations:

1. Good agreement between the level statistics of the physical model and the eigenvalue statistics of the Gaussian beta ensemble can be observed, which shows that the Gaussian beta ensemble can serve as a model for intermediate level statistics beyond $\beta \in [0, 1]$.
2. Because of the adding of H' to the original Hamiltonian, the crossover from the ergodic to the many-body localized phase shifts towards a higher disorder strength W . To the knowledge of the author, it has not been investigated if many-body localization can persist in settings with broken time-reversal symmetry.
3. It can be of interest to observe that a proper tuning of the disorder strength (here $W \approx 3.9$) makes that the level statistics of the Hamiltonian mimic those of an

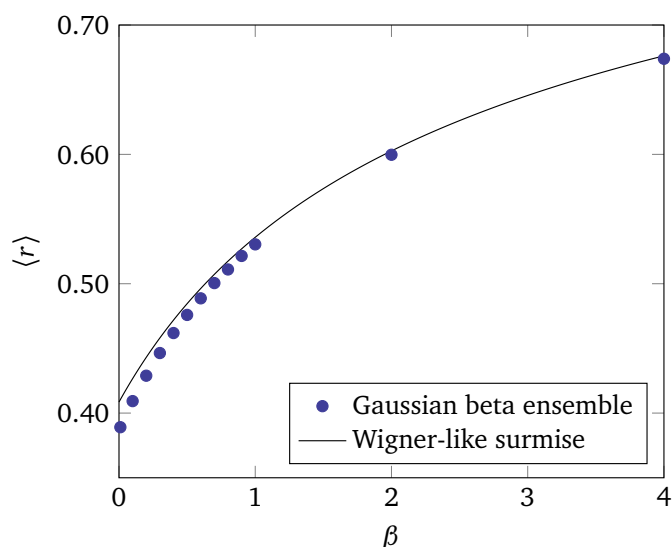


Fig. 4.8: The average ratio of consecutive level spacings for the Gaussian beta ensemble at several $\beta \in [0, 4]$ (dots) and the Wigner-like surmise (line) as given in eq. (4.29). Error bars are significantly smaller than the marker size. See the main text for computational details.

ergodic system with time-reversal symmetry (meaning that $\beta = 1$). There are no indications this disorder strength is special in some physical sense.

4.7 Longer-range statistics

The preceding sections indicated that the of level spacing distribution and the distribution of the ratios of consecutive level spacings for the ‘standard model of many-body localization’ match the corresponding eigenvalue statistics of the Gaussian beta ensemble for a properly chosen fitting parameter β . This section investigates to what extent a similar agreement can be observed for longer-range statistics, acting over a larger number of level spacings

The focus is on higher-order ratios of consecutive level spacings, first introduced by Tekur, Bhosale, and Santhanam in 2018 [74]. The k -th order ratios of consecutive level spacings generalize the ‘ordinary’ ratios of consecutive level spacings by only considering every k -th level. More precise, let $\{E_i\}_{i=1}^N$ ($E_1 \leq E_2 \leq \dots \leq E_N$) denote an ascendingly ordered set of energy levels. The set of k -th order ratios of consecutive level spacings contains the elements

$$r_i^{(k)} = \min\left(\frac{E_{i+2k} - E_{i+k}}{E_{i+k} - E_i}, \frac{E_{i+k} - E_i}{E_{i+2k} - E_{i+k}}\right), \quad i = 1, 2, \dots, N - 2k. \quad (4.30)$$

Notice that $r_i^{(1)}$ equals r_i as given in eq. (4.17). The motivation to consider higher-order ratios of consecutive level spacings instead of for example the spectral form

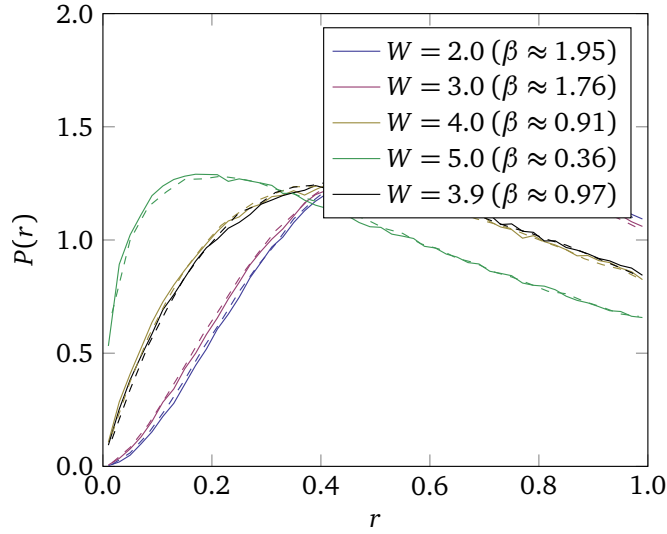


Fig. 4.9: The distribution of the ratios of consecutive level spacings for the Hamiltonian $H + H'$ as discussed in the main text at several W (solid lines), combined with corresponding distributions for the Gaussian beta ensemble (dashed lines). Solid and dashed lines obey the same color scheme. The estimated values of β are indicated in the legend.

factor is two-fold:

1. The (higher order) ratios of consecutive level spacings are insensitive to unfolding, as pointed out in section 3.5.2. As a result, the higher-order ratios of consecutive level spacings can be determined unambiguously.
2. Higher-order ratios of consecutive level spacings can be used as a tool to quantify the range over which the level statistics of the physical model and the Gaussian beta ensemble agree by varying k .

Higher-order level spacings can be defined in multiple ways, see for example ref. [53] for an alternative definition.

Analog to the procedure followed above, here the distribution of the higher-order ratios of consecutive level spacings is studied. For the ratios of higher-order spacings given above, the distribution is analog to eq. (4.18) for the ordinary ratios ($k = 1$) given by

$$P(r^{(k)}) = \frac{1}{N - 2k} \sum_{i=1}^{N-2k} \delta(r^{(k)} - r_i^{(k)}). \quad (4.31)$$

Also here, additional averaging over a large number of disorder realizations is performed. The distribution of higher-order ratios of consecutive spacings for the eigenvalues of the Gaussian beta ensemble is defined analogously. Figs. 4.10, 4.11, 4.12, and 4.13 show the distributions of $r^{(k)}$ for the ‘standard model of many-body localization’ and the corresponding distributions of the Gaussian beta ensemble for respectively

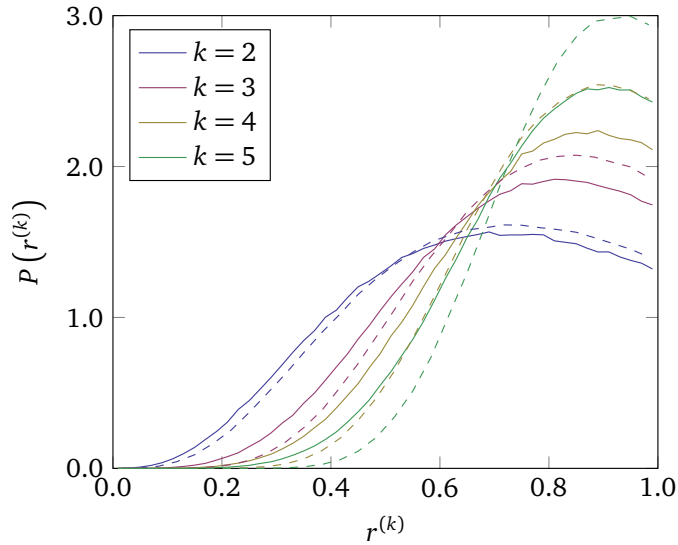


Fig. 4.10: The distribution of the ratios of consecutive level spacings of order $k = 2, 3, 4, 5$ for the physical model at $W = 2$ (solid lines) combined with corresponding distributions for the Gaussian beta ensemble (dashed lines) with $\beta \approx 0.86$ as estimated in section 4.5.3. Solid and dashed lines obey the same color scheme.

$W = 2, W = 3, W = 4,$ and $W = 5$ for $k \in \{2, 3, 4, 5\}$. The procedure followed to obtain the data is identical to the one followed in section 4.5.3. Three observations can be made:

1. In each of the figures, there is qualitative agreement up to and including $k = 3$, indicating that the level spacing statistics of the physical model and the eigenvalue statistics of the Gaussian beta ensemble match up to windows of ~ 6 level spacings.
2. There is a tendency for agreement to persist up to higher k with a lowering value of β . Apparently, weaker correlations (corresponding to lower β) tend to follow random matrix theory predictions on larger energy windows.
3. The eigenvalue statistics of the Gaussian beta ensemble systematically give a higher degree of level repulsion than the level statistics of the physical model. In other words: the energy levels of the physical model are correlated less strongly than the random matrix theory prediction. It can not be excluded that this is an artefact related to fluctuations in the density of states (see also fig. 4.6).

At this point, it can be of relevance to remark that a more extensive similar study on longer-range statistics yielding similar conclusions appearing after the work described in this chapter was published is provided in ref. [64].

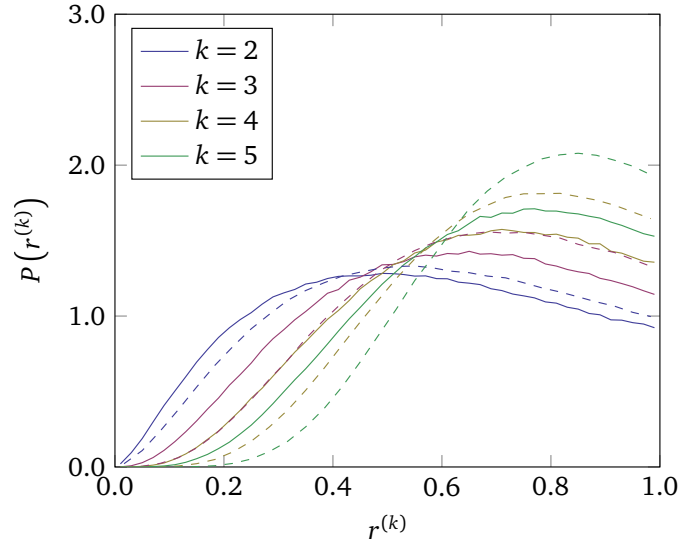


Fig. 4.11: The distribution of the ratios of consecutive level spacings of order $k = 2, 3, 4, 5$ for the physical model at $W = 3$ (solid lines) combined with corresponding distributions for the Gaussian beta ensemble (dashed lines) with $\beta \approx 0.23$ as estimated in section 4.5.3. Solid and dashed lines obey the same color scheme.

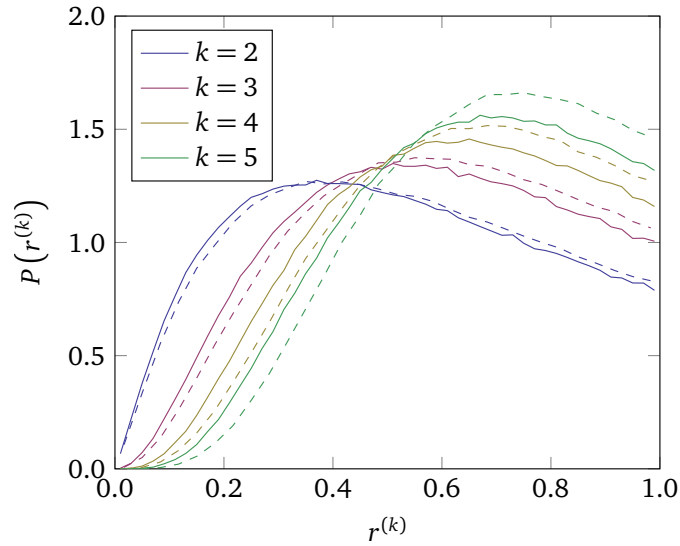


Fig. 4.12: The distribution of the ratios of consecutive level spacings of order $k = 2, 3, 4, 5$ for the physical model at $W = 4$ (solid lines) combined with corresponding distributions for the Gaussian beta ensemble (dashed lines) with $\beta \approx 0.05$ as estimated in section 4.5.3. Solid and dashed lines obey the same color scheme.

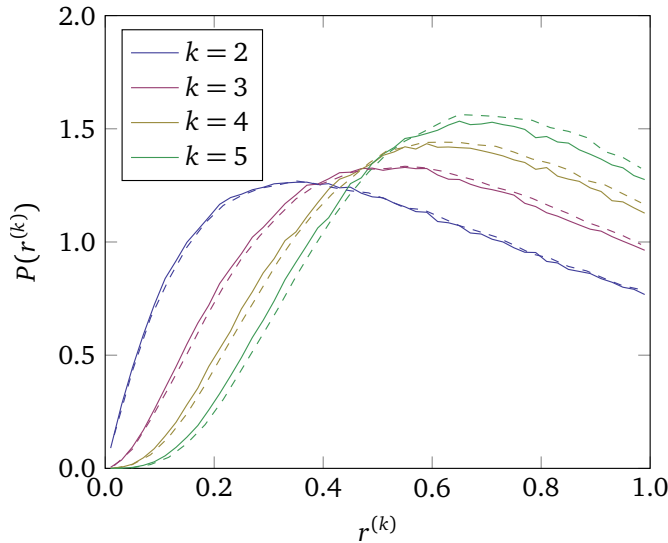


Fig. 4.13: The distribution of the ratios of consecutive level spacings of order $k = 2, 3, 4, 5$ for the physical model at $W = 5$ (solid lines) combined with corresponding distributions for the Gaussian beta ensemble (dashed lines) with $\beta \approx 0.02$ as estimated in section 4.5.3. Solid and dashed lines obey the same color scheme.

4.8 Discussion and outlook

In summary, this chapter proposed the eigenvalue statistics of the Gaussian beta ensemble as a random matrix model for the intermediate level statistics along the crossover from the ergodic to the many-body localized phase for the ‘standard model of many-body localization’. The Gaussian beta ensemble provides a generalization of Wigner-Dyson level statistics from the discrete taxonomy $\beta \in \{1, 2, 4\}$ to the continuous one $\beta \in (0, \infty)$, providing a smooth interpolation between Poissonian and Wigner-Dyson statistics.

Focusing on the level spacing distribution and the distribution of the ratios of consecutive level spacings, near-perfect agreement was observed between the eigenvalue statistics of the physical model and the corresponding statistics of the Gaussian beta ensemble over the full crossover range between the ergodic (corresponding to $\beta \approx 1$) and many-body localized (corresponding to $\beta \approx 0$) phase, where β is a single fitting parameter. Similar agreement is shown to hold for a related model with broken time-reversal symmetry.

Recently, a number of works focusing on spectral form factors (a probe not considered in this chapter) in the context of many-body localization appeared. Most notably, ref. [75] uses spectral form factors to argue that many-body localization can not persist in the thermodynamic limit (see also ref. [18] for a number of counter-arguments). Next, ref. [76] explores the spectral form factor for the ‘standard model of many-body localization’ along the crossover from the ergodic to the many-body localized phase. This probe is discussed in chapter 5.

A number of potentially interesting questions remain open for further investigations:

1. What is physical interpretation of the level statistics of the Gaussian beta ensemble for $\beta \notin \{1, 2, 4\}$? In particular, could one expect these level statistics to be found more generically in systems displaying intermediate level statistics?
2. The agreement between the level statistics of the physical model and the eigenvalue statistics of the Gaussian beta ensemble was shown to hold up to ~ 6 mean level spacings. Is this due to a physical mechanism due to which level repulsion is only short-ranged, or do fluctuations in the density of states play a role?

To the knowledge of the author, both questions are currently still open.

Spectral form factor and level repulsion

5.1 Introduction

Level statistics can be characterized by the spectral form factor, which is essentially given by the Fourier transformation of the two-point spectral correlation function. Typically, the spectral form factor is used as a probe for ergodicity by a comparison with the expectation for ergodic systems obtained using random matrix theory. The onset of ergodicity is quantified by the so-called Thouless time, which is given by the smallest time (wave number) from which onwards the two agree.

In this chapter, it is observed that the degree of level repulsion imposes a constraint on the time-integrated spectral form factor. It is discussed how this constraint could have a strong effect on the Thouless time. A new probe based on the spectral form factor, approximating the spectral self-correlation in a controlled way, is proposed. It is indicated how the spectral form factor can be integrated up to arbitrarily large times at low computational costs.

Section 2 discusses the spectral form factor. In section 3, the relation between the time-integrated spectral form factor and level repulsion is introduced. Section 4 reviews the Thouless time. In section 5, the new probe is proposed. Section 6 provides a numerical illustration for a system that can be tuned from an ergodic to a many-body localized phase. A discussion and outlook is provided in section 7.

5.2 Spectral form factor

Spectral form factors are studied primarily in the context of periodically driven systems, which are described by a time-dependent Hamiltonian $H(t)$ obeying the property

$$H(t + T) = H(t), \quad (5.1)$$

where T is the length of a single driving period. Periodically driven systems are commonly referred to as Floquet systems [77]. They are characterized by the Floquet

operator

$$U_F = \exp \left[-i \int_0^T H(t) dt \right], \quad (5.2)$$

which gives the time-evolution operator acting over a single driving period. Since U_F is unitary, the eigenvalues are parameterizable as $\exp(i\theta)$ with $0 \leq \theta < 2\pi$. The set of angles $\{\theta_i\}$ is known as the *quasi-energy spectrum*.

The quasi-energy spectrum is scaled to unit mean level spacing. Let $N = \dim(U_F)$ denote the number of levels in a spectrum. The elements of the scaled spectrum $\{x_i\}$ are obtained from the θ_i through the scaling $x_i = N/(2\pi) \theta_i$.

Let $\langle \cdot \rangle$ denote an ensemble average. The spectral density $\rho(x)$ and two-point spectral correlation function $\rho^{(2)}(x, x')$ for an ensemble of scaled quasi-energy spectra $\{x_i\}$ are given by

$$\rho(x) = \left\langle \sum_i \delta(x_i - x) \right\rangle, \quad (5.3)$$

$$\rho^{(2)}(x, x') = \left\langle \sum_{i \neq j} \delta(x_i - x) \delta(x_j - x') \right\rangle. \quad (5.4)$$

The focus is on the cluster function $\rho_c^{(2)}(x, x')$, representing the excess of the spectral density at x' due to the presence of a level at x (see for example ref. [24]). In terms of the spectral density and two-point spectral correlation function, the cluster function (equivalent to the connected part of the two-point spectral correlation function, hence the subscript c) is expressed as

$$\rho_c^{(2)}(x, x') = \rho^{(2)}(x, x') - \rho(x) \rho(x'). \quad (5.5)$$

The spectral form factor $K(t)$ (in the mathematical literature also known as the *structure function* [78]) is given by the Fourier transformation the cluster function,

$$K(t) = 1 + \frac{1}{\rho(0)} \int_0^N \left[\rho^{(2)}(0, x) - \rho(0) \rho(x) \right] e^{ixt} dx, \quad (5.6)$$

where $t \in 2\pi n/N$ with $n \in \mathbb{Z}$. The set of eigenvalues of the n -th power of U_F , which is the time-evolution operator for n cycles, is given by $\{\theta_i n\} = \{x_i t\}$. Since the parameter t only enters in the expression for the spectral form factor as θt , it follows that t has the interpretation of a (discrete) time.

Quasi-energy spectra generically have a uniform density of states, and obey the spectral symmetry $\rho^{(2)}(x, x') = \rho^{(2)}(x', x)$. The latter property implies that $K(t) = K(-t)$ and that $K(t)$ is real-valued. The spectral form factor for a quasi-energy spectrum scaled to

unit mean level spacing can be evaluated numerically as

$$K(t) = \frac{1}{N} \sum_{j,k} e^{i(x_j - x_k)t} - N \delta(t) \quad (5.7)$$

$$= \frac{1}{N} \left| \sum_j e^{ix_j t} \right|^2 - N \delta(t), \quad (5.8)$$

again for $t \in 2\pi n/N$ with $n \in \mathbb{Z}$ and all summed indices running over $1, 2, \dots, N$. The spectral form factor for an ensemble of quasi-energy spectra is given by the ensemble average of the spectral form factors for single spectra. As $K(t) = K(-t)$, the focus is typically restricted to $t \geq 0$.

The spectral form factor can be evaluated for the (unfolded) energy spectra of Hamiltonians as well [79]. The results discussed below are valid for both energy and quasi-energy spectra.

5.3 Constraint by level repulsion

A key distinction between ergodic and non-ergodic systems is the occurrence of level repulsion. Level repulsion is a characteristic property of Wigner-Dyson level spacing statistics, which is absent for Poissonian level spacing statistics (see section 3.5). It can be quantified by the self-correlation $\rho^{(2)}(x, x)$. For unfolded spectra (uniform density $\rho = 1$), one trivially finds

$$\rho^{(2)}(x, x) = \begin{cases} 0 & \text{(level repulsion),} \\ 1 & \text{(no level repulsion).} \end{cases} \quad (5.9)$$

The self-correlation puts a constraint on the time-integrated spectral form factor, as outlined below.

Aiming to express the self-correlation $\rho^{(2)}(0, 0)$ in terms of the spectral form factor as introduced in eq. (5.6), consider the time-integrated value of $1 - K(t)$ given by

$$\frac{2\pi}{N} \sum_{n \in \mathbb{Z}} \left[1 - K\left(\frac{2\pi n}{N}\right) \right]. \quad (5.10)$$

After substituting eq. (5.6) in (5.10), it follows by simple algebraic manipulations that the latter can be expressed as

$$\frac{2\pi}{N} \sum_{n \in \mathbb{Z}} \left[1 - K\left(\frac{2\pi n}{N}\right) \right] = \frac{2\pi}{N} \int_0^N \left(\sum_{n \in \mathbb{Z}} \left[1 - \rho^{(2)}(0, x) \right] e^{2\pi i n x / N} \right) dx \quad (5.11)$$

$$= 2\pi \left[1 - \rho^{(2)}(0, 0) \right]. \quad (5.12)$$

First, the summation and integration are reversed in order. Second, the Fourier transformation of $\delta(x)$ is recognized and evaluated. One observes that the integral of $1 - K(t)$ over t depends linearly on the spectral self-correlation.

5.4 Thouless time

When probing ergodicity using the spectral form factor, it is convenient to focus on the so-called Thouless time. Consider two levels θ_i and θ_j from a quasi-energy spectrum. The angle Δ between θ_i and θ_j is given by

$$\Delta = \min(|\theta_i - \theta_j|, 2\pi - |\theta_i - \theta_j|). \quad (5.13)$$

Note that $\Delta \in [0, \pi)$. When taking the n -th power of the Floquet operator to evolve the system over n cycles, the angle is given by $n\Delta$. Correlations can be measured as long as $n\Delta < 2\pi$, or equivalently when $n < 2\pi/\Delta$. Remark that correlations do not vanish for $n > 2\pi/\Delta$.

The (single) assumption underlying the Thouless time is that quasi-energy levels can be treated as uncorrelated for $n > 2\pi/\Delta$. Now, consider two ensembles of quasi-energy spectra with matching two-point correlations on angles $\Delta < \Delta_{\max}$. The difference between the two-point correlations due to mismatches on angles $\Delta > \Delta_{\max}$ can be detected if the system is evolved over $n < 2\pi/\Delta_{\max}$ cycles. Under the assumption mentioned above, two-point correlations are indistinguishable for $n > 2\pi/\Delta_{\max}$.

Quasi-energy spectra of ergodic systems obey the eigenvalue statistics of the corresponding circular random matrix ensemble, introduced in section 3.4. The angle Δ_{\max} on which the two-point correlations of the ensemble under consideration and the corresponding circular random matrix ensemble match can be referred to as the Thouless angle, named after an (in spirit) similar quantity encountered in the context of Anderson localization [80]. Focusing on quasi-energy spectra scaled to unit mean level spacing, one can define a Thouless energy x_{Th} and a Thouless time t_{Th} by

$$x_{\text{Th}} = \frac{N}{2\pi} \Delta_{\max}, \quad t_{\text{Th}} = \frac{2\pi}{N} \frac{2\pi}{\Delta_{\max}}, \quad (5.14)$$

where again N is the number of levels in a spectrum.

Ergodicity is conventionally quantified by the evolution of t_{Th} as a function of a control parameter such as the system size. The Thouless time is determined as the smallest time from which onwards the spectral form factor matches the value of the corresponding circular random matrix ensemble (see refs. [75, 76, 81–84] for a number of recent examples). When a system is ergodic, one expects $\Delta_{\max} = \pi$ and thus $t_{\text{Th}} \rightarrow 0$ for large N .

For the quasi-energy spectra scaled to unit mean level spacing of the circular orthogonal ensemble ($\beta = 1$) modeling Floquet operators of ergodic systems, one finds

$$K(t) = \begin{cases} \frac{|t|}{\pi} - \frac{|t|}{2\pi} \log\left(1 + \frac{|t|}{\pi}\right) & |t| \leq 2\pi, \\ 2 - \frac{|t|}{2\pi} \log\left(\frac{1 + |t|/\pi}{-1 + |t|/\pi}\right) & |t| > 2\pi. \end{cases} \quad (5.15)$$

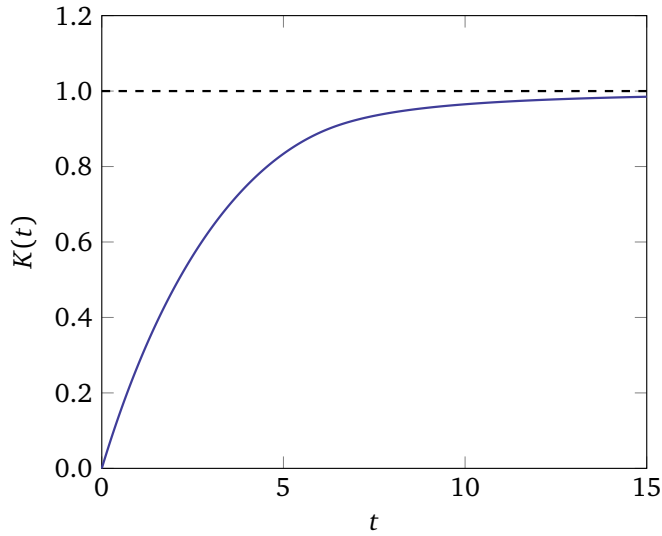


Fig. 5.1: The spectral form factor $K(t)$ for the circular orthogonal ensemble as given in eq. (5.15). The dotted line gives the corresponding value for quasi-energy spectra obeying Poissonian level spacing statistics.

Note that this expression is independent of N . Similar closed-form expressions can be found as well for the circular unitary ($\beta = 2$) and symplectic ($\beta = 4$) ensembles. Poissonian level spacing statistics are observed for uncorrelated levels. Trivially, it follows that then $\rho_c^{(2)}(x, x') = 0$ and thus $K(t) = 1$. Fig. 5.1 shows a plot of $K(t)$ as given in eq. (5.15).

5.5 Proposal for a new probe

The Thouless time is given by the smallest time from which onwards the spectral form factor matches the value for ergodic systems. Eq. (5.12) shows that the time-integrated value of the spectral form factor is determined by the presence or absence of level repulsion, quantified by the spectral self-correlation $\rho^{(2)}(0, 0)$. This could have a strong effect on the Thouless time:

1. If $\rho^{(2)}(0, 0) = 0$ as for ergodic systems, a positive (negative) difference between the spectral form factor and the expectation for ergodic systems at earlier times is corrected by a negative (positive) difference at later times.
2. If $\rho^{(2)}(0, 0) > 0$, the spectral form factor can not agree with the expectation for ergodic systems at all times.

This section aims to propose the spectral self-correlation as a new probe for ergodicity based on the spectral form factor. A quantity $\tilde{\rho}^{(2)}(0, 0|t_{\max})$ representing the spectral self-correlation as captured by the spectral form factor for times $t \leq t_{\max}$ is introduced below. This quantity approximates the spectral self-correlation $\rho^{(2)}(0, 0)$ in a controlled

way. It is shown that this quantity can be evaluated for arbitrarily large t_{\max} at low computational costs.

From eqs. (5.10) and (5.12), it follows that the spectral self-correlation $\rho^{(2)}(0, 0)$ is expressed in terms of the spectral form factor $K(t)$ as

$$\rho^{(2)}(0, 0) = 1 - \frac{1}{N} \sum_{n \in \mathbb{Z}} \left[1 - K\left(\frac{2\pi n}{N}\right) \right]. \quad (5.16)$$

For a quasi-energy spectrum $\{x_i\}$, the right-hand side of the this expression can be evaluated by inserting eq. (5.7), yielding

$$\left[\text{eq. (5.16)} \right] = 1 - \frac{1}{N} \sum_{n \in \mathbb{Z}} \left[1 - \frac{1}{N} \sum_{j, k} \exp\left(\frac{2\pi n i}{N}(x_j - x_k)\right) - N \delta(t) \right] \quad (5.17)$$

$$= 1 - \frac{1}{N^2} \sum_{n \in \mathbb{Z}} \left[\sum_{j \neq k} \exp\left(\frac{2\pi n i}{N}(x_j - x_k)\right) - N \delta(t) \right] \quad (5.18)$$

$$= 1 - \frac{2}{N^2} \sum_{n \in \mathbb{Z}} \left[\sum_{j > k} \cos\left(\frac{2\pi n i}{N}(x_j - x_k)\right) - N \delta(t) \right] \quad (5.19)$$

$$= 1 - \frac{4}{N^2} \sum_{n \in \mathbb{N}} \left[\sum_{j > k} \cos\left(\frac{2\pi n}{N}(x_j - x_k)\right) \right]. \quad (5.20)$$

Remark that up to now no approximations have been made.

Instead of summing over all $n \in \mathbb{N}$, an upper bound n_{\max} is imposed here. Let $t_{\max} = 2\pi n_{\max}/N$, and define

$$\tilde{\rho}^{(2)}(0, 0|t_{\max}) = 1 - \frac{4}{N^2} \sum_{n=1}^{n_{\max}} \left[\sum_{j > k} \cos\left(\frac{2\pi n}{N}(x_j - x_k)\right) \right] \quad (5.21)$$

$$= 1 - \frac{4}{N^2} \sum_{j > k} \left[\sum_{n=1}^{n_{\max}} \cos\left(\frac{2\pi n}{N}(x_j - x_k)\right) \right]. \quad (5.22)$$

The quantity $\tilde{\rho}^{(2)}(0, 0|t_{\max})$ gives the spectral self-correlation as captured by the spectral form factor for times $t \leq t_{\max}$, or equivalently by taking into account only Fourier modes with a period larger than $1/t_{\max}$ mean level spacing. It can be seen as a well-controlled approximation of the spectral self-correlation, becoming better with an increasing value of t_{\max} . Arguably, $\tilde{\rho}^{(2)}(0, 0|t_{\max})$ with $t_{\max} \gg 1$ provides a natural probe for ergodicity based on the spectral form factor.

The summation over n in eq. (5.22) can be evaluated by a single computation using the relation

$$\sum_{n=0}^{n_{\max}} \cos(nx) = \frac{1}{\sin(x/2)} \sin\left(\frac{1}{2}(n_{\max} + 1)x\right) \cos\left(\frac{x}{2}n_{\max}\right), \quad (5.23)$$

which gives

$$\begin{aligned} \left[\text{eq. (5.22)} \right] &= 1 - \frac{4}{N^2} \sum_{j>k} \left[\csc\left(\frac{\pi}{N}(x_j - x_k)\right) \right. \\ &\quad \times \sin\left(\frac{\pi}{N}(n_{\max} + 1)(x_j - x_k)\right) \\ &\quad \left. \times \cos\left(\frac{\pi n_{\max}}{N}(x_j - x_k)\right) \right], \end{aligned} \quad (5.24)$$

where $\csc(x) = 1/\sin(x)$. The evaluation of $\tilde{\rho}^{(2)}(0, 0|t_{\max})$ at arbitrarily large t_{\max} requires the computation of order N^2 sines and cosines, which corresponds to a computational cost comparable to the brute-force integration of the spectral form factor over times $t \lesssim 1$.

5.6 Numerical illustration

This section illustrates the use of $\tilde{\rho}^{(2)}(0, 0|t_{\max})$ as a probe for ergodicity with an example. The setup is a Floquet model introduced by Zhang, Khemani, and Huse in 2016 [85]. It describes a spin-1/2 chain subject to disorder and an external field switching back-and-forth between the two directions. The Floquet operator U_F is given by

$$U_F = e^{-i\tau H_x} e^{-i\tau H_z}, \quad (5.25)$$

where

$$H_x = 2 \sum_{j=1}^L g \Gamma S_j^x, \quad H_z = 4 \sum_{j=1}^{L-1} S_j^z S_{j+1}^z + 2 \sum_{j=1}^L \left(h + g \sqrt{1 - \Gamma^2} G_j \right) S_j^z. \quad (5.26)$$

The $S_j^{x,z}$ represent spin-1/2 operators as given in eq. (2.26), acting on site j only. The G_j represent disorder sampled independently from a Gaussian distribution with mean zero and unit variance. Aiming at consistency with previous works, the free parameters are taken as $g = 0.9045$, $h = 0.809$, and $\tau = 0.8$.

Finite-size scaling analysis indicates that the system is in a many-body localized (ergodic) phase for $\Gamma \lesssim 0.3$ ($\Gamma \gtrsim 0.3$) at large system sizes. Further evidence for a transition point at $\Gamma \approx 0.3$ is reported in ref. [86]. The model does not possess symmetries, such that for a system of L sites one finds $N = 2^L$. The spectral density $\rho(x)$ as introduced in eq. (5.3) is uniform. The theory of many-body localization in periodically driven systems is discussed in for example refs. [87–90].

The results of this section are obtained from statistics over at least 1.000 disorder realizations. Matrix diagonalizations and exponentiations are evaluated using respectively the `eig` and `expm` functions of MATLAB release 2017a [69] with the default options. The default random number generator is used to sample disorder.

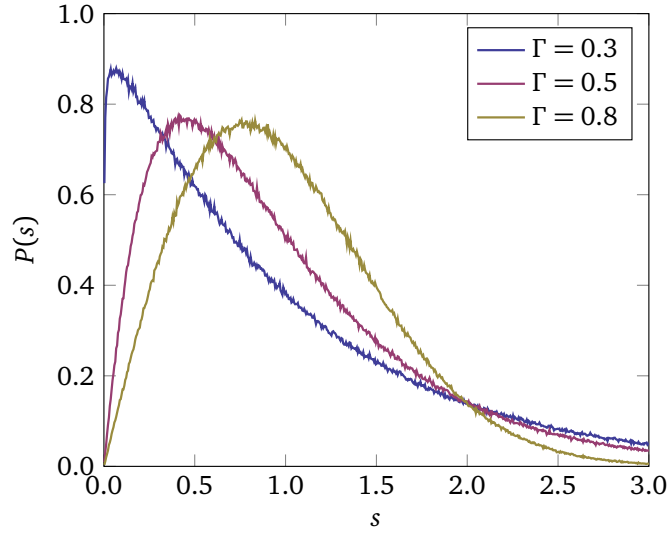


Fig. 5.2: The distributions of level spacings for the quasi-energy spectra of the physical model scaled to unit mean level spacing. Considered is system size $L = 12$. The noise is due to the finite number of disorder realizations that is studied.

Before presenting the main result, the level spacing distribution is investigated. The interpretation of the level spacing distribution as a probe for ergodicity is discussed in section 3.5. The elements of quasi-energy spectra $\{\theta_i\}$ are ordered ascendingly. Fig. 5.2 shows the distribution of level spacings

$$P(s) = \frac{1}{N} \sum_{i=1}^N \delta(s_i - s), \quad (5.27)$$

where

$$s_i = \frac{N}{2\pi} \min(|\theta_i - \theta_{i+1}|, 2\pi - |\theta_i - \theta_{i+1}|) \quad (5.28)$$

with $\theta_{i+N} \equiv \theta_i$, averaged over disorder realizations. The focus is on the largest considered system size $L = 12$ for several values of Γ . For $\Gamma = 0.8$, the curve is close to the random matrix theory prediction for orthogonal random matrix ensembles (see fig. 3.1 for reference). Intermediate statistics are observed for $\Gamma = 0.5$. For $\Gamma = 0.3$, the level spacing distribution is close to Poissonian. The figure suggests that here $P(0) > 0$, which would indicate that the spectral self-correlation is non-zero.

Next, the evolution of $\tilde{\rho}^{(2)}(0, 0|t_{\max})$ as a function of t_{\max} is investigated (see eq. (5.21)). Fig. 5.3 shows $\tilde{\rho}^{(2)}(0, 0|t_{\max})$ as a function of t_{\max} for the same parameter values as considered above. With decreasing Γ , the curve moves from the random matrix theory prediction for ergodic systems towards $\tilde{\rho}^{(2)}(0, 0|t_{\max}) = 1$ for integrable systems, which is consistent with the above observation for the level spacing distribution.

This chapter proposes $\tilde{\rho}^{(2)}(0, 0|t_{\max})$ evaluated at large t_{\max} as a probe for ergodicity. The main result presented in this section can be found in fig. 5.4, which shows $\tilde{\rho}^{(2)}(0, 0|t_{\max})$ evaluated at $t_{\max} = 1.000$ as a function of Γ for several system sizes.

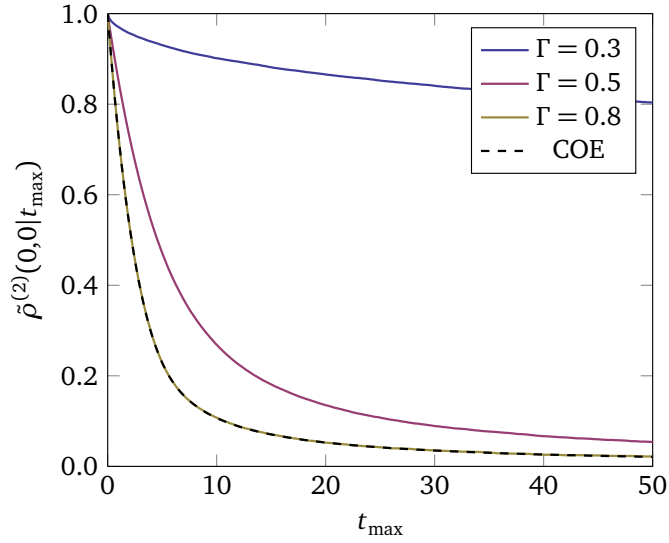


Fig. 5.3: Plots of $\tilde{\rho}^{(2)}(0,0|t_{\max})$ as a function of t_{\max} obtained from the same data as considered in fig. 5.2. The dashed line (COE) shows the random matrix theory prediction for the circular orthogonal ensemble for ergodic systems, as obtained from eq. (5.15).

For $\Gamma \leq 0.3$ the value increases with increasing system size, whereas it decreases with increasing system size for $\Gamma \geq 0.4$. This is in agreement with the results presented in refs. [85, 86] cited above.

5.7 Discussion and outlook

In summary, this chapter revisits the interpretation of the spectral form factor as a diagnostic for ergodicity. It is shown that the presence or absence of level repulsion imposes a constraint on the time-integrated spectral form factor. This constraint is argued to potentially have a strong effect on the Thouless time, which is the conventional quantity by which ergodicity is diagnosed. A new probe based on the spectral form factor, approximating the spectral self-correlation in a controlled way, is proposed.

The use of the probe is demonstrated for a Floquet system that can be tuned from an ergodic to a many-body localized phase. The results are in agreement with the previous literature. In future studies, it could be interesting to compare the here proposed probe to other probes, such as the average ratio of consecutive level spacings (see section 3.5.2). For completeness, the average ratio of consecutive level spacings

$$\langle r \rangle = \frac{1}{N} \sum_{i=1}^N \min \left(\frac{s_{i+1}}{s_i}, \frac{s_i}{s_{i+1}} \right) \quad (5.29)$$

with s_i as defined in eq. (5.28) and additionally averaged over disorder realizations for the parameters considered in fig. 5.4 is shown in fig. 5.5.

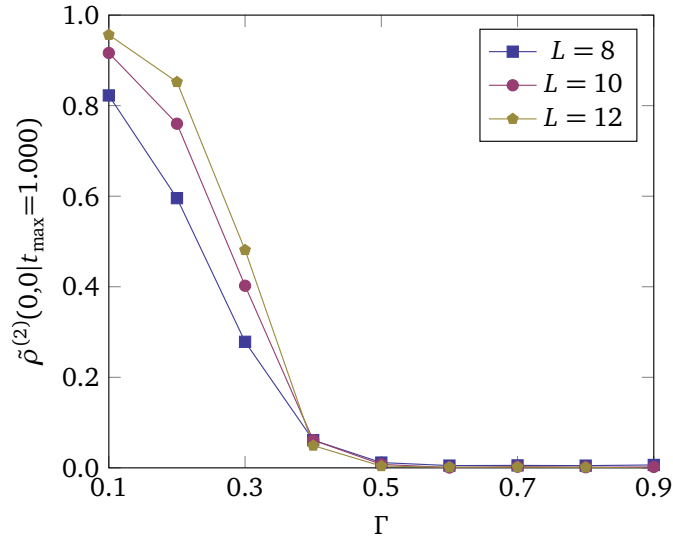


Fig. 5.4: Plots of $\tilde{\rho}^{(2)}(0,0|t_{\max} = 1.000)$ for the physical model as a function of Γ for system sizes $L = 8, 10, 12$. For ergodic and non-ergodic systems, one finds respectively $\tilde{\rho}^{(2)}(0,0|t_{\max} = 1.000) \approx 0.001$ and $\tilde{\rho}^{(2)}(0,0|t_{\max} = 1.000) = 1$.

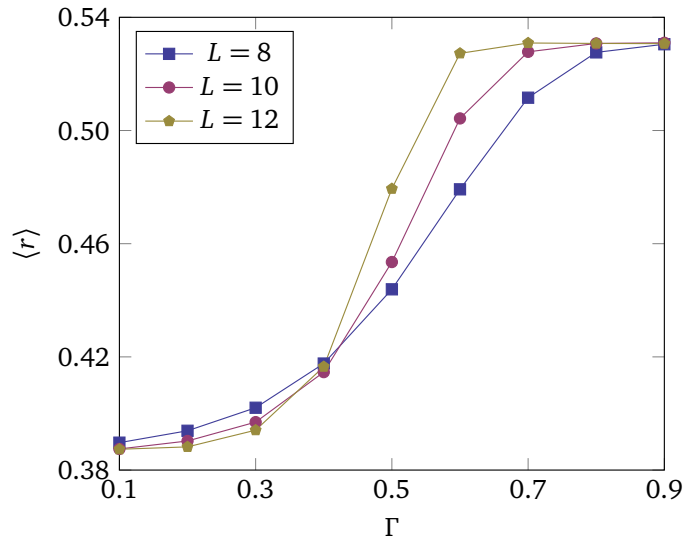


Fig. 5.5: The average ratio of consecutive level spacings $\langle r \rangle$ for the physical model as a function of Γ for system sizes $L = 8, 10, 12$. For ergodic and non-ergodic systems, one finds respectively $\langle r \rangle \approx 0.531$ and $\langle r \rangle \approx 0.386$.

Many-body localization in the Fock space of natural orbitals

6.1 Introduction

Natural orbitals and the corresponding occupation numbers resulting from the diagonalization of a one-particle density matrix gained significant attention in the field of many-body localization [91–95]. It was found that the occupation numbers exhibit qualitatively different statistics in the ergodic and the many-body localized phase, allowing them to be used as a probe for the many-body localization transition [91]. Based on this observation, this chapter argues that the scope can be naturally broadened by studying many-body localization in the Fock basis constructed out of the natural orbitals. The results presented in this chapter are published in ref. [1].

The ergodic phase in the vicinity of the many-body localization transition displays properties that are typically associated with non-ergodic systems [96, 97], such as subdiffusion [98, 99] and subthermal entanglement scaling [100]. By numerically studying the participation ratio for the eigenstates of the Hamiltonian for a finite-size system, a crossover between different phases at a disorder strength close to the disorder strength at which the breakdown of thermalization [101] sets in, is identified.

Section 2 introduces one-particle density matrices and discusses their role in the field of many-body localization. Section 3 points out the motivation for the current investigation by discussing the Fock space constructed out of the natural orbitals. In section 4, a probe to quantify localization of quantum states in Fock space is proposed. The model that is considered and the numerical implementation are discussed in sections 5 and 6, respectively. The results are presented in section 7. Section 8 provides a discussion and outlook.

6.2 One-particle density matrices

In this chapter, a study on many-body localization in the Fock space constructed out of natural orbitals is described. As discussed below, this study can be regarded as a

continuation of a series of earlier works on spectra of one-particle density matrices. This section introduces one-particle density matrices, followed by a discussion of their relation to many-body localization. A review of the content discussed in this section can be found in for example section 5 of ref. [93].

Consider a system of spinless fermions, which are created (annihilated) by the operators c_i^\dagger (c_i) with i denoting a labeling index. Recapitulating, these operators obey the anticommutation relations given in eqs. (2.2) and (2.3) by

$$\{c_i^\dagger, c_j\} = \delta_{ij}, \quad (6.1)$$

$$\{c_i^\dagger, c_j^\dagger\} = \{c_i, c_j\} = 0. \quad (6.2)$$

In the present context, the use of one-particle density matrices was introduced by Löwdin in 1955 [16]. The one-particle density matrix associated with a state $|\psi\rangle$ is element-wise defined as

$$\rho_{ij}^{(1)} = \langle\psi|c_i^\dagger c_j|\psi\rangle. \quad (6.3)$$

Note that $\rho^{(1)}$ is symmetric by the anticommutation relations given in eq. (6.1). A generalization to multi-particle density matrices is discussed in the work cited above.

In what follows, the focus is restricted to systems for which the number of particles N in the system given by

$$N = \sum_i c_i^\dagger c_i \quad (6.4)$$

is fixed (conserved). This number can be determined from the trace of the one-particle density matrix by

$$\text{Tr}(\rho^{(1)}) = \sum_i \langle\psi|c_i^\dagger c_i|\psi\rangle \quad (6.5)$$

$$= N, \quad (6.6)$$

where the step from eq. (6.5) to (6.6) is made by substituting eq. (6.4). Because $\langle\psi|c_i^\dagger c_i|\psi\rangle \in [0, 1]$, the eigenvalues of one-particle density matrices are real-valued numbers ranging from 0 to 1.

The eigenvalue spectra of one-particle density matrices can be used to distinguish between interacting and (effectively) non-interacting systems. If a system is non-interacting, the diagonalized Hamiltonian H and the corresponding one-particle density matrix are of the respective forms

$$H = \sum_i \epsilon_i d_i^\dagger d_i, \quad \rho_{ij}^{(1)} = \langle\psi|d_i^\dagger d_j|\psi\rangle. \quad (6.7)$$

Here, d_i^\dagger (d_i) denote creation (annihilation) operators of spinless fermions obeying the anticommutation relations

$$\{d_i^\dagger, d_j\} = \delta_{ij}, \quad (6.8)$$

$$\{d_i^\dagger, d_j^\dagger\} = \{d_i, d_j\} = 0. \quad (6.9)$$

The state under consideration is denoted by $|\psi\rangle$, and the ϵ_i denote the excitation energies of the single-particle ($N = 1$) eigenstates. If $|\psi\rangle$ is an eigenstate of the system, the one-particle density matrix as given in eq. (6.7) is diagonal with elements 1 and 0 on the diagonal. For ergodic states, one-particle density matrices have eigenvalues that are all approximately equal [91].

As discussed in section 2.3, many-body localization can be interpreted as an emergent type of Anderson localization in Fock space, meaning that many-body localized systems are similar to non-interacting ones when considering one-particle density matrices. It was shown first by Bera, Schomerus, Heidrich-Meisner, and Bardarson in 2015 [91] that the eigenvalue statistics of one-particle density matrices can be used to probe many-body localization.

Consider a L -site system with N particles, and let n_i ($i = 1, 2, \dots, L$) denote the eigenvalues of the one-particle density matrix associated with an eigenstate of the Hamiltonian. Suppose that the n_i are labeled in descending order,

$$n_1 \geq n_2 \geq \dots \geq n_L. \quad (6.10)$$

The n_i are referred to as *occupation numbers of natural orbitals*, the latter being discussed in the next section. If the system is non-interacting, the first N occupation numbers have a value 1 while the remaining $L - N$ ones have a value 0. Among a number of other quantities, the reference cited above studies the *occupation gap*

$$\Delta n = n_N - n_{N+1}, \quad (6.11)$$

which follows to be given by $\Delta n = 1$ for non-interacting systems. It is indicated that the occupation gap can be used to detect many-body localization; it is given by a number close to 1 and 0 in respectively the many-body localized and ergodic phase. Fig. 6.1 illustrates the above for (representative) eigenstates of a non-interacting and a many-body localized system.

In the context of many-body localization, a number of studies on one-particle density matrices have been undertaken. The list below gives a non-exhaustive list of results.

1. Ref. [94] focuses on the dynamics of occupation numbers. The setting is a one-dimensional system in a many-body localized phase with spinless fermions initially located on every even site, meaning that the system is initialized in a Néel state. It is shown that at late times the occupation gap remains non-zero, which is interpreted as a consequence of the local structure of the initial state and the resulting partial occupation of so-called quasiparticles roughly equivalent to the local integrals of motion discussed in section 2.4.
2. Ref. [95] studies the natural orbitals (eigenstates) of one-particle density matrices obtained from many-body localized Hamiltonian eigenstates. It is observed that the natural orbitals are spatially localized. Next, it is found that different Hamiltonian eigenstates corresponding to nearby energy levels share an approximately common set of natural orbitals.

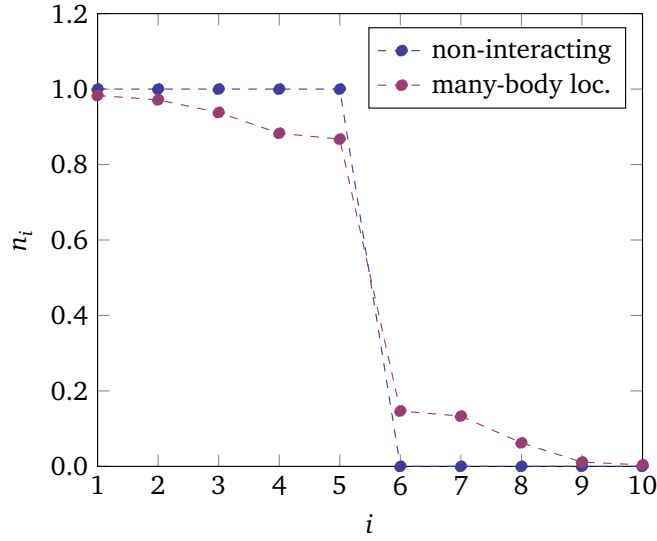


Fig. 6.1: The occupation numbers n_i for (representative) eigenstates of a non-interacting and a many-body localized system of size $L = 10$ at half-filling ($N = 5$). The occupation gaps are given by $\Delta n = 1$ and $\Delta n \approx 0.72$ for the non-interacting and the many-body localized eigenstate, respectively. The connecting lines serve as a guide to the eye.

3. Ref. [102] proposes an experimental setup able to measure the occupation numbers of one-particle density matrices for systems of ultracold atoms in optical lattices. To the knowledge of the author, no experimental follow-up study has been performed currently.

6.3 Fock space of natural orbitals

Consider a system of non-interacting spinless fermions created (annihilated) by the operators c_i^\dagger (c_i), which obey the anticommutation relations given in eqs. (6.1) and (6.2). The particle number N given in eq. (6.4) is conserved. Because the system is non-interacting, eigenstates of the Hamiltonian are given by Slater determinants constructed out of single-particle eigenstates, as discussed in section 2.3.

The single-particle eigenstates of the Hamiltonian can be read off from the eigen-decomposition. In the diagonal representation, the Hamiltonian H and one-particle density matrix $\rho^{(1)}$ of a non-interacting system are given in eq. (6.7) by

$$H = \sum_i \epsilon_i d_i^\dagger d_i, \quad \rho_{ij}^{(1)} = \langle \psi | d_i^\dagger d_j | \psi \rangle, \quad (6.12)$$

where $|\psi\rangle$ gives the state under consideration, and the ϵ_i denote the excitation energies of the single-particle ($N = 1$) eigenstates. The operators d_i^\dagger , d_i obey the anticommutation relations for spinless fermions given in eqs. (6.8) and (6.9). For eigenstates of the

Hamiltonian, two statements hold:

1. Both the Hamiltonian and the one-particle density matrix are of diagonal form. This implies that the single-particle ($N = 1$) eigenstates of the Hamiltonian are identical to the eigenstates of the one-particle density matrix.
2. The one-particle density matrix is diagonal for *each* of the eigenstates of the Hamiltonian. This implies that the set of eigenstates of the one-particle density matrix is the same for each eigenstate of the Hamiltonian. Eigenstates of the one-particle density matrices are commonly referred to as *natural orbitals* [16].

The eigenstates of the Hamiltonian span what is referred to as the *Fock space constructed out of the natural orbitals*.

Diagonalizing the one-particle density matrix associated with an eigenstate $|\psi\rangle$ gives the natural orbitals $|\phi_i\rangle$ and the associated occupation numbers n_i , the latter satisfying $n_i \in \{0, 1\}$ because the system is non-interacting:

$$\rho^{(1)}|\phi_i\rangle = n_i|\phi_i\rangle. \quad (6.13)$$

The natural orbitals are said to be either *occupied* (occupation number $n_i = 1$) or *unoccupied* (occupation number $n_i = 0$). Remark that, because of the degeneracy of the eigenvalues, the natural orbitals are not defined uniquely in this way. This issue does not occur in the next sections, where interactions break the degeneracies of the eigenvalues of one-particle density matrices.

6.4 Localization in Fock space

This section proposes a probe to quantify localization of quantum states in Fock space. Consider Hamiltonians of the form $H = H_0 + H_{\text{int}}$ with the successive terms as given in eqs. (2.10) and (2.11) by respectively

$$H_0 = \sum_i \epsilon_i c_i^\dagger c_i, \quad (6.14)$$

$$H_{\text{int}} = \sum_{ij} J_{ij}^{(1)} c_i^\dagger c_j + \sum_{ijkl} J_{ijkl}^{(2)} c_i^\dagger c_j^\dagger c_k c_l + \dots \quad (6.15)$$

Here, the creation (annihilation) operators c_i^\dagger (c_i) with i denoting a labeling index obey the anticommutation relations for spinless fermions given in eqs. (6.1) and (6.2). The first and second term represent respectively the diagonal and the off-diagonal part of the Hamiltonian, meaning that $J^{(n)} = 0$ if the first and last n indices are identical.

In the language of perturbation theory, the non-diagonal part is said to induce hybridizations between basis states. This leads to a hierarchical structure in the set of basis states, which is explored in the context of many-body localization below.

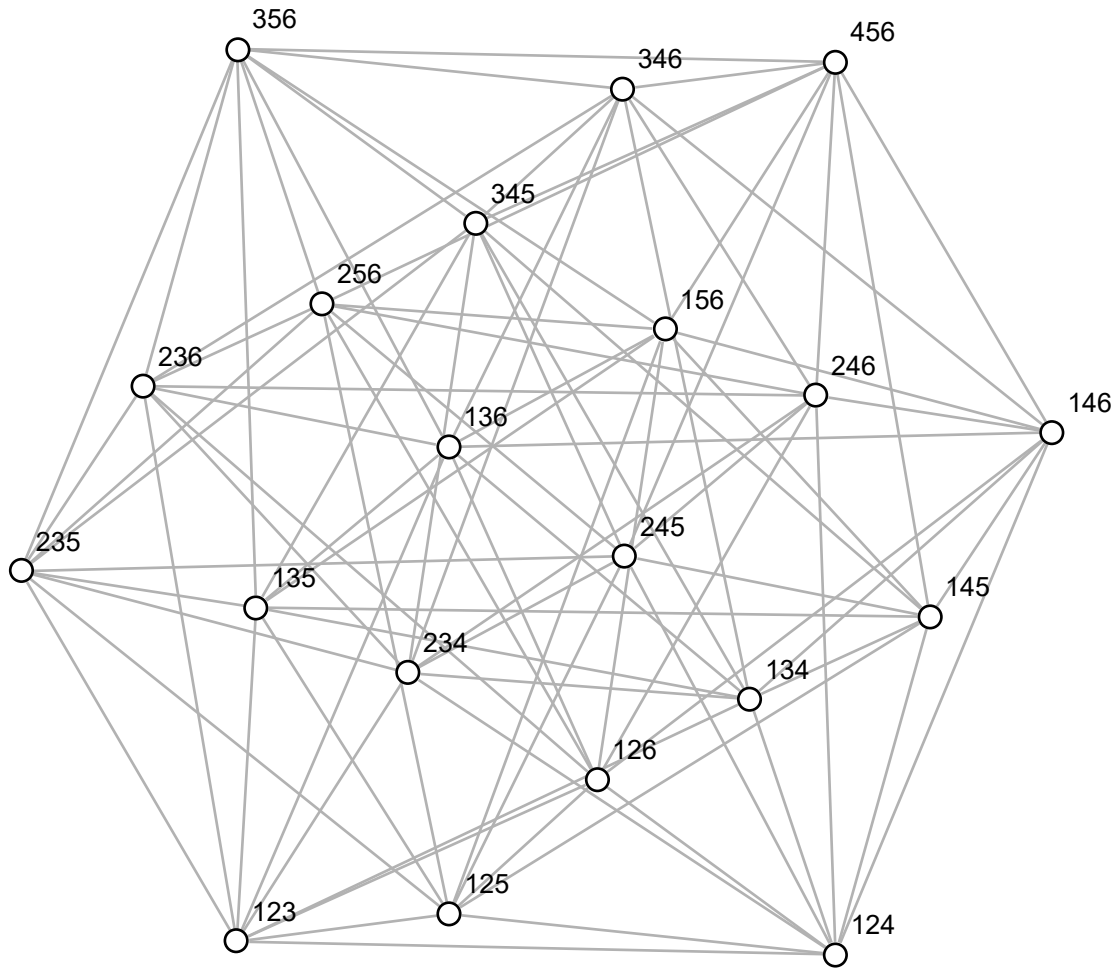


Fig. 6.2: A graph with vertices representing the basis states of a non-interacting system of spinless fermions with 6 sites labeled by $\{1, 2, 3, 4, 5, 6\}$ at half-filling. The labels denote the indices of the occupied natural orbitals. The edges connect basis states that are hybridized by a two-body interaction. The positioning of the vertices is arbitrary.

Aiming to introduce the main idea, focus on the example of 3 fermions on 6 sites. Let the sites be labeled by indices $\{1, 2, \dots, 6\}$. For two-body interactions, one can draw a graph consisting of vertices representing the basis states and edges connecting basis states that can be hybridized by a two-body interaction. Fig. 6.2 shows such a graph. A hierarchy arises: from a given basis state, each other one can be reached in either 1, 2, or 3 hybridization steps (in the current context referred to as *particle-hole excitations*).

Let $|\psi^{(0)}\rangle$ denote an eigenstate of H_0 . The remaining basis states can be labeled

according to the number of particle-hole excitations with respect to this reference state:

$$\{|\psi_i^{(1)}\rangle\} \quad 1 \text{ particle-hole excitation,} \quad (6.16)$$

$$\{|\psi_i^{(2)}\rangle\} \quad 2 \text{ particle-hole excitations,} \quad (6.17)$$

$$\{|\psi_i^{(3)}\rangle\} \quad 3 \text{ particle-hole excitations,} \quad (6.18)$$

et cetera. For a system of N particles on L sites, the number of ways to create k particle-hole excitations is

$$\dim(\{|\psi_i^{(k)}\rangle\}) = \binom{N}{k} \times \binom{L-N}{k}, \quad (6.19)$$

where the first term gives the number of ways to take k out of N occupied natural orbitals, and the second term gives the number of ways to take k out of $L-N$ unoccupied natural orbitals.

The labeling system proposed above allows one to distinguish localized from delocalized states, and to characterize crossovers from localized to delocalized (ergodic) phases. Let $P^{(k)}$ denote the overlap of a state $|\psi\rangle$ with basis states having k particle-hole excitations with respect to the reference state $|\psi^{(0)}\rangle$,

$$P^{(k)} = \sum_i |\langle\psi_i^{(k)}|\psi\rangle|^2. \quad (6.20)$$

For a properly chosen reference state $|\psi^{(0)}\rangle$, one finds $P^{(0)} = 1$ if the state is fully localized. For an ergodic state, one finds

$$P^{(k)} \approx \frac{1}{\dim(H)} \dim(\{|\psi_i^{(k)}\rangle\}). \quad (6.21)$$

For the example of 3 particles on 6 sites discussed above, ergodic states obey $P^{(0)} \approx 0.05$, $P^{(1)} \approx 0.45$, $P^{(2)} \approx 0.45$, and $P^{(3)} \approx 0.05$. Notice that the $P^{(k)}$ sum up to 1.

The building blocks of Fock bases are the single-particle states. For non-interacting systems, these are naturally given by the natural orbitals. For interacting systems, several arguably natural choices of single-particle states could be adapted. Below, the single-particle states are taken as the eigenstates (natural orbitals) of the one-particle density matrix $\rho^{(1)}$ as given in eq. (6.3). The reference state $|\psi^{(0)}\rangle$ is constructed from the N highest occupied natural orbitals. Two remarks can be made:

1. Constructing the Fock space out of the natural orbitals establishes a relation with previous studies on the evolution of occupation spectra along crossovers from ergodic to many-body localized phases (see for example refs. [94, 95, 102] as discussed in the former section).
2. For the Hamiltonian of an interacting system, the eigenstates do not have a common set of natural orbitals. Consequently, superpositions of eigenstates can not be naturally studied in the Fock space constructed out of the natural orbitals.

As suggestion for a different choice of the single-particle states is mentioned in the discussion section below.

6.5 Model and parameters

This chapter studies the onset of localization along a crossover from an ergodic to a many-body localized phase. As before, the focus is on the ‘standard model of many-body localization’ discussed in section 2.6. The model describes a collection of interacting spin-1/2 particles. First, the model is reformulated as a collection of interacting spinless fermions.

In section 2.6, the Hamiltonian of the model is written down in terms of the spin-1/2 operators S_i^x , S_i^y , and S_i^z introduced in eq. (2.26). The spin operators S_j^x and S_j^y can be rewritten in terms of the so-called raising and lowering ladder operators S_j^+ and S_j^- as

$$S_j^x = \frac{1}{2} (S_j^+ + S_j^-), \quad S_j^y = \frac{1}{2i} (S_j^+ - S_j^-). \quad (6.22)$$

Note that direct expressions for S_j^+ and S_j^- can be obtained in a straightforward way. In terms of the S_j^z and the ladder operators given above, the Hamiltonian H describing the model is expressed as

$$H = \sum_{i=1}^L \left[S_i^+ S_{i+1}^- + S_i^- S_{i+1}^+ + S_i^z S_{i+1}^z + h_i S_i^z \right]. \quad (6.23)$$

Again, periodic boundary conditions $S_{L+1}^{+, -, z} \equiv S_1^{+, -, z}$ are imposed. The Hamiltonian can be rewritten in terms of the fermionic creation (annihilation) operators c_i^\dagger (c_i) obeying the anticommutation relations given in eqs. (6.1) and (6.2) by a Jordan-Wigner transformation. To do this, let

$$S_i^+ = \frac{1}{2} c_i^\dagger \prod_{j=1}^{i-1} S_j^z, \quad S_i^- = \frac{1}{2} c_i \prod_{j=1}^{i-1} S_j^z, \quad S_i^z = \frac{1}{2} (1 - 2 c_i^\dagger c_i). \quad (6.24)$$

One can show that these definitions obey the correct commutation relations. Substituting the above expressions in eq. (6.23), one finds the (up to a constant offset) equivalent expression

$$H = \frac{1}{2} \sum_{i=1}^L (c_i^\dagger c_{i+1} + c_i c_{i+1}^\dagger) + \sum_{i=1}^L h_i \left(n_i - \frac{1}{2} \right) + \sum_{i=1}^L \left(n_i - \frac{1}{2} \right) \left(n_{i+1} - \frac{1}{2} \right), \quad (6.25)$$

where $n_i = c_i^\dagger c_i$ is the number of particles on site i .

The Hamiltonian as formulated in eq. (6.23) commutes with the total spin S^z as introduced in eq. (2.28). Applying the Jordan-Wigner transformation on the total spin

operator, one finds

$$S^z \rightarrow \frac{L}{2} - \sum_{i=1}^L c_i^\dagger c_i \quad (6.26)$$

$$= \frac{L}{2} - N, \quad (6.27)$$

where N is (for obvious reasons) referred to as the particle number. As before, the focus is restricted to the $S^z = 0$, or equivalent $N = L/2$ half-filling sector. The onsite potentials h_i ($i = 1, 2, \dots, L$) are again sampled independently from the probability distribution

$$P(x) = \begin{cases} 1/(2W) & \text{if } |x| \leq W, \\ 0 & \text{if } |x| > W \end{cases} \quad (6.28)$$

as given in eq. (4.14), corresponding to the uniform distribution ranging over the interval $[-W, W]$. As outlined in section 2.6, the disorder strength W can be used as a tuning parameter able to drive the system from an ergodic ($W \lesssim 3.6$) to a many-body localized ($W \gtrsim 3.6$) phase. Remark that for $1.7 \lesssim W \lesssim 3.6$ a number of non-trivial effects can be observed, as discussed in section 8 of this chapter.

In the numerical investigation discussed below, the focus is restricted to the eigenstate for which the associated energy is closest to 0. Averages are taken over 1000 disorder realizations. The motivation only to consider a single eigenstate per disorder realization is that different eigenstates might have strongly resembling single-particle states, as suggested by ref. [95] discussed above. System sizes, limited by computational costs, range from $L = 10$ to $L = 16$.

6.6 Numerical implementation

The study discussed in this chapter is about the expansion of many-body states in the Fock space constructed out of the natural orbitals. The states under consideration are given by eigenstates of Hamiltonians. The eigenstates are obtained numerically by a procedure similar to the one discussed in section 4.5.2. For all computations, again the computational software MATLAB, release 2017a [69] is used.

At a technical level, the following steps are involved to expand a given state $|\psi\rangle$ in the Fock basis constructed out of the natural orbitals:

1. The one-particle density matrix $\rho^{(1)}$ as given in eq. (6.3) is constructed element-wise. Exact diagonalization (see section B.3 in appendix B for details of the algorithm) is used to obtain the occupation numbers n_i and corresponding natural orbitals $|\phi_i\rangle$ given by respectively the eigenvalues and corresponding eigenvectors. Matrix diagonalizations are performed using the `eig` function (default options).

2. A table of all possible selections of N distinct indexing labels $i \in \{1, 2, \dots, L\}$ is generated. Each selection $\{i_1, i_2, \dots, i_N\}$ labels a basis state of the Fock space by the indices of the occupied natural orbitals. For each selection, the number k of particle-hole excitations with respect to the reference state with indices $\{1, 2, \dots, N\}$ is calculated as the cardinality

$$k = |\{i_1, i_2, \dots, i_N\} \cup \{1, 2, \dots, N\}|. \quad (6.29)$$

The number of particle-hole excitations is involved in the determination of $P^{(k)}$ as given in eq. (6.20).

3. For each selection $\{i_1, i_2, \dots, i_N\}$ of natural orbitals, the associated basis state of the Fock space is expanded in the computational basis. The overlap with the computational basis state with particles localized on sites $\{j_1, j_2, \dots, j_N\}$ is given by the Slater determinant

$$\det \begin{pmatrix} \phi_{i_1}(j_1) & \phi_{i_1}(j_2) & \cdots & \phi_{i_1}(j_N) \\ \phi_{i_2}(j_1) & \phi_{i_2}(j_2) & \cdots & \phi_{i_2}(j_N) \\ \vdots & \vdots & \ddots & \vdots \\ \phi_{i_N}(j_1) & \phi_{i_N}(j_2) & \cdots & \phi_{i_N}(j_N) \end{pmatrix}, \quad (6.30)$$

where $\phi_i(j)$ is the j -th component of $|\phi_i\rangle$ (see for example ref. [16]). The numerical algorithm used to compute determinants is outlined in section 4 of appendix B.

4. The overlap of a basis state from the Fock basis with $|\psi\rangle$ is determined by summing over all basis states.

Remark that the number of particle-hole excitations for a basis state of the Fock space does not need to be determined separately for each $|\psi\rangle$.

6.7 Probing crossovers

Localization in Hilbert space can be studied through a number of different probes, such as the inverse participation ratio [103, 104] or the Shannon-Rényi entropies [105]. This section shows the numerical results obtained by focusing on the weights $P^{(k)}$ as introduced in eq. (6.20), and the participation ratio (see for example ref. [106]). Surprisingly, no signatures of the many-body localization transition at disorder strength $W \approx 3.6$ [27] are observed. Instead, a crossover between different phases at the ergodic side centered at $W \approx 2.3$ is reported.

As the focus is on the effect of considering a non-standard basis, only basis-dependent probes are considered. This excludes probes based on, for example, level statistics [2, 60] or entanglement [3, 100, 107–109]. Since superpositions of eigenstates can not be naturally studied in the Fock space constructed out of the natural orbitals, also dynamical probes as investigated in for example refs. [110–112] are excluded.

6.7.1 Weight decomposition

Consider the weights $P^{(k)}$ as introduced in eq. (6.20). Recapitulating, $P^{(k)}$ gives the overlap of the state under consideration with basis states of the Fock space having k particle-hole excitations with respect to the reference state. Let $\langle \cdot \rangle$ denote an ensemble average. Fig. 6.3 shows the ensemble average $\langle P^{(k)} \rangle$ for $k = 1, 2, \dots, 5$ as a function of the disorder strength W for systems of size $L = 14$ and $L = 16$. One can make three observations:

1. Many-body localized eigenstates are observed to be well localized in the Fock space. On average, eigenstates are mainly composed out of basis states with low values of k , which is consistent with the interpretation of many-body localization as localization in the Fock space (see section 2.3 and ref.[6]).
2. No clear signatures can be observed of the many-body localization transition at $W \approx 3.6$. However, on average eigenstates appear to remain localized until significantly lower disorder strengths.
3. At a qualitative level, similar observations can be made for both system sizes.

These observations point in a similar direction as the findings reported by Luitz and Bar Lev in 2016 [113] on ergodic properties of eigenstates from the point of the Berry conjecture [114], indicating a violation at a disorder strength as low as $W = 1.6$. At a qualitative level, the Berry conjecture states that the eigenstates of thermal systems are spread out over the full Hilbert space in any local basis.

6.7.2 Participation ratio

Inspired by works on Anderson localization, the participation ratio has been investigated in the context of many-body localization by De Luca and Scardicchio in 2013 [106], and earlier as part of a broader oriented study by Canovi, Rossini, Fazio, Santoro, and Silva in 2011 [115]. In ref. [106], a finite-size scaling analysis was shown to be capable of detecting the many-body localization transition in the computational basis. Here, the participation ratio is used to investigate the crossover from the ergodic to the many-body localized phase in the Fock space constructed out of the natural orbitals.

The participation ratio is here interpreted as a measure of the effective Hilbert space dimension in which a state is confined. For a state $|\psi\rangle$ expressed in the basis spanned by orthonormal states $|i\rangle$ labeled by an index i , the participation ratio PR is given by

$$\text{PR} = \frac{1}{\sum_i |\langle \psi | i \rangle|^4}. \quad (6.31)$$

For a fully localized state, $\text{PR} = 1$, while $\text{PR} = N$ if $|\psi\rangle$ is a uniform superposition of N basis states. The interpretation of PR as an effective Hilbert space dimension has been adapted previously in for example works on many-body localization [115] and the

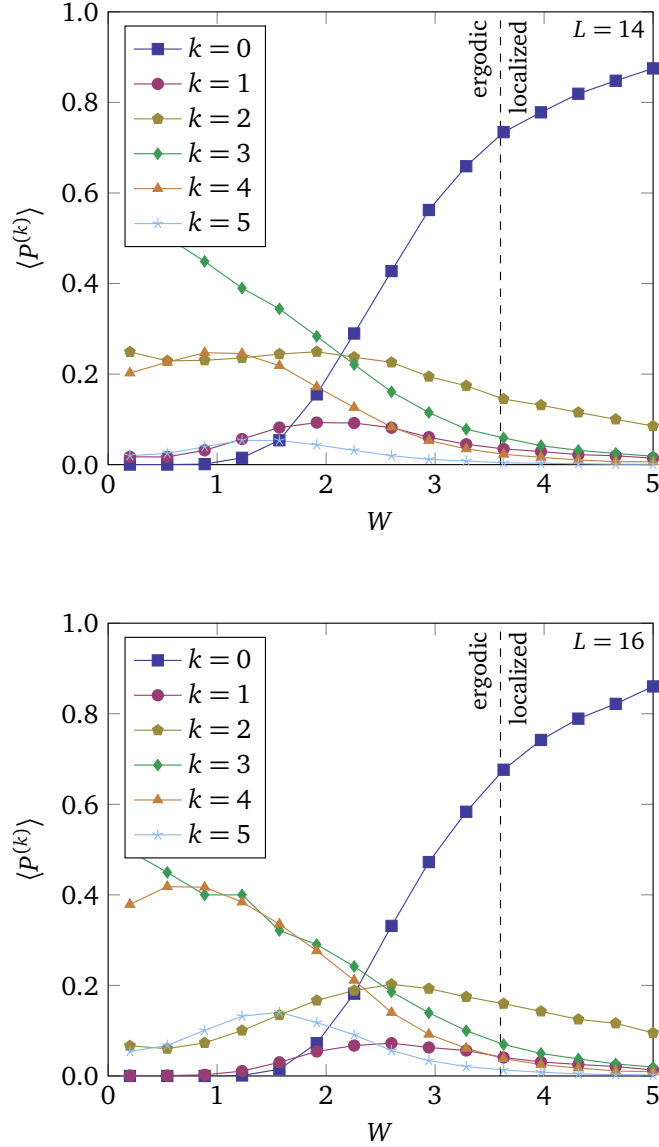


Fig. 6.3: The ensemble-averages of the overlaps $P^{(k)}$ for $k = 1, 2, \dots, 5$ as a function of the disorder strength W at system sizes $L = 14$ (top) and $L = 16$ (bottom). The many-body localization transition at $W \approx 3.6$ is indicated by vertical dashed lines. See the main text for computational details. For $L = 14$, an ergodic state is characterized by $P^{(0)} \approx 0.00$, $P^{(1)} \approx 0.00$, $P^{(2)} \approx 0.01$, $P^{(3)} \approx 0.13$, $P^{(4)} \approx 0.36$, and $P^{(5)} \approx 0.36$. For $L = 16$, an ergodic state is characterized by $P^{(0)} \approx 0.00$, $P^{(1)} \approx 0.00$, $P^{(2)} \approx 0.00$, $P^{(3)} \approx 0.06$, $P^{(4)} \approx 0.24$, and $P^{(5)} \approx 0.38$.

eigenstate thermalization hypothesis [116]. For the largest system size $L = 16$ studied here, one finds $\dim(H) = 12,870$. To account for the large range $[1, \dim(H)]$ over which PR can vary, below the logarithm $\log_{10}(\text{PR})$ is considered.

Ensemble average Fig. 6.4 shows the ensemble average $\langle \log_{10}(\text{PR}) \rangle$ for systems of size $L = 10, 12, 14, 16$ as a function of the disorder strength W in both the Fock and computational basis. An approximate disorder strength-independence for $W \lesssim 1.7$ can be observed in both bases, which suggests the presence of a crossover from an ergodic phase to a phase with broken ergodicity at a disorder strength below the many-body localization reported at $W \approx 3.6$.

Although the curves appear to be free of effects due to the finiteness of the number of samples, one might argue an estimation of the uncertainty is required. The uncertainties of averages is estimated using the standard statistical approach. For a set of independent observations $\{x_1, x_2, \dots, x_N\}$ from an unknown distribution, the estimates of the mean μ and variance σ^2 are estimated as

$$\mu = \frac{1}{N} \sum_{i=1}^N x_i, \quad (6.32)$$

$$\sigma^2 = \frac{1}{N(N-1)} \sum_{i=1}^N (x_i - \mu)^2. \quad (6.33)$$

As usual, the uncertainty of the mean is estimated as σ / \sqrt{N} .

Ensemble variance Second, the focus is on the variance of $\log_{10}(\text{PR})$. This investigation is motivated by the observation of Kjäll, Bardarson, and Pollmann from 2014 [117] that the ensemble of eigenstates at the intermediate region between ergodic and many-body localized phases consists of members originating from both sides. As a result, variances peak at the intermediate phase. This idea has been applied to the occupation entropy of the natural orbitals in ref. [91] and the eigenstate entanglement entropy in ref. [85] to detect the many-body localization transition.

The variance of $\log_{10}(\text{PR})$ within the ensemble is given by

$$\text{var}(\log_{10}(\text{PR})) = \langle (\log_{10}(\text{PR}) - \langle \log_{10} \text{PR} \rangle)^2 \rangle. \quad (6.34)$$

Fig. 6.5 shows $\text{var}(\log_{10}(\text{PR}))$ in the Fock and the computational bases for system sizes $L = 10, 12, 14, 16$ as a function of the disorder strength W . In both bases, one observes a peak centered around $W \approx 2.3$. For the system sizes under consideration, the peak becomes increasingly sharp with increasing system size. It is an open question is if the peak moves towards the MBL transition at $W \approx 3.6$ in the thermodynamic limit $L \rightarrow \infty$, although the figures suggest this not to be the case. Noteworthy, a similar peak has been observed in studies the ensemble variance of the bipartite entanglement entropy in refs. [107, 108].

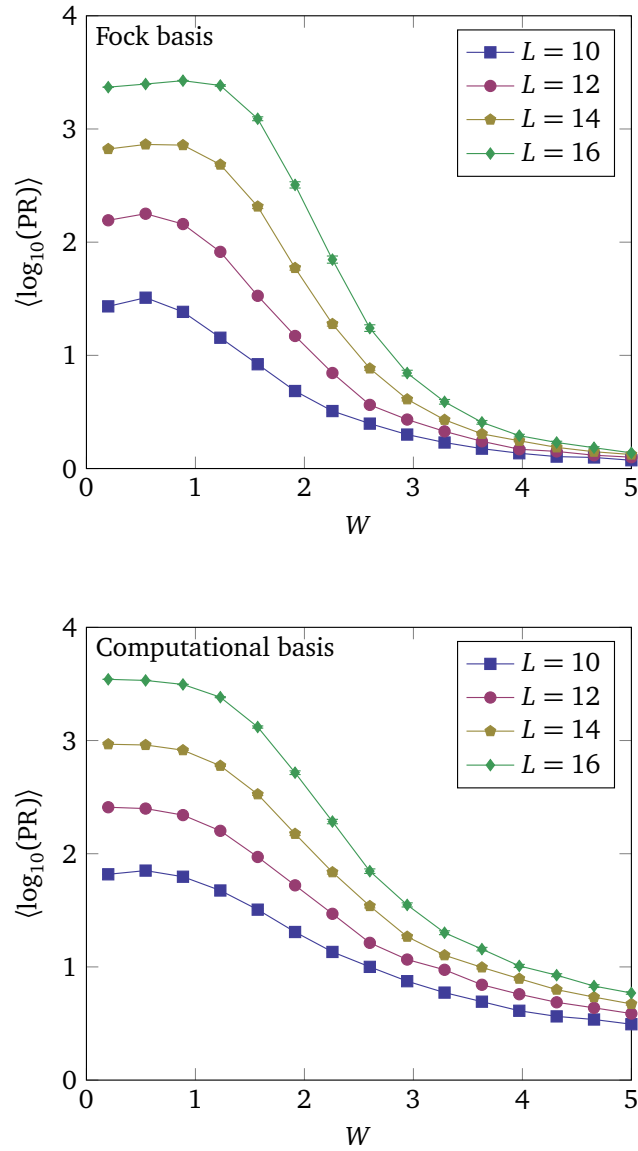


Fig. 6.4: The ensemble-averages of $\log_{10}(\text{PR})$ for $L = 10, 12, 14, 16$ in the Fock space constructed out of the natural orbitals (top) and the computational basis (bottom) as a function of the disorder strength W . Averages are taken over 1000 eigenstates. Error bars are mostly smaller than the marker size. See the main text for computational details.

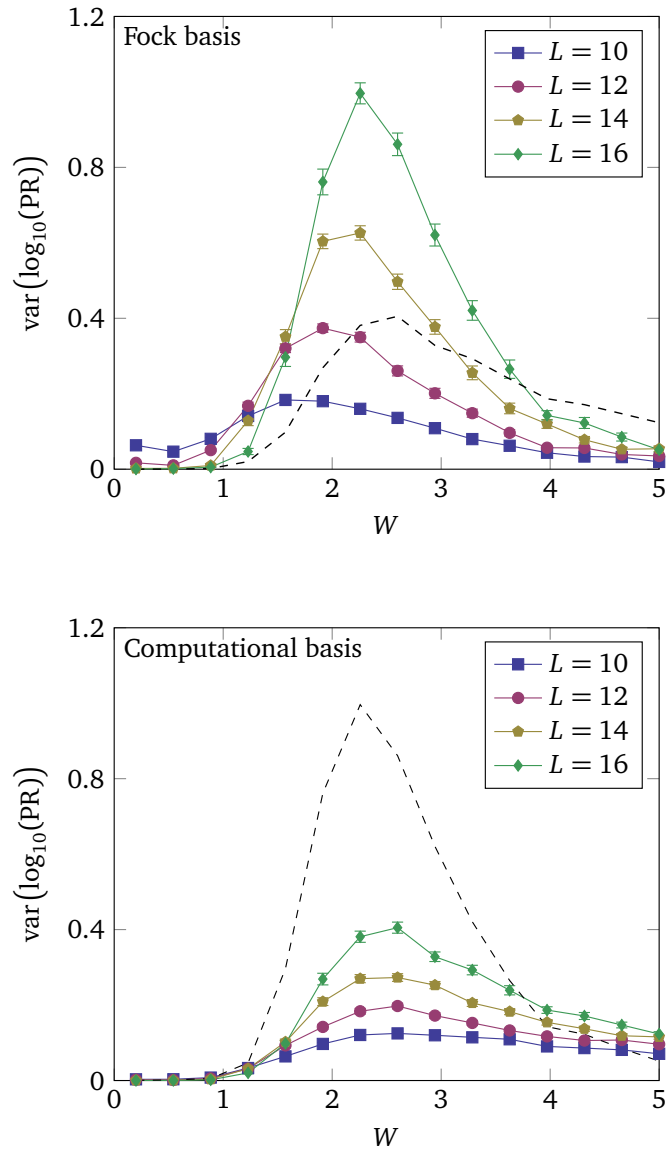


Fig. 6.5: The variances $\text{var}(\log_{10}(\text{PR}))$ for $L = 10, 12, 14, 16$ in the Fock space constructed out of the natural orbitals (top) and the computational basis (bottom) as a function of the disorder strength W . Averages are taken over 1000 eigenstates. For comparison, the dashed lines in the top (bottom) plot indicate $\text{var}(\log_{10}(\text{PR}))$ for $L = 16$ in the Fock (computational) basis. See the main text for computational details.

Hilbert space occupation Finally, the scaling of the participation ratio with the Hilbert space dimension is studied. As mentioned above, the participation ratio can be interpreted as an estimate for the dimension of the effective Hilbert space in which a state is confined. Hence, $10^{(\log_{10}(\text{PR}))} / \dim(H)$ can be seen as an indication for the fraction of the full Hilbert space that is occupied. Fig. 6.6 shows this quantity in the Fock and computational bases for $L = 10, 12, 14, 16$ as a function of the disorder strength W . Again, the figure suggests a crossover at $W \approx 2.3$ in both bases. It appears unlikely that the peak shifts towards the many-body localization transition at $W \approx 3.6$ in the thermodynamic limit $L \rightarrow \infty$.

Since $10^{(\log_{10}(\text{PR}))} / \dim(H)$ is not an average, the uncertainty can not be estimated using the approach used above. Here, jackknife resampling (see for example ref. [118]) is used to estimate the uncertainty. As above, consider a set of independent observations $\{x_1, x_2, \dots, x_N\}$ from an unknown distribution. Following the introduction section of the above-cited reference, let

$$\mu^{(i)} = \frac{1}{N-1} \sum_{j \neq i} x_j \quad (6.35)$$

$$\mu_{(\cdot)} = \frac{1}{N} \sum_{i=1}^N \mu^{(i)} \quad (6.36)$$

denote respectively the sample average of the data set with the i -th point omitted, and the mean of the $\mu_{(i)}$. Notice that $\mu = \mu_{(\cdot)}$. The jackknife estimate σ_J^2 of the variance is given by

$$\sigma_J^2 = \frac{N-1}{N} \sum_{i=1}^N (\mu_{(i)} - \mu_{(\cdot)}), \quad (6.37)$$

which can be verified to be equal to σ^2 as given above in eq. (6.33). This estimate can be generalized to functions $f(x_1, x_2, \dots, x_N)$ by the substitutions

$$f_{(i)} = f(x_1, x_2, \dots, x_{i-1}, x_{i+1}, x_{i+1}, \dots, x_N), \quad (6.38)$$

$$f_{(\cdot)} = \frac{1}{N} \sum_{i=1}^N f_{(i)}. \quad (6.39)$$

Note that a trivial proper choice of f allows one to estimate the uncertainty for $10^{(\log_{10}(\text{PR}))} / \dim(H)$.

6.8 Discussion and outlook

In this chapter, the focus was on many-body localization in the Fock basis constructed out of the natural orbitals. Motivated by studies on the occupation numbers and the interpretation of many-body localization as localization in Fock space, it was argued that the Fock space constructed out of the natural orbitals is a natural one in which

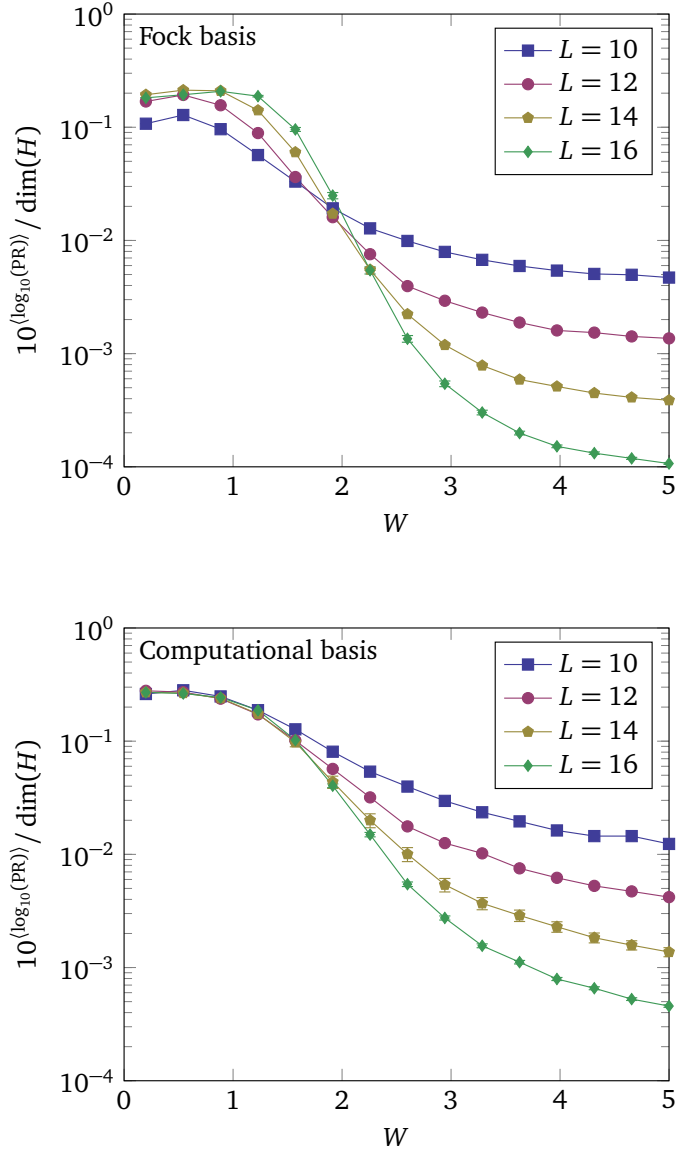


Fig. 6.6: Plots of $10^{(\log_{10}(\text{PR}))} / \dim(H)$ for system sizes $L = 10, 12, 14, 16$ in the Fock space constructed out of the natural orbitals (top) and the computational basis (bottom) as a function of the disorder strength W . Averages are taken over 1000 eigenstates. See the main text for computational details. Error bars (mostly smaller than the marker size) are determined by jackknife resampling. Note the logarithmic scales on the vertical axes.

to study many-body localization. The main result is the identification of a crossover between different phases centered at disorder strength $W \approx 2.3$.

The crossover identified in this chapter is located at the thermal side of the many-body localization transition. In parameter space, this crossover is accompanied by the breakdown of thermalization (see for example refs. [97] and [101]). Further investigations on the relation between these different phenomena might be valuable. Besides, it might be interesting to investigate whether there is a link with the notion that no signatures of the many-body localization transition have been observed.

Many-body localized eigenstates are localized in the Fock space constructed out of the natural orbitals more strongly than in the conventionally used computational basis. In future research, it could be interesting to search for even more optimal bases in which to study many-body localization. When adapting $P^{(0)}$ as given in eq. (6.20) as a measure of the localization of a state, one can not exclude that different single-particle states leading to even more strongly localized eigenstates can be found [119]. An iterative algorithm to find the optimal single-particle states achieving this has been proposed in ref. [120]. However, convergence of this algorithm is not guaranteed.

Gumbel statistics for many-body localized eigenstates

7.1 Introduction

Entanglement entropies can be extracted from entanglement spectra [28, 121]. Referring back to section 3.6.1, the most general setting is a quantum system divided into subsystems A and B with Hilbert space dimensions M and N . A pure state $|\psi\rangle$ of the composite system can be expanded in basis states $|a_i\rangle$ and $|b_i\rangle$ of the respective subsystems as

$$|\psi\rangle = \sum_{i,j} X_{ij} |a_i\rangle \otimes |b_j\rangle, \quad (7.1)$$

where X is an $M \times N$ matrix. Labeling the subsystems such that $M \geq N$, the Schmidt decomposition of X uniquely expands $|\psi\rangle$ as a linear combination of product states over the subsystems,

$$|\psi\rangle = \sum_{i=1}^N \sqrt{\lambda_i} |\alpha_i\rangle \otimes |\beta_i\rangle, \quad (7.2)$$

where $|\alpha_i\rangle$ and $|\beta_i\rangle$ are basis states for respectively subsystems A and B , and the λ_i ($\lambda_i \geq 0$) are the Schmidt coefficients. An element λ_i can be interpreted as the physical weight of the product state $|\alpha_i\rangle \otimes |\beta_i\rangle$, providing a contribution of $-\lambda_i \ln(\lambda_i)$ to the entanglement entropy. The elements e_i of the entanglement spectrum [28, 121] are given by

$$e_i = -\ln(\lambda_i) \quad (7.3)$$

The e_i can be interpreted as the eigenvalues of the *entanglement Hamiltonian*, introduced below.

At the localized side of the many-body localization transition [27], eigenstates obey area-law scaling of the entanglement entropy, while volume-law scaling is observed at the ergodic side [31]. The physical information encoded in the entanglement spectrum of a many-body localized eigenstate is almost fully carried by the smallest few elements [60], indicating the potential physical significance of the extreme value statistics. This chapter focuses on the extreme value statistics of entanglement spectra of many-body localized eigenstates.

Extreme value statistics display universal characteristics over a wide range of physically relevant conditions [122–125]. This chapter reports the observation of Gumbel statistics [126, 127]. These statistics apply to the extreme value of $N \rightarrow \infty$ independent samples drawn from a distribution with a faster than power-law asymptotic decay. This result provides an analytical, parameter-free characterization of many-body localized eigenstates.

Section 2 provides a brief overview of the literature on entanglement spectra in the context of many-body localization. Sections 3 and 4 discuss the technical background by focusing on respectively Gumbel statistics and entanglement spectra. In section 5, the physical setup is discussed. Section 6 shows the results, which are discussed in 7.

7.2 Literature review

This section provides a non-exhaustive list of previous investigations on entanglement spectra in the context of many-body localization.

1. Ref. [128] identifies a two-component structure in the entanglement spectra of many-body localized eigenstates. The focus is on a model closely related to the ‘standard model of many-body localization’ (see section 2.6), which is discussed in section 7.5 below. The system is splitted in equally-sized left- and right-hand sides. A deviation from the Marčenko-Pastur distribution (see section 3.6.4) is observed for larger Schmidt coefficients λ_i , while deviations are absent for the smaller coefficients.
2. Ref. [129] studies level spacing statistics (see section 3.5) of eigenstate entanglement spectra in many-body localized phases. The Schmidt coefficients obey Wigner-Dyson spacing statistics at the ergodic side of the many-body localization transition, consistent with the expectation for random states (see section 3.6). At the many-body localized side of the transition, a so-called semi-Poisson spacing distribution is observed. It should be remarked that the models studied in this work are qualitatively different from the model studied in this chapter.
3. Ref. [130] finds a power-law structure in the Schmidt spectra of many-body localized eigenstates. This observation is interpreted as a consequence of the emergence of local integrals of motion, as discussed in section 2.4.
4. Ref. [131] studies the Schmidt spectra of eigenstates at the ergodic side of the many-body localization transition. A correlation length, which diverges at the many-body localization transition, is extracted by a finite-size scaling analysis.

For completeness, the reader is made aware of a preprint by Pal and Lakshminarayan from 2020 [132] on extreme value statistics of eigenstate entanglement spectra in the context of many-body localization, whose initiation was driven by identical motivations as for the work on which this chapter is based.

7.3 Gumbel statistics

Following parts of the first chapter of the book ‘Extremes and Related Properties of Random Sequences and Processes’ by Leadbetter, Lindgren, and Rootzén [127], this section gives an introduction to Gumbel statistics. The content is also covered in section 3 of a recent pedagogical review by Majumdar, Pal, and Schehr [133].

Gumbel statistics – also known as Fisher-Tippett-Gumbel statistics [123] – are a type (specified below) of extreme value statistics. Consider a collection X_i ($i = 1, 2, \dots, N$) of independent and identically distributed random variables. Extreme value theory is concerned with the properties of the maximum

$$M_N = \max(X_1, X_2, \dots, X_N), \quad (7.4)$$

or the minimum by considering $-\max(-X_1, -X_2, \dots, -X_N)$. Let the cumulative density function of X_i be denoted by $F(x)$, meaning that

$$P\{X_i \leq x\} = F(x). \quad (7.5)$$

Notice that by construction $F(-\infty) = 0$ and $F(\infty) = 1$. Also notice the newly introduced notation “ $P\{\text{condition}\}$ ” for a probability density, adapted in this chapter to avoid notational ambiguities. It follows from the independence of the X_i that the cumulative density function of M_N is given by

$$P\{M_N \leq x\} = P\{X_1, X_2, \dots, X_N \leq x\}, \quad (7.6)$$

$$= F^N(x). \quad (7.7)$$

Below, the extremal types theorem is introduced. This theorem states that, when properly transformed, the distribution of M_N can take only three forms when considering limit $N \rightarrow \infty$.

7.3.1 Extremal types theorem

The extremal types theorem states that if there exist constants $a_N > 0$ and b_N such that one has

$$\lim_{N \rightarrow \infty} F^n(a_N x + b_N) = G(x), \quad (7.8)$$

then $G(x)$ can take only three possible forms (given below). In the context of extreme value statistics, two cumulative density functions F_1 and F_2 are said to be *of the same type* if

$$F_2(x) = F_1(ax + b) \quad (7.9)$$

for some $a > 0$ and b . Phrased differently, the extremal types theorem thus states that if there exist constants $a_N > 0$ and b_N such that eq. (7.8) holds, then the distribution of the maximum M_N can take only three possible forms. When N is large, M_N is sampled from the right-side tail of the probability distribution of X_i . The extremal types theorem thus distinguishes three types of tail distributions. These are referred to as the Gumbel, Fréchet, and Weibull distributions.

Gumbel distribution The Gumbel distribution is described by a cumulative density function

$$G(x) = \exp(-e^{-x}) \quad (7.10)$$

for $x \in (-\infty, \infty)$. Note the double-exponential form of $G(x)$. Gumbel statistics are observed when the probability distribution for the X_i has an unbounded faster-than-power-law asymptotic decay,

$$\lim_{x \rightarrow \infty} P\{X_i = x\} \sim \exp(-x^\alpha) \quad (7.11)$$

with $\alpha > 0$ a free parameter. Examples include exponential ($\alpha = 1$) and Gaussian ($\alpha = 2$) tails.

Considering $\alpha = 1$ for illustrative purposes, the probability distribution for the maximum M_N of N samples as defined in eq. (7.4) can be written as

$$P\{M_N = x\} = (1 - e^{-x})^N \quad (7.12)$$

$$= e^{N \ln(1 - e^{-x})} \quad (7.13)$$

$$\approx e^{N \exp(-x)} \quad (7.14)$$

$$= \exp(-e^{-(x - \ln(N))}) \quad (7.15)$$

$$= G(x - \ln(N)), \quad (7.16)$$

where the approximation $\ln(1 - x) \approx -x$ for $x \rightarrow 0$ is involved in the third line. By identifying $a_N = 1$ and $b_N = \ln(N)$, one finds that this distribution is of the same type as the one given in eq. (7.10) through eq. (7.9).

Fréchet distribution The Fréchet distribution is described by a cumulative density function

$$G(x) = \begin{cases} 0 & \text{if } x \leq 0, \\ \exp(-x^{-\alpha}) & \text{if } x > 0, \end{cases} \quad (7.17)$$

for some $\alpha > 0$. Fréchet statistics are observed when the probability distribution for the X_i has an unbounded power-law asymptotic decay,

$$\lim_{x \rightarrow \infty} P\{X_i = x\} \sim x^{-(1+\alpha)}. \quad (7.18)$$

The Pareto and Cauchy distributions are examples of distributions for which Fréchet extreme value statistics apply. These are not discussed as the focus in this chapter is on Gumbel statistics.

Weibull distribution The Weibull distribution is described by a cumulative density function

$$G(x) = \begin{cases} \exp(-(-x)^\alpha) & \text{if } x \leq 0, \\ 1 & \text{if } x > 0, \end{cases} \quad (7.19)$$

for some $\alpha > 0$. Weibull statistics are observed when the probability distribution for the X_i with an upper-bounded support. An example of distributions for which Weibull statistics apply is the uniform distribution, which again is not discussed here.

7.3.2 Shifting and scaling

As indicated by eq. (7.9), extreme value distributions are defined up to a shift and scale. To check whether two extreme value distributions are of the same type, one conventionally fixes these parameters by setting the mean to 0 and the variance to 1. Considering the Gumbel distribution, one thus needs to find parameters a and b such that the probability density function

$$g(x) = \frac{d}{dx} G(ax + b) \quad (7.20)$$

with $G(x)$ given in eq. (7.10) obeys the constraints

$$\int_{-\infty}^{\infty} x g(x) dx = 0, \quad \int_{-\infty}^{\infty} x^2 g(x) dx = 1 \quad (7.21)$$

to fix respectively the mean and variance. It can be verified that these constraints are satisfied for $a = \pi/\sqrt{6}$ and $b = \gamma$ with $\gamma \approx 0.577$ denoting Euler's constant. A selection of examples in which this distribution is considered is provided by refs. [122–125, 134–138].

For the Gumbel distribution, the probability density $g(x)$ for the maximum of $N \rightarrow \infty$ samples after proper shifting and scaling is given in explicit form by

$$g(x) = \frac{\pi}{\sqrt{6}} \exp \left[- \left(\frac{\pi}{\sqrt{6}} x + \gamma \right) - e^{-\left(\frac{\pi}{\sqrt{6}} x + \gamma \right)} \right]. \quad (7.22)$$

Fig. 7.1 shows a plot of $g(x)$ as given in eq. (7.22). For later reference, in addition the density

$$h(x) = \frac{1}{\sqrt{2\pi}} e^{-x^2/2} \quad (7.23)$$

for a standard normal distribution is shown. One observes an asymmetric shape, which is the main qualitative characteristic of the Gumbel distribution.

7.4 Entanglement spectra

The Schmidt decomposition introduced in section 3.6.1 can be used to obtain an entanglement spectrum. This section first discusses this decomposition at a technical level. Second, the entanglement Hamiltonian and the physical motivation for the entanglement spectrum are discussed. Finally, this section focuses on the properties of entanglement spectra for ergodic and localized states.

7.4.1 Schmidt decomposition

The discussion below essentially follows the first part of section 3.3.4 of the book 'Log-Gases and Random Matrices' by Forrester [41]. A Schmidt decomposition transformes

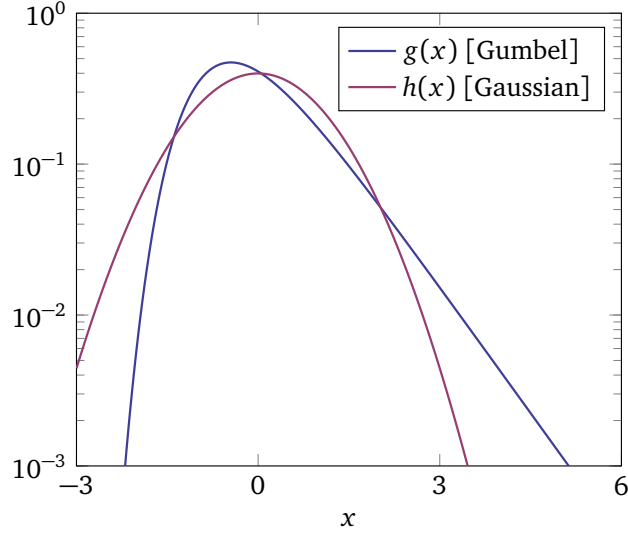


Fig. 7.1: Plots of the Gumbel distribution $g(x)$ and the standard Gaussian $h(x)$ as given in respectively eqs. (7.22) and (7.23). Note the logarithmic scale on the vertical axis.

a state $|\psi\rangle$ expanded in the form of eq. (7.1) to the form of eq. (7.2). As before, the focus is on a quantum system divided into subsystems A and B with Hilbert space dimensions M and N , labeled such that $N \leq M$. A state $|\psi\rangle$ of the composite system can be expanded in basis states $|a_i\rangle$ and $|b_i\rangle$ for the respective subsystems as

$$|\psi\rangle = \sum_{i,j} X_{ij} |a_i\rangle \otimes |b_j\rangle. \quad (7.24)$$

The reduced density matrix ρ_B is defined as the partial trace of the density matrix $\rho = |\psi\rangle\langle\psi|$ over the states $\{|a_i\rangle\}$ of subsystem A , meaning that $\rho_B = \text{Tr}_A(\rho)$. Explicitly,

$$\rho_B = \sum_i \langle a_i | \rho | a_i \rangle \quad (7.25)$$

$$= \sum_i \left[\sum_{j,k} X_{ji}^\dagger X_{ik} |b_j\rangle\langle b_k| \right] \quad (7.26)$$

$$= \sum_{j,k} (X^\dagger X)_{jk} |b_j\rangle\langle b_k|. \quad (7.27)$$

In a similar way, it follows that the reduced density matrix $\rho_A = \text{Tr}_B(\rho)$ of subsystem A is given by

$$\rho_A = \sum_{j,k} (XX^\dagger)_{jk} |a_j\rangle\langle a_k|. \quad (7.28)$$

Because $(XX^\dagger)^\dagger = X^\dagger X$, the matrix products $X^\dagger X$ and XX^\dagger have a common set of nonzero eigenvalues. The reduced density matrices ρ_A and ρ_B can as a result be expressed as

$$\rho_A = \sum_i \lambda_i |\alpha_i\rangle\langle\alpha_i|, \quad \rho_B = \sum_i \lambda_i |\beta_i\rangle\langle\beta_i|, \quad (7.29)$$

where $\{\lambda_i\}$ is the set of eigenvalues of $X^\dagger X$. Here, $|\alpha_i\rangle$ and $|\beta_i\rangle$ are basis states for subsystems A and B , respectively.

The density matrix ρ is given in terms of the reduced density matrices ρ_A and ρ_B by $\rho = \rho_A \otimes \rho_B$. By substituting ρ_A and ρ_B as given in eq. (7.29) in this expression, one trivially finds

$$\rho = \sum_i \lambda_i |\alpha_i\rangle \otimes |\beta_i\rangle \langle \beta_i| \otimes \langle \alpha_i|, \quad (7.30)$$

from which eq. (7.2) can be deduced directly by realizing that ρ has nonzero entries only on the diagonal. Computationally, the Schmidt spectrum $\{\lambda_i\}$ can thus be found by diagonalizing $X^\dagger X$. Alternatively, it could be obtained by a singular value decomposition of X .

7.4.2 Entanglement Hamiltonian

The reduced density matrix ρ_B of subsystem B contains all information accessible by measurements on subsystem B only. Specifically, the expectation value of an operator \mathcal{O}_B acting on subsystem B only is given by $\text{Tr}(\rho_B \mathcal{O}_B)$. One can write

$$\rho_B = \exp(-H_B). \quad (7.31)$$

The Hamiltonian H_B is known as the *entanglement Hamiltonian* [121]. The entanglement Hamiltonian is the result of an interpretation of ρ_B as the full density matrix of a ergodic system at temperature 1. By considering eq. (7.31) in the diagonal basis of eq. (7.29), it follows that the eigenvalues $\{e_i\}$ of the entanglement Hamiltonian are related to the Schmidt spectrum $\{\lambda_i\}$ by $\lambda_i = \exp(-e_i)$, or

$$e_i = -\ln(\lambda_i). \quad (7.32)$$

The spectrum $\{e_i\}$ is known as the *entanglement spectrum*. It is convenient to study entanglement by means of the entanglement spectrum. Remark that in some literature (see for example refs. [128, 130, 139]) the “quantum information definition” $e_i = \lambda_i$ of the entanglement spectrum is adapted.

7.4.3 Ground state energy

Consider a Schmidt spectrum λ_i ($i = 1, 2, \dots, N$). Many-body localized eigenstates are nearly unentangled [27]. The Schmidt spectrum of an unentangled state has only a single nonzero element of value 1. When assigning this element index $i = 1$, the elements e_i of the entanglement spectrum are given by

$$e_i = \begin{cases} 0 & \text{if } i = 1 \\ \infty & \text{if } i > 1. \end{cases} \quad (7.33)$$

One observes that the smallest element $e_i = 0$ plays a special role. Remark that because $\lambda_1 = 1$, this element also carries the full physical weight, as follows from the expansion given in eq. (7.2). In the numerical investigation discussed below, the focus is on the statistics of $-e_1$. The minus sign is added to allow for a comparison with Gumbel statistics, which are for the maximum element of a sequence.

The Schmidt spectra of ergodic states obey the statistics of the appropriate fixed-trace Wishart ensemble, as discussed in section 3.6. The joint probability density is according to eq. (3.44) proportional to

$$\prod_{i=1}^N \lambda_i^{\beta a/2} e^{-\beta \lambda_i/2} \prod_{j < k} |\lambda_j - \lambda_k|^\beta \quad (7.34)$$

with $\lambda_i \geq 0$, where $a = M - N + 1 - 2/\beta$, and $\beta \in \{1, 2, 4\}$ is the Dyson index as given in eq. (3.16), determined by the symmetry of the system with respect to reversing time. One deduces that the elements are strongly correlated, exhibiting level repulsion (discussed in section 3.5).

Gumbel statistics are observed for the extreme value statistics of certain sets of uncorrelated or weakly correlated elements [133]. The Schmidt spectra of ergodic states have strongly correlated elements, due to which the extreme value statistics do not obey Gumbel, nor any of the other types of extreme value statistics discussed in section 7.3.1. Instead, the probability density for the extreme value statistics of these Schmidt spectra (largest elements) as well as the corresponding entanglement spectra (smallest elements) turns out to be close to a Gaussian (numerical data not shown). As can be seen in fig. 7.1, these statistics differ at a qualitative level from Gumbel statistics.

7.5 Physical setup

This section consists of two parts. The first part discusses the model for which the eigenstate entanglement spectra are studied. In this part, also the numerical implementation is pointed out briefly. The second part discusses the way the system is splitted into subsystems.

7.5.1 Model and parameters

This chapter studies the model introduced in ref. [128], which is closely related to the ‘standard model of many-body localization’ discussed in section 2.6. The Hamiltonian H is given by

$$H = \sum_{i=1}^L \left[S_i^x S_{i+1}^x + S_i^y S_{i+1}^y + S_i^z S_{i+1}^z + h_i S_i^z + \Gamma S_i^x \right], \quad (7.35)$$

where L is the total number of sites. The spin-1/2 operators $S_i^{x,y,z}$ are defined in eq. (2.26). Periodic boundary conditions $S_{L+1}^{x,y,z} \equiv S_1^{x,y,z}$ are imposed. The onsite potentials h_i ($i = 1, 2, \dots, L$) are sampled independently from the probability distribution

$$P(x) = \begin{cases} 1/(2W) & \text{if } |x| \leq W, \\ 0 & \text{if } |x| > W, \end{cases} \quad (7.36)$$

which corresponds to the uniform distribution ranging over the interval $[-W, W]$. For $\Gamma = 0$, the model reduces to the ‘standard model of many-body localization’. As in the reference cited above, the parameter Γ is set to $\Gamma = 0.3$. For this model, indications for a many-body localization transition at $W \approx 3.5$ are reported (see the reference cited above).

In what follows, histograms (probability densities) are drawn from the combined data of at least 2.5×10^5 eigenstates. For Hamiltonians with $L = 10$ or $L = 12$, the 10 eigenstates associated with energies closest to the middle $(\max(E_i) + \min(E_i))/2$ of the spectrum E_i ($i = 1, 2, \dots, \dim(H)$) are involved in the analysis, while for Hamiltonians with $L = 14$ this number is set to 50. The eigenstates are obtained numerically by a procedure similar to the one discussed in section 4.5.2. As before, the computational software MATLAB, release 2017a [69] is used for all computations.

7.5.2 Splitting

For the entanglement spectra studied here, the system is splitted into equally-sized left- and right-hand subsystems A and B . Phrased differently, subsystems A and B cover respectively sites $\{1, 2, \dots, L/2\}$ and $\{L/2 + 1, L/2 + 2, \dots, L\}$. The number of elements in the corresponding entanglement spectra is $2^{L/2}$.

For the ‘standard model of many-body localization’ obtained by setting $\Gamma = 0$, the total spin projection S^z as given in eq. (2.28) is a conserved quantity. Consider a state $|\psi\rangle$ with a fixed total spin projection, expanded in terms of basis states $|a_i\rangle$ and $|b_i\rangle$ for respectively subsystems A and B as

$$|\psi\rangle = \sum_{i,j} X_{ij} |a_i\rangle \otimes |b_j\rangle. \quad (7.37)$$

Suppose without loss of generality that the basis states $|a_i\rangle$ and $|b_i\rangle$ can be labeled according to the total spin projections S_A^z and S_B^z of the subsystems given by

$$S_A^z = \sum_{i \in A} S_i^z, \quad S_B^z = \sum_{i \in B} S_i^z. \quad (7.38)$$

Since the total spin projection $S^z = S_A^z + S_B^z$ is conserved, the value of S_A^z determines the value of $S_B^z = S^z - S_A^z$. Consequently, the matrix X in (7.37) acquires a block-diagonal structure with the blocks labeled by either S_A^z or S_B^z . It is not hard to see that the

Schmidt decomposition of $|\psi\rangle$ yields a spectrum which is the union of independent subspectra. To avoid this, the conservation of the total spin projection is broken by setting $\Gamma = 0.3$ as in ref. [128].

7.6 Results

This section shows the main result, namely the observation of Gumbel statistics for the entanglement spectra of many-body localized eigenstates. Let $e_{\min} = \min_i(e_i)$ denote the smallest element of an entanglement spectrum. The focus is on the statistics of $-e_{\min}$, as Gumbel statistics are formulated for the largest element of a set.

Following section 7.3.2, the collection of extreme values obtained from distinct eigenstates is shifted and scaled such that the distribution has mean 0 and variance 1. As before, let $\langle \cdot \rangle$ denote an average, and let

$$\mu = \langle -e_{\min} \rangle, \quad \sigma^2 = \langle e_{\min}^2 \rangle - \langle e_{\min} \rangle^2 \quad (7.39)$$

denote respectively the estimated mean and variance of the distribution of e_{\min} . The analysis is concerned with the statistics of

$$\tilde{e}_{\min} = \frac{-e_{\min} - \mu}{\sqrt{\sigma^2}}, \quad (7.40)$$

which matches the required values for the mean and variance by construction.

Fig. 7.2 compares the density $P\{\tilde{e}_{\min} = x\}$ of \tilde{e}_{\min} for many-body localized eigenstates with the Gumbel distribution $g(x)$ as given in eq. (7.22) and the standard Gaussian $h(x)$ as given in eq. (7.23). The latter is observed when considering the entanglement spectra of ergodic states, as indicated in section 7.4.2. Good agreement with Gumbel statistics is observed for the largest system sizes $L = 12$ and $L = 14$. Deviations from Gumbel statistics can presumably be attributed to finite-size effects, as can be concluded from the observation the agreement becomes better with increasing system size. Finite-size effects come into play from two sides:

1. With increasing system size, eigenstates become more strongly localized [27].
2. The number $N = 2^{L/2}$ of elements of an entanglement spectrum increases with increasing system size. As mentioned above, Gumbel statistics are concerned with the limit $N \rightarrow \infty$.

As might be clear intuitively, the rate of convergence of extreme value statistics depends non-trivially on the parent distribution from which the samples are taken [140].

Fig. 7.3 compares the density $P\{\tilde{e}_{\min} = x\}$ of \tilde{e}_{\min} for eigenstates at the largest system size $L = 14$ with the Gumbel distribution $g(x)$ as given in eq. (7.22) and the standard Gaussian $h(x)$ as given in eq. (7.23) for disorder strengths $W = 2, 3, 4, 5$. Qualitative

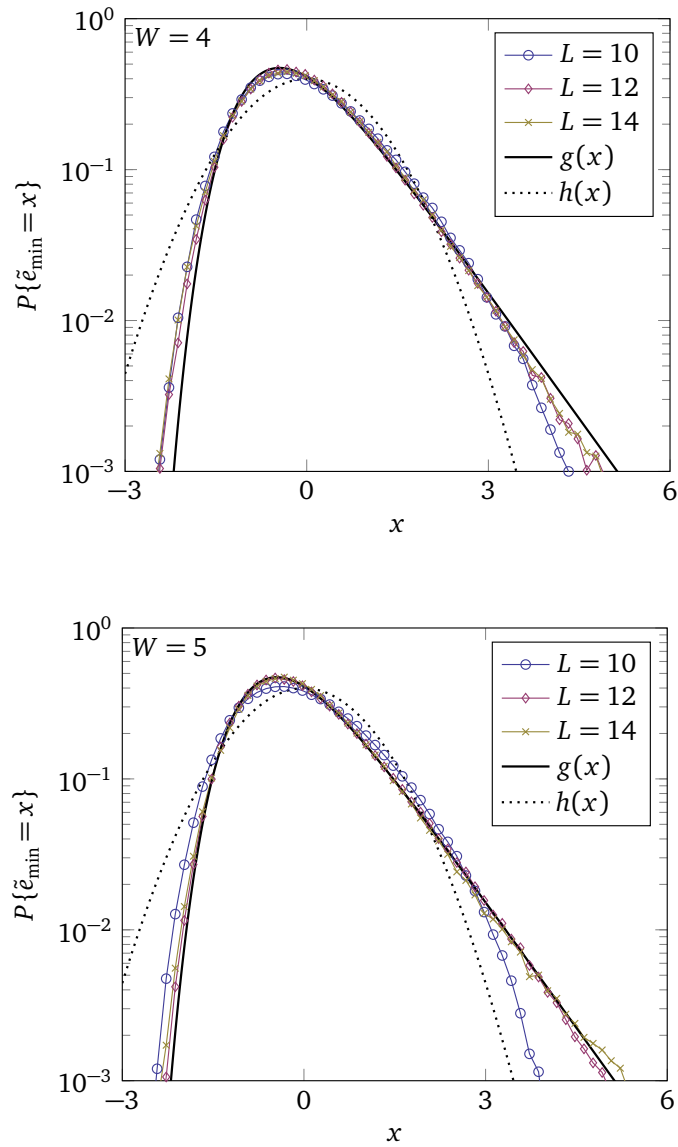


Fig. 7.2: The distribution of \tilde{e}_{\min} for disorder strengths $W = 4$ (top) and $W = 5$ (bottom) at system sizes $L = 10, 12, 14$, combined with the densities $g(x)$ for the Gumbel distribution and $h(x)$ for a standard Gaussian as given in eqs. (7.22) and (7.23), respectively. The probability density is approximated by a histogram with bins of width 0.05, which is normalized to unit area. Note the logarithmic scales on the vertical axes.

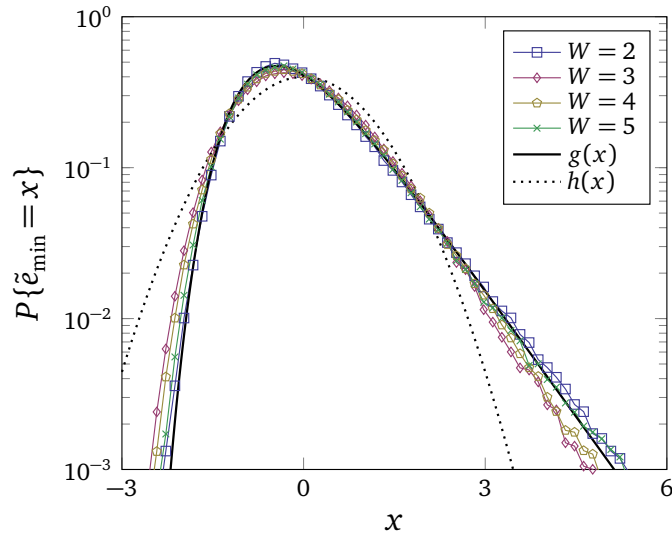


Fig. 7.3: The distribution of $\tilde{\epsilon}_{\min}$ for disorder strengths $W = 2, 3, 4, 5$ at system size $L = 14$, combined with the densities $g(x)$ and $h(x)$ as given in eqs. (7.22) and (7.23), respectively. The probability density is approximated by a histogram with bins of width 0.05, which is normalized to unit area. Note the logarithmic scales on the vertical axis.

similarities between the density of $\tilde{\epsilon}_{\min}$ and $g(x)$ can be observed for each of the disorder strengths.

Based on the results presented above, no conclusions can be drawn on the convergence of the distribution of $\tilde{\epsilon}_{\min}$ towards Gumbel statistics with increasing system size at the ergodic side of the many-body localization transition ($W \lesssim 3.5$). In an ergodic phase, the physical significance of the statistics of $\tilde{\epsilon}_{\min}$ is arguably limited due to the vanishing physical weight (given by the corresponding Schmidt coefficient) in the thermodynamic limit $L \rightarrow \infty$.

7.7 Discussion and outlook

The observation of Gumbel statistics suggests that the smallest elements of an entanglement spectrum obtained from a many-body localized eigenstate can be viewed as independent (uncorrelated) samples from a single distribution. Short-range correlations can be probed through the spacing statistics discussed in chapter 3. Let the $\tilde{\epsilon}_i$ be sorted in descending order (i.e. $\tilde{\epsilon}_i \geq \tilde{\epsilon}_{i+1}$), and let

$$r = \min\left(\frac{\tilde{\epsilon}_1 - \tilde{\epsilon}_2}{\tilde{\epsilon}_2 - \tilde{\epsilon}_3}, \frac{\tilde{\epsilon}_2 - \tilde{\epsilon}_3}{\tilde{\epsilon}_1 - \tilde{\epsilon}_2}\right). \quad (7.41)$$

The properties of the distribution of r are investigated in section 3.5.2. Summarizing, in the absence of short-range correlations, the distribution of r_1 obeys Poissonian statistics

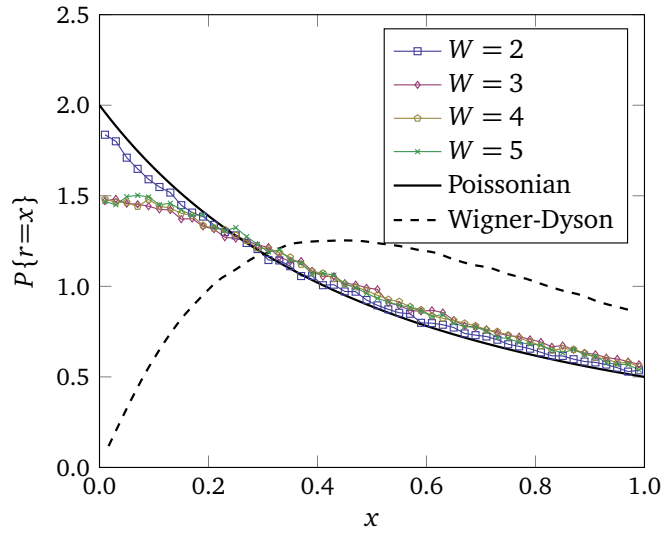


Fig. 7.4: The distribution of r as given in eq. (7.41) for disorder strengths $W = 2, 3, 4, 5$ at system size $L = 14$, combined with the distributions for Poissonian and Wigner-Dyson spacing statistics.

$$P\{r = x\} = \frac{2}{(1+x)^2}. \quad (7.42)$$

Because of the level repulsion (see section 7.4.3), ergodic states obey Wigner-Dyson spacing statistics. For systems with time-reversal symmetry (Dyson index $\beta = 1$), the corresponding density of r is well approximated by

$$P\{r = x\} \approx \frac{27}{8} \frac{x + x^2}{(1 + x + x^2)^{5/2}}. \quad (7.43)$$

Fig. 7.4 compares the distribution of r for $W = 2, 3, 4, 5$ at $L = 14$ with Poissonian and Wigner-Dyson spacing statistics. At disorder strengths $W = 2, 3, 4, 5$ the spacing statistics are close to Poissonian, indicating the (near) independence of the largest \tilde{e}_i .

The main open question remaining is the physical mechanism responsible for the occurrence of Gumbel statistics. A possible starting point for further investigations might be provided by the notion that an entanglement spectrum can be interpreted as the eigenvalue spectrum of the entanglement Hamiltonian introduced in section 7.4.2. One might hypothesize that the statistics of the eigenvector associated with e_{\min} carry relevant information.

Real symmetric tridiagonal matrices obey a number of special properties, of which two are utilized in the next section to establish a tridiagonal matrix model for the eigenvalues of the Gaussian beta ensemble. Consider the change of variables from

$$\vec{a} = (a_N, a_{N-1}, \dots, a_1), \quad \vec{b} = (b_{N-1}, b_{N-2}, \dots, b_1) \quad (\text{A.3})$$

to

$$\vec{\lambda} = (\lambda_1, \lambda_2, \dots, \lambda_N), \quad \vec{q} = (q_1, q_2, \dots, q_{N-1}). \quad (\text{A.4})$$

Remark that T is diagonalized by an orthogonal transformation, meaning that there are only $n - 1$ independent q_i as the sum of q_i^2 over $i = 1, 2, \dots, N$ equals 1.

The first property is that the determinant of the Jacobian $\det(J)$ for the transformation of variables from \vec{a}, \vec{b} to $\vec{\lambda}$ to \vec{q} evaluates to

$$\det(J) = \frac{1}{q_N} \frac{\prod_{i=1}^{N-1} b_i}{\prod_{i=1}^N q_i}, \quad (\text{A.5})$$

as is shown in ref. [141]. Remark that this expression does not depend on λ_i . The second property, derived in ref. [56], is that

$$\prod_{i < j} (\lambda_i - \lambda_j)^2 = \frac{\prod_{i=1}^{N-1} b_i^{2i}}{\prod_{i=1}^N q_i^2}. \quad (\text{A.6})$$

Besides in the references cited above, proofs of eqs. (A.5) and (A.6) can be found in the book referred to at the beginning of this section.

A.3 Gaussian beta ensemble

This section covers part of proposition 1.9.4 of the book ‘Log-Gases and Random Matrices’ by Forrester [41]. Consider a matrix T as given in eq. (A.1) above, and let $\beta > 0$ denote a fixed parameter. The elements a_i and b_i of T are independent random variables. The a_i are sampled from the probability distribution

$$P(a_i) = \frac{1}{\sqrt{2\pi}} e^{-a_i^2/2}, \quad (\text{A.7})$$

representing a Gaussian with mean 0 and variance 1. The b_i are sampled from the probability distribution

$$P(b_i) = \begin{cases} 0 & \text{if } b_i \leq 0, \\ \frac{2}{\Gamma(i\beta/2)} b_i^{i\beta-1} e^{-b_i^2} & \text{if } b_i > 0, \end{cases} \quad (\text{A.8})$$

meaning that the b_i are χ distributed with the shape parameter given by $i\beta$. Here, Γ represents the Gamma function. For an integer shape parameter k , samples from the

χ distribution are given by the square root of the sum of k squared samples from a Gaussian distribution with mean 0 and variance 1.

The joint probability distribution for T in terms of \vec{a} and \vec{b} is given by

$$P(\vec{a}, \vec{b}) = \prod_{i=1}^N P(a_i) \prod_{j=1}^{N-1} P(b_j) \quad (\text{A.9})$$

$$= \frac{2^{N-1}}{(2\pi)^{N/2}} \prod_{i=1}^n e^{-a_i^2/2} \prod_{j=1}^{N-1} \frac{b_j^{j\beta-1} e^{-b_j^2}}{\Gamma(j\beta/2)} \quad (\text{A.10})$$

$$= \frac{2^{N-1}}{(2\pi)^{N/2}} \prod_{i=1}^{N-1} \frac{b_i^{i\beta-1}}{\Gamma(i\beta/2)} e^{-\text{Tr}(T^2)/2} \quad (\text{A.11})$$

where it is assumed implicitly that all $b_i > 0$. By substituting eq. (A.5), it follows that the probability distribution in terms of $\vec{\lambda}$ and \vec{q} is given by

$$P(\vec{\lambda}, \vec{q}) = \frac{2^{N-1}}{(2\pi)^{N/2}} \prod_{i=1}^{N-1} \frac{1}{\Gamma(i\beta/2)} \frac{1}{q_N} \frac{\prod_{j=1}^{N-1} b_j^{j\beta}}{\prod_{j=1}^N q_j} e^{-\text{Tr}(T^2)/2} \quad (\text{A.12})$$

$$= \frac{2^{N-1}}{(2\pi)^{N/2}} \prod_{i=1}^{N-1} \frac{1}{\Gamma(i\beta/2)} \frac{1}{q_N} \frac{\prod_{j=1}^{N-1} b_j^{j\beta}}{\prod_{j=1}^N q_j} e^{-\frac{1}{2} \sum_{k=1}^N \lambda_k^2}. \quad (\text{A.13})$$

From eq. (A.6), it follows directly that

$$\prod_{i=1}^{N-1} b_i^{i\beta} = \prod_{i<j} |\lambda_i - \lambda_j|^\beta \prod_{k=1}^N q_k^\beta. \quad (\text{A.14})$$

Substituting eq. (A.14) in eq. (A.13), the expression for $P(\vec{\lambda}, \vec{q})$ factorizes in parts $P(\vec{\lambda})$ and $P(\vec{q})$ only depending on respectively $\vec{\lambda}$ and \vec{q} with

$$P(\lambda_1, \lambda_2, \dots, \lambda_N) = \frac{1}{C_{N,\beta}} \exp\left[-\frac{1}{2} \sum_{i=1}^N \lambda_i^2\right] \prod_{i<j} |\lambda_i - \lambda_j|^\beta, \quad (\text{A.15})$$

where $C_{N,\beta}$ is a normalization constant. Notice that this expression matches eq. (3.17).

A.4 Derivation for the Gaussian orthogonal ensemble

Following the steps in section 2.1 of ref. [56], it is shown below that the joint probability distribution for the eigenvalues of the Gaussian orthogonal ensemble agrees with eq. (A.15) for $\beta = 1$. Similar procedures can be followed for the Gaussian unitary ($\beta = 2$) and symplectic ($\beta = 4$) ensembles.

Consider a $N \times N$ matrix A sampled from the Gaussian orthogonal ensemble, meaning that the matrix is symmetric with the diagonal and upper triangular sampled independently from the respective probability distributions

$$P(x) = \frac{1}{\sqrt{2\pi}} e^{-x^2/2}, \quad P(x) = \frac{1}{\sqrt{\pi}} e^{-x^2}. \quad (\text{A.16})$$

One defines the $(N-1)$ -dimensional vector \vec{x} and the $(N-1) \times (N-1)$ matrix B as

$$\vec{x} = \begin{pmatrix} A_{12} \\ A_{13} \\ \vdots \\ A_{1N} \end{pmatrix}, \quad B = \begin{pmatrix} A_{22} & A_{23} & \cdots & A_{2N} \\ A_{23} & A_{33} & \cdots & A_{3N} \\ \vdots & \vdots & \ddots & \vdots \\ A_{2N} & A_{3N} & \cdots & A_{NN} \end{pmatrix}, \quad (\text{A.17})$$

such that A can be represented as

$$A = \begin{pmatrix} A_{11} & \vec{x}^T \\ \vec{x} & B \end{pmatrix}. \quad (\text{A.18})$$

The key step is to define an $(N-1) \times (N-1)$ symmetric matrix H obeying $H\vec{x} = \|\vec{x}\| \vec{e}_1$ with $\vec{e}_1 = (1, 0, 0, \dots, 0)^T$. Explicitly,

$$\begin{pmatrix} H_{11} & H_{12} & \cdots & H_{1(N-1)} \\ H_{12} & H_{22} & \cdots & H_{2(N-1)} \\ \vdots & \vdots & \ddots & \vdots \\ H_{1(N-1)} & H_{2(N-1)} & \cdots & H_{(N-1)(N-1)} \end{pmatrix} \begin{pmatrix} x_1 \\ x_2 \\ \vdots \\ x_{N-1} \end{pmatrix} = \|\vec{x}\| \begin{pmatrix} 1 \\ 0 \\ 0 \\ \vdots \\ 0 \end{pmatrix}, \quad (\text{A.19})$$

where $\|\vec{x}\| = \sqrt{x_1^2 + x_2^2 + \dots + x_{N-1}^2}$. The matrix H is required only to depend on \vec{x} . Next, it is required to be orthogonal, meaning that for any matrix M the eigenvalues of HMH^{-1} are the same as those of M .

Trivially, one has

$$\begin{pmatrix} 1 & 0 \\ 0 & H \end{pmatrix} \begin{pmatrix} A_{11} & \vec{x}^T \\ \vec{x} & B \end{pmatrix} \begin{pmatrix} 1 & 0 \\ 0 & H^T \end{pmatrix} = \begin{pmatrix} A_{11} & \|\vec{x}\| e_1^T \\ \|\vec{x}\| e_1 & HBH^T \end{pmatrix}. \quad (\text{A.20})$$

Since the Gaussian orthogonal ensemble is invariant under basis transformations and \vec{x} is independent of H , the sub-matrix HBH^{-1} is an $(N-1) \times (N-1)$ sample from the Gaussian orthogonal ensemble. Next, one observes that

$$\|\vec{x}\| = \sqrt{x_1^2 + x_2^2 + \dots + x_{N-1}^2} \sim \chi_{N-1}. \quad (\text{A.21})$$

Thus, iteratively repeating the above procedure on the sub-matrices brings A to the tridiagonal form discussed above for $\beta = 1$.

Computational aspects

B.1 Introduction

This appendix discusses the principles of the algorithms used for the numerical diagonalization of matrices. Section 2 discusses the basics of iterative diagonalization. Section 3 considers the QR diagonalization algorithm, which is utilized in exact diagonalization.

B.2 Iterative diagonalization

This section discusses some aspects of iterative methods for numerical eigenvalue problems, which are used in chapter 4 to determine the eigenvalues of matrices sampled from the Gaussian beta ensemble.

B.2.1 Power and inverse power methods

The content discussed in this section is covered in sections 6.2 and 6.3 of the book ‘Scientific Computing with MATLAB and Octave’ by Quarteroni, Saleri, and Gervasio [67]. Consider an $N \times N$ matrix T with (yet undetermined) non-degenerate eigenvalues λ_i ($i = 1, 2, \dots, N$), without loss of generality labeled such that

$$|\lambda_1| < |\lambda_2| < |\lambda_3| < \dots < |\lambda_N|. \quad (\text{B.1})$$

The eigenvalue λ_N having the largest modulus can be found iteratively by using the *power method*. Let \vec{x}_i denote the eigenvector associated with the eigenvalues λ_i , and let $\vec{x}^{(0)}$ be an N -dimensional vector which is non-orthogonal to \vec{x}_N . For $k \in \mathbb{N}$, let

$$\vec{x}^{(k)} = T\vec{y}^{(k-1)}, \quad \vec{y}^{(k)} = \frac{\vec{x}^{(k)}}{\|\vec{x}^{(k)}\|}. \quad (\text{B.2})$$

It is not difficult to see that the elements of the sequence $\{\vec{x}^{(k)}\}$ become an increasingly better approximation of \vec{x}_N with an increasing value of k . It follows that

$$\lim_{k \rightarrow \infty} \vec{x}^{(k)} = \vec{x}_N, \quad (\text{B.3})$$

showing that the eigenvector associated with the largest-modulus eigenvalue can be obtained iteratively. In practise, the sequence can be truncated at finite k .

The expression of the left-hand side of eq. (B.5) in terms of T and $\vec{x}^{(0)}$ involves a power of T , which justifies the name of the method. Eigenvectors \vec{x}_i with $i < N$ can be found by taking $\vec{x}^{(0)}$ orthogonal to \vec{x}_N , although one should take care of avoiding rounding-off errors inducing a nonzero overlap with \vec{x}_N at higher k . Modern computational software such as MATLAB typically uses improved algorithms (such as Lanczos or Arnoldi [68]) inspired by the power method.

The inverse T^{-1} of T shares a common set of eigenvectors \vec{x}_i with T . The eigenvalue μ_i associated with \vec{x}_i is given by $\mu_i = 1/\lambda_i$, where λ_i is the associated eigenvalue of T . Analog to the procedure followed above, let $\vec{x}^{(0)}$ be an N -dimensional vector which is non-orthogonal to \vec{x}_1 . For $k \in \mathbb{N}$ let

$$\vec{x}^{(k)} = T^{-1} \vec{y}^{(k-1)}, \quad \vec{y}^{(k)} = \frac{\vec{x}^{(k)}}{\|\vec{x}^{(k)}\|}. \quad (\text{B.4})$$

In this context, the power method is known as the *inverse power method*. As before, it follows that

$$\lim_{k \rightarrow \infty} \vec{x}^{(k)} = \vec{x}_1, \quad (\text{B.5})$$

indicating that the power method can be used to find the smallest-modulus eigenvalue too. As discussed below, the inverse power method can be implemented such that no matrix inversion (in terms of computational costs equivalent to full diagonalization) is required.

B.2.2 LU factorization method and Thomas algorithm

The content discussed in this section is covered in sections 5.3 (LU factorization method) and 5.6 (Thomas algorithm) of the book by Quarteroni, Saleri, and Gervasio [67] cited above. To find the smallest-modulus eigenvector of an $N \times N$ matrix T using the inverse power method, either the inverse T^{-1} has to be computed, or a matrix equation of the form $T\vec{x} = \vec{y}$ has to be solved at each iteration. The former operation is comparable to full diagonalization in terms of computational costs. The latter operation can be performed at relative low computational costs by using the LU factorization method.

The strategy is to efficiently solve equations of the form $T\vec{x} = \vec{y}$ is to write T in the factorized form $T = LU$ with L and U being respectively lower and upper triangular as

$$L = \begin{bmatrix} L_{11} & & & \\ L_{21} & L_{22} & & \\ \vdots & \vdots & \ddots & \\ L_{N1} & L_{N2} & \cdots & L_{NN} \end{bmatrix}, \quad U = \begin{bmatrix} U_{11} & U_{12} & \cdots & U_{1N} \\ & U_{22} & \cdots & U_{2N} \\ & & \ddots & \vdots \\ & & & U_{NN} \end{bmatrix}. \quad (\text{B.6})$$

with coefficients β_i ($i = 2, 3, \dots, N$) and γ_i ($i = 1, 2, \dots, N$). From $LU = T$, it follows that the coefficients can be obtained by the recursive relations

$$\gamma_1 = a_1, \quad (\text{B.13})$$

$$\beta_i = \frac{b_1}{\alpha_{i-1}}, \quad \gamma_i = a_i - \beta_i b_{i-1} \quad (i = 2, 3, \dots, N). \quad (\text{B.14})$$

Analog to the above, one can find the elements of $\vec{v} = (v_1, v_2, \dots, v_N)$ and $\vec{x} = (x_1, x_2, \dots, x_N)$ by the iterative relations

$$v_1 = y_1, \quad (\text{B.15})$$

$$v_i = y_i - \beta_i v_{i-1} \quad (i = 2, 3, \dots, N), \quad (\text{B.16})$$

for $L\vec{v} = \vec{y}$ and

$$x_n = \frac{y_n}{\gamma_n}, \quad (\text{B.17})$$

$$x_i = \frac{y_i - b_i x_{i+1}}{\gamma_i} \quad (i = N-1, N-2, \dots, 1), \quad (\text{B.18})$$

for $U\vec{x} = \vec{v}$, respectively. The procedure outlined here is known as the *Thomas algorithm*. In chapter 4, the Thomas algorithm is used in the determination of eigenvalues of matrices sampled from the Gaussian beta ensemble.

B.3 QR diagonalization

For the full diagonalization of matrices, modern computational software uses a routine based on the *QR algorithm* [67]. Full diagonalization is used in this dissertation to find the eigenvalues (and sometimes, the eigenvectors) of Hamiltonians, one-particle occupation matrices, and reduced density matrices. This section briefly discusses the QR algorithm. The content discussed in this section is covered in ref. [70], in which the algorithm was first proposed.

A matrix T can be factorized as $T = QR$, where Q is unitary ($QQ^{-1} = \mathbb{1}$) and R is upper triangular. Computationally, the matrices Q and R are commonly obtained through the Householder algorithm, discussed in most standard works on linear algebra. The QR algorithm consider matrices $T^{(i)}$ ($i \in \mathbb{N}$) factorized as $T^{(i)} = Q^{(i)} R^{(i)}$ with $Q^{(i)}$ and $R^{(i)}$ being respectively unitary and upper triangular. The algorithm constructs $T^{(i)}$ iteratively from T by

$$T^{(1)} = T \quad (\text{B.19})$$

$$T^{(i)} = R^{(i-1)} Q^{(i-1)} \quad (i = 2, 3, \dots). \quad (\text{B.20})$$

Notice that here the upper triangular matrix appears before the orthogonal one. Since $R^{(i)} = [Q^{(i)}]^{-1} T^{(i)}$, it follows that $T^{(i)} = [Q^{(i-1)}]^{-1} T^{(i-1)} Q^{(i-1)}$, which indicates that all $T^{(i)}$ have a common set of eigenvalues.

Under the condition that all eigenvalues of T have a different modulus, one can show that the i -th eigenvalue and corresponding eigenvector appears as the i -th diagonal elements of a matrix \tilde{T} and i -th column of a matrix \tilde{Q} given by

$$\tilde{T} = \lim_{i \rightarrow \infty} T^{(i)}, \quad \tilde{Q} = \prod_{i=1}^{\infty} Q^{(i)}. \quad (\text{B.21})$$

Remark that one can omit the calculation of \tilde{Q} when one is only interested in the eigenvalues, as is the case in for example chapter 4.

B.4 Determinants

The content discussed in this section is covered in section 1,4 of the book by Quarteroni, Saleri, and Gervasio [67] cited above, as well as the documentation of MATLAB R2017a [69]. Consider an $N \times N$ matrix T ,

$$T = \begin{pmatrix} T_{11} & T_{12} & \cdots & T_{1N} \\ T_{21} & T_{22} & \cdots & T_{2N} \\ \vdots & \vdots & \ddots & \vdots \\ T_{N1} & T_{N2} & \cdots & T_{NN} \end{pmatrix}. \quad (\text{B.22})$$

The goal is to calculate the determinant $\det(T)$. The determinant can be calculated recursively by using the Laplace rule:

$$\det(T) = \begin{cases} T_{11} & \text{if } N = 1, \\ \sum_{j=1}^N (-1)^{i+j} T_{ij} \det(T^{ij}) & \text{if } N \geq 2, \forall i \in \{1, 2, \dots, N\}, \end{cases} \quad (\text{B.23})$$

where T^{ij} is the matrix obtained by eliminating the i -th row and the j -th column from T without further relabeling. The result is independent of i .

Although eq. (B.23) can be implemented numerically in a straightforward way, the algorithm is computationally much more expensive than necessary. Aiming to introduce the algorithm used by modern computational software, consider the lower and upper-triangular matrices L and U as given in eq. (B.6),

$$L = \begin{bmatrix} L_{11} & & & \\ L_{21} & L_{22} & & \\ \vdots & \vdots & \ddots & \\ L_{N1} & L_{N2} & \cdots & L_{NN} \end{bmatrix}, \quad U = \begin{bmatrix} U_{11} & U_{12} & \cdots & U_{1N} \\ & U_{22} & \cdots & U_{2N} \\ & & \ddots & \vdots \\ & & & U_{NN} \end{bmatrix}. \quad (\text{B.24})$$

By choosing i to have the lowest (highest) possible value, the determinant of L (U) follows to be given by the products of the diagonal terms,

$$\det(L) = \prod_{i=1}^N L_{ii}, \quad \det(U) = \prod_{i=1}^N U_{ii}. \quad (\text{B.25})$$

The algorithm to determine the determinant of a generic $N \times N$ matrix T works in 2 steps: first, the matrix T is decomposed as $T = LU$ with L and U given above by using the LU factorization algorithm as discussed in section 2.2 of this appendix above. Second, the determinant is determined by using the property that for $N \times N$ matrices A , B , and C with $A = BC$ holds that

$$\det(A) = \det(B) \times \det(C), \tag{B.26}$$

as is discussed in most introductions on linear algebra.

Bibliography

- [1] W. Buijsman, V. Gritsev, and V. Cheianov, Many-body localization in the Fock space of natural orbitals , *SciPost Phys.* **4**, 038 (2018).
- [2] W. Buijsman, V. Cheianov, and V. Gritsev, Random Matrix Ensemble for the Level Statistics of Many-Body Localization, *Phys. Rev. Lett.* **122**, 180601 (2019).
- [3] W. Buijsman, V. Gritsev, and V. Cheianov, Gumbel statistics for entanglement spectra of many-body localized eigenstates, *Phys. Rev. B* **100**, 205110 (2019).
- [4] W. Buijsman and M. Sheinman, Efficient fold-change detection based on protein-protein interactions, *Phys. Rev. E* **89**, 022712 (2014).
- [5] W. Buijsman, V. Gritsev, and R. Sprik, Nonergodicity in the Anisotropic Dicke Model, *Phys. Rev. Lett.* **118**, 080601 (2017).
- [6] D.M. Basko, I.L. Aleiner, and B.L. Altshuler, Metal–insulator transition in a weakly interacting many-electron system with localized single-particle states, *Ann. Phys.* **321**, 1126 (2006).
- [7] D. A. Huse, R. Nandkishore, and V. Oganesyan, Phenomenology of fully many-body-localized systems, *Phys. Rev. B* **90**, 174202 (2014).
- [8] D. A. Abanin, E. Altman, I. Bloch, and M. Serbyn, Colloquium: Many-body localization, thermalization, and entanglement, *Rev. Mod. Phys.* **91**, 021001 (2019).
- [9] P. W. Anderson, Absence of Diffusion in Certain Random Lattices, *Phys. Rev.* **109**, 1492 (1958).
- [10] E. Abrahams, P. W. Anderson, D. C. Licciardello, and T. V. Ramakrishnan, Scaling Theory of Localization: Absence of Quantum Diffusion in Two Dimensions, *Phys. Rev. Lett.* **42**, 673 (1979).
- [11] M. Schreiber and H. Grussbach, Multifractal wave functions at the Anderson transition, *Phys. Rev. Lett.* **67**, 607 (1991).
- [12] B. Kramer and A. MacKinnon, Localization: theory and experiment, *Rep. Prog. Phys.* **56**, 1469 (1993).
- [13] F. Evers and A. D. Mirlin, Anderson transitions, *Rev. Mod. Phys.* **80**, 1355 (2008).
- [14] L. Fleishman and P. W. Anderson, Interactions and the Anderson transition, *Phys. Rev. B* **21**, 2366 (1980).
- [15] I. V. Gornyi, A. D. Mirlin, and D. G. Polyakov, Interacting Electrons in Disordered Wires: Anderson Localization and Low- T Transport, *Phys. Rev. Lett.* **95**, 206603 (2005).

-
- [16] P-O. Löwdin, Quantum Theory of Many-Particle Systems. I. Physical Interpretations by Means of Density Matrices, Natural Spin-Orbitals, and Convergence Problems in the Method of Configurational Interaction, *Phys. Rev.* **97**, 1474 (1955).
- [17] V. Oganesyan and D. A. Huse, Localization of interacting fermions at high temperature, *Phys. Rev. B* **75**, 155111 (2007).
- [18] D. A. Abanin, J. H. Bardarson, G. De Tomasi, S. Gopalakrishnan, V. Khemani, S. A. Parameswaran, F. Pollmann, A. C. Potter, M. Serbyn, and R. Vasseur, Distinguishing localization from chaos: challenges in finite-size systems, arXiv:1911.04501 (2019).
- [19] J. Z. Imbrie, On Many-Body Localization for Quantum Spin Chains, *J. Stat. Phys.* **163**, 998 (2016).
- [20] J. Z. Imbrie, Diagonalization and Many-Body Localization for a Disordered Quantum Spin Chain, *Phys. Rev. Lett.* **117**, 027201 (2016).
- [21] W. De Roeck and F. Huveneers, Stability and instability towards delocalization in many-body localization systems, *Phys. Rev. B* **95**, 155129 (2017).
- [22] V. Ros, M. Müller, and A. Scardicchio, Integrals of motion in the many-body localized phase, *Nucl. Phys. B* **891**, 420 (2015).
- [23] F. Alet and N. Laflorencie, Many-body localization: An introduction and selected topics, *Comptes Rendus Physique* **19**, 498 (2018).
- [24] M. L. Mehta, *Random Matrices*, 3rd ed., Pure and Applied Mathematics, Vol. 142 (Elsevier, New York, 2004).
- [25] Y. Y. Atas, E. Bogomolny, O. Giraud, and G. Roux, Distribution of the Ratio of Consecutive Level Spacings in Random Matrix Ensembles, *Phys. Rev. Lett.* **110**, 084101 (2013).
- [26] A. Pal and D. A. Huse, Many-body localization phase transition, *Phys. Rev. B* **82**, 174411 (2010).
- [27] D. J. Luitz, N. Laflorencie, and F. Alet, Many-body localization edge in the random-field Heisenberg chain, *Phys. Rev. B* **91**, 081103 (2015).
- [28] N. Laflorencie, Quantum entanglement in condensed matter systems, *Phys. Rep.* **646**, 1 (2016).
- [29] P. Vivo, M. P. Pato, and G. Oshanin, Random pure states: Quantifying bipartite entanglement beyond the linear statistics, *Phys. Rev. E* **93**, 052106 (2016).
- [30] C. Bauer, B. and Nayak, Area laws in a many-body localized state and its implications for topological order, *J. Stat. Mech.* **2013**, P09005 (2013).
- [31] P. T. Dumitrescu, R. Vasseur, and A. C. Potter, Scaling Theory of Entanglement at the Many-Body Localization Transition, *Phys. Rev. Lett.* **119**, 110604 (2017).
- [32] D. N. Page, Average entropy of a subsystem, *Phys. Rev. Lett.* **71**, 1291 (1993).

- [33] M. Žnidarič, T. Prosen, and P. Prelovšek, Many-body localization in the Heisenberg XXZ magnet in a random field, *Phys. Rev. B* **77**, 064426 (2008).
- [34] J. H. Bardarson, F. Pollmann, and J. E. Moore, Unbounded Growth of Entanglement in Models of Many-Body Localization, *Phys. Rev. Lett.* **109**, 017202 (2012).
- [35] M. Serbyn, Z. Papić, and D. A. Abanin, Universal Slow Growth of Entanglement in Interacting Strongly Disordered Systems, *Phys. Rev. Lett.* **110**, 260601 (2013).
- [36] E. P. Wigner, On the statistical distribution of the widths and spacings of nuclear resonance levels, *Proc. Cambridge Philos. Soc.* **47**, 790 (1951).
- [37] F. J. Dyson, Statistical Theory of the Energy Levels of Complex Systems. I, *J. Math. Phys.* **3**, 140 (1962).
- [38] T. A. Brody, J. Flores, J. B. French, P. A. Mello, A. Pandey, and S. S. M. Wong, Random-matrix physics: spectrum and strength fluctuations, *Rev. Mod. Phys.* **53**, 385 (1981).
- [39] T. Guhr, A. Müller-Groeling, and H. A. Weidenmüller, Random-matrix theories in quantum physics: common concepts, *Phys. Rep.* **299**, 189 (1998).
- [40] L. D'Alessio, Y. Kafri, A. Polkovnikov, and M. Rigol, From quantum chaos and eigenstate thermalization to statistical mechanics and thermodynamics, *Adv. Phys.* **65**, 239 (2016).
- [41] P. J. Forrester, *Log-Gases and Random Matrices*, London Mathematical Society Monographs, Vol. 34 (Princeton University Press, Princeton and Oxford, 2010).
- [42] O. Bohigas, M. J. Giannoni, and C. Schmit, Characterization of Chaotic Quantum Spectra and Universality of Level Fluctuation Laws, *Phys. Rev. Lett.* **52**, 1 (1984).
- [43] F. J. Dyson, Statistical Theory of the Energy Levels of Complex Systems. II, *J. Math. Phys.* **3**, 157 (1962).
- [44] G. Livan, M. Novaes, and P. Vivo, *Introduction to Random Matrices*, SpringerBriefs in Mathematical Physics, Vol. 26 (Springer, New York, 2018).
- [45] E. P. Wigner, On the distribution of the roots of certain symmetric matrices, *Ann. Math.* **67**, 325 (1958).
- [46] I. Dumitriu and A. Edelman, Global spectrum fluctuations for the β -hermite and β -laguerre ensembles via matrix models, *J. Math. Phys.* **47**, 063302 (2006).
- [47] F. J. Dyson, A Class of Matrix Ensembles, *J. Math. Phys.* **13**, 90 (1971).
- [48] G. Hackenbroich and H. A. Weidenmüller, Universality of Random-Matrix Results for Non-Gaussian Ensembles, *Phys. Rev. Lett.* **74**, 4118 (1995).
- [49] F. Mezzadri, How to Generate Random Matrices from the Classical Compact Groups, *Not. Am. Math. Soc.* **54**, 592 (2007).
- [50] M. V. Berry and M. Tabor, Level Clustering in the Regular Spectrum, *Proc. R. Soc. A* **356**, 375 (1977).

-
- [51] J.-S. Caux and J. Mossel, Remarks on the notion of quantum interability, *J. Stat. Phys.* **2011**, P02023 (2011).
- [52] F. Haake, *Quantum Signatures of Chaos*, 3rd ed., Springer Series in Synergetics, Vol. 54 (Springer-Verlag, Berlin, Heidelberg, 2010).
- [53] Y. Y. Atas, E. Bogomolny, O. Giraud, P. Vivo, and E. Vivo, Joint probability densities of level spacing ratios in random matrices, *J. Phys. A: Math. Th.* **46**, 355204 (2013).
- [54] V. A. Marchenko and L. A. Pastur, Distribution of eigenvalues for some sets of random matrices, *Math. USSR-Sbornik* **1**, 457 (1967).
- [55] K. Życzkowski, K. A. Penson, I. Nechita, and B. Collins, Generating random density matrices, *J. Math. Phys.* **52**, 062201 (2011).
- [56] I. Dumitriu and A. Edelman, Matrix models for beta ensembles, *J. Math. Phys.* **43**, 5830 (2002).
- [57] N. Rosenzweig and C. E. Porter, “Repulsion of Energy Levels” in Complex Atomic Spectra, *Phys. Rev.* **120**, 1698 (1960).
- [58] T. A. Brody, A Statistical Measure for the Repulsion of Energy Levels, *Lett. Nuovo Cimento* **7**, 482 (1973).
- [59] T. A. Brody, P. A. Mello, J. Flores, and O. Bohigas, Doorway States and Nuclear-Spectrum Statistics, *Lett. Nuovo Cimento* **7**, 707 (1973).
- [60] M. Serbyn and J. E. Moore, Spectral statistics across the many-body localization transition, *Phys. Rev. B* **93**, 041424 (2016).
- [61] B. I. Shklovskii, B. Shapiro, B. R. Sears, P. Lambrianides, and H. B. Shore, Statistics of spectra of disordered systems near the metal-insulator transition, *Phys. Rev. B* **47**, 11487 (1993).
- [62] C. W. J. Beenakker, J. M. Edge, J. P. Dahlhaus, D. I. Pikulin, Shuo Mi, and M. Wimmer, Wigner-Poisson Statistics of Topological Transitions in a Josephson Junction, *Phys. Rev. Lett.* **111**, 037001 (2013).
- [63] V. E. Kravtsov, I. M. Khaymovich, E. Cuevas, and M. Amini, A random matrix model with localization and ergodic transitions, *New J. Phys.* **17**, 122002 (2015).
- [64] P. Sierant and J. Zakrzewski, Level statistics across the many-body localization transition, *Phys. Rev. B* **99**, 104205 (2019).
- [65] E. Bogomolny, U. Gerland, and C. Schmit, Short-range plasma model for intermediate spectral statistics, *Eur. Phys. J. B* **19**, 121 (2001).
- [66] F. Benaych-Georges and S. Péché, Poisson Statistics for Matrix Ensembles at Large Temperature, *J. Stat. Phys.* **161**, 633 (2015).
- [67] A. Quarteroni, F. Saleri, and P. Gervasio, *Scientific Computing with MATLAB and Octave*, 3rd ed., Texts in Computational Science and Engineering, Vol. 2 (Springer, Berlin, Heidelberg, 2010).

- [68] F. Pietracaprina, N. Macé, D. J. Luitz, and F. Alet, Shift-invert diagonalization of large many-body localizing spin chains, *SciPost Phys.* **6**, 045 (2018).
- [69] The MathWorks Inc., MATLAB version 9.2.0.556344 / R2017a.
- [70] J. G. F. Francis, The QR transformation, A unitary analogue to the LR transformation—Part 1, *Comput. J.* **4**, 265 (1961).
- [71] Wolfram Research Inc., MATHEMATICA version 10.0.
- [72] J. M. G. Gómez, R. A. Molina, A. Relaño, and J. Retamosa, Misleading signatures of quantum chaos, *Phys. Rev. E* **66**, 036209 (2002).
- [73] Y. Avishai, J. Richert, and R. Berkovits, Level statistics in a Heisenberg chain with random magnetic field, *Phys. Rev. B* **66**, 052416 (2002).
- [74] S. H. Tekur, U. T. Bhosale, and M. S. Santhanam, Higher-order spacing ratios in random matrix theory and complex quantum systems, *Phys. Rev. B* **98**, 104305 (2018).
- [75] J. Šuntajs, J. Bonča, T. Prosen, and L. Vidmar, Quantum chaos challenges many-body localization, arXiv:1905.06345v2 (2019).
- [76] P. Sierant and J. Zakrzewski, Model of level statistics for disordered interacting quantum many-body systems, *Phys. Rev. B* **101**, 104201 (2020).
- [77] J. H. Shirley, Solution of the Schrödinger Equation with a Hamiltonian Periodic in Time, *Phys. Rev.* **138**, B979 (1965).
- [78] P. J. Forrester, B. Jancovici, and D. S. McAnally, Analytic Properties of the Structure Function for the One-Dimensional One-Component Log-Gas, *J. Stat. Phys.* **102**, 737 (2001).
- [79] E. Brézin and S. Hikami, Spectral form factor in a random matrix theory, *Phys. Rev. E* **55**, 4067 (1997).
- [80] J. T. Edwards and D. J. Thouless, Numerical studies of localization in disordered systems, *J. Phys. C: Solid State Phys.* **5**, 807 (1972).
- [81] P. Kos, M. Ljubotina, and T. Prosen, Many-Body Quantum Chaos: Analytic Connection to Random Matrix Theory, *Phys. Rev. X* **8**, 021062 (2018).
- [82] A. Chan, A. De Luca, and J. T. Chalker, Spectral Statistics in Spatially Extended Chaotic Quantum Many-Body Systems, *Phys. Rev. Lett.* **121**, 060601 (2018).
- [83] A. J. Friedman, A. Chan, A. De Luca, and J. T. Chalker, Spectral Statistics and Many-Body Quantum Chaos with Conserved Charge, *Phys. Rev. Lett.* **123**, 210603 (2019).
- [84] P. Sierant, D. Delande, and J. Zakrzewski, Thouless Time Analysis of Anderson and Many-Body Localization Transitions, *Phys. Rev. Lett.* **124**, 186601 (2020).
- [85] L. Zhang, V. Khemani, and D. A. Huse, A Floquet model for the many-body localization transition, *Phys. Rev. B* **94**, 224202 (2016).

- [102] L. A. Peña Ardila, M. Heyl, and A. Eckardt, Measuring the Single-Particle Density Matrix for Fermions and Hard-Core Bosons in an Optical Lattice, *Phys. Rev. Lett.* **121**, 260401 (2018).
- [103] F. Evers and A. D. Mirlin, Fluctuations of the Inverse Participation Ratio at the Anderson Transition, *Phys. Rev. Lett.* **84**, 3690 (2000).
- [104] K. S. Tikhonov and A. D. Mirlin, Many-body localization transition with power-law interactions: Statistics of eigenstates, *Phys. Rev. B* **97**, 214205 (2018).
- [105] D. J. Luitz, F. Alet, and N. Laflorencie, Universal Behavior beyond Multifractality in Quantum Many-Body Systems, *Phys. Rev. Lett.* **112**, 057203 (2014).
- [106] A. De Luca and A. Scardicchio, Ergodicity breaking in a model showing many-body localization, *Europhys. Lett.* **101**, 37003 (2013).
- [107] X. Yu, D. J. Luitz, and B. K. Clark, Bimodal entanglement entropy distribution in the many-body localization transition, *Phys. Rev. B* **94**, 184202 (2016).
- [108] V. Khemani, S. P. Lim, D. N. Sheng, and D. A. Huse, Critical Properties of the Many-Body Localization Transition, *Phys. Rev. X* **7**, 021013 (2017).
- [109] L. Herviou, S. Bera, and J. H. Bardarson, Multiscale entanglement clusters at the many-body localization phase transition, *Phys. Rev. B* **99**, 134205 (2019).
- [110] P. Naldesi, E. Ercolessi, and T. Roscilde, Detecting a many-body mobility edge with quantum quenches, *SciPost Phys.* **1**, 010 (2016).
- [111] M. Serbyn and D. A. Abanin, Loschmidt echo in many-body localized phases, *Phys. Rev. B* **96**, 014202 (2017).
- [112] J. Lee, D. Kim, and D.-H. Kim, Typical growth behavior of the out-of-time-ordered commutator in many-body localized systems, *Phys. Rev. B* **99**, 184202 (2019).
- [113] D. J. Luitz and Y. Bar Lev, Anomalous Thermalization in Ergodic Systems, *Phys. Rev. Lett.* **117**, 170404 (2016).
- [114] M.V. Berry, Regular and irregular semiclassical wavefunctions, *J. Phys. A: Math. Gen.* **10**, 2083 (1977).
- [115] E. Canovi, D. Rossini, R. Fazio, G. E. Santoro, and A. Silva, Quantum quenches, thermalization, and many-body localization, *Phys. Rev. B* **83**, 094431 (2011).
- [116] W. Beugeling, R. Moessner, and M. Haque, Finite-size scaling of eigenstate thermalization, *Phys. Rev. E* **89**, 042112 (2014).
- [117] J. A. Kjäll, J. H. Bardarson, and F. Pollmann, Many-Body Localization in a Disordered Quantum Ising Chain, *Phys. Rev. Lett.* **113**, 107204 (2014).
- [118] B. Efron and G. Gong, A Leisurely Look at the Bootstrap, the Jackknife, and Cross-Validation, *Am. Stat.* **37**, 36 (1983).
- [119] J. M. Zhang and N. J. Mauser, Optimal Slater-determinant approximation of fermionic wave functions, *Phys. Rev. A* **94**, 032513 (2016).

-
- [120] J. M. Zhang and M. Kollar, Optimal multiconfiguration approximation of an n -fermion wave function, *Phys. Rev. A* **89**, 012504 (2014).
- [121] H. Li and F. D. M. Haldane, Entanglement Spectrum as a Generalization of Entanglement Entropy: Identification of Topological Order in Non-Abelian Fractional Quantum Hall Effect States, *Phys. Rev. Lett.* **101**, 010504 (2008).
- [122] S. T. Bramwell, K. Christensen, J.-Y. Fortin, P. C. W. Holdsworth, H. J. Jensen, S. Lise, J. M. López, M. Nicodemi, J.-F. Pinton, and M. Sellitto, Universal fluctuations in correlated systems, *Phys. Rev. Lett.* **84**, 3744 (2000).
- [123] T. Antal, M. Droz, G. Györgyi, and Z. Rácz, $1/f$ Noise and Extreme Value Statistics, *Phys. Rev. Lett.* **87**, 240601 (2001).
- [124] E. Bertin, Global Fluctuations and Gumbel Statistics, *Phys. Rev. Lett.* **95**, 170601 (2005).
- [125] A. Lakshminarayan, S. Tomsovic, O. Bohigas, and S. N. Majumdar, Extreme Statistics of Complex Random and Quantum Chaotic States, *Phys. Rev. Lett.* **100**, 044103 (2008).
- [126] E. J. Gumbel, *Statistics of Extremes* (Columbia University Press, New York, 1958).
- [127] M. R. Leadbetter, G. Lindgren, and H. Rootzén, *Extremes and Related Properties of Random Sequences and Processes*, Springer Series in Statistics, Vol. 11 (Springer-Verlag, New York, Heidelberg, Berlin, 1983).
- [128] Z.-C. Yang, C. Chamon, A. Hama, and E. R. Mucciolo, Two-Component Structure in the Entanglement Spectrum of Highly Excited States, *Phys. Rev. Lett.* **115**, 267206 (2015).
- [129] S. D. Geraedts, R. Nandkishore, and N. Regnault, Many-body localization and thermalization: Insights from the entanglement spectrum, *Phys. Rev. B* **93**, 174202 (2016).
- [130] M. Serbyn, A. A. Michailidis, D. A. Abanin, and Z. Papić, Power-Law Entanglement Spectrum in Many-Body Localized Phases, *Phys. Rev. Lett.* **117**, 160601 (2016).
- [131] F. Pietracaprina, G. Parisi, A. mariano, S. Pascazio, and A. Scardicchio, Entanglement critical length at the many-body localization transition, *J. Stat. Mech.* **2017**, P113102 (2017).
- [132] R. Pal and R. Lakshminarayan, Probing the randomness of ergodic states: extreme-value statistics in the ergodic and many-body-localized phases, *arXiv:2002.00682* (2020).
- [133] S. N. Majumdar, A. Pal, and G. Schehr, Extreme value statistics of correlated random variables: A pedagogical review, *Phys. Rep.* **840**, 1 (2019).
- [134] S. T. Bramwell, J.-Y. Fortin, P. C. W. Holdsworth, S. Peysson, J.-F. Pinton, B. Portelli, and M. Sellitto, Magnetic fluctuations in the classical XY model: The origin of an exponential tail in a complex system, *Phys. Rev. E* **63**, 041106 (2001).
- [135] S. N. Majumdar and A. Comtet, Exact Maximal Height Distribution of Fluctuating Interfaces, *Phys. Rev. Lett.* **92**, 225501 (2004).

- [136] H. G. Katzgraber, M. Körner, F. Liers, M. Jünger, and A. K. Hartmann, Universality-class dependence of energy distributions in spin glasses, *Phys. Rev. B* **72**, 094421 (2005).
- [137] S. Hofferberth, I. Lesanovsky, T. Schumm, A. I. Imambekov, V. Gritsev, E. Demler, and J. Schmiedmayer, Probing quantum and thermal noise in an interacting many-body system, *Nat. Phys.* **4**, 489 (2008).
- [138] I. Lovas, B. Dóra, E. Demler, and G. Zaránd, Full counting statistics of time-of-flight images, *Phys. Rev. A* **95**, 053621 (2017).
- [139] Z.-C. Yang, A. Hamma, S. M. Giampaolo, E. R. Mucciolo, and C. Chamon, Entanglement complexity in quantum many-body dynamics, thermalization, and localization, *Phys. Rev. B* **96**, 020408 (2017).
- [140] G. Györgyi, N. R. Moloney, K. Ozogány, Z. Rácz, and M. Droz, Renormalization-group theory for finite-size scaling in extreme statistics, *Phys. Rev. E* **81**, 041135 (2010).
- [141] P. J. Forrester and E. M. Rains, Jacobians and rank 1 perturbations relating to unitary Hessenberg matrices, *Int. Math. Res. Not.* **2006**, 48306 (2006).

Popular scientific summary

From everyday experience, it is clear that most objects obey the laws of thermal physics. A famous example is a metal rod of which one side is heated up, while the other one is cooled down. When the temperature difference is not maintained actively, the rod will eventually acquire an intermediate temperature homogeneously. Such behaviour is known to occur when the object obeys some rather generic physical properties.

Many-body localization is a phase of matter that avoids thermalization. In a many-body localized phase, interacting particles act as being non-interacting due to a quantum-mechanical interference effect. Many-body localization was discovered around 15 years ago and has been actively investigated ever since. This dissertation discusses a number of explorations on many-body localization.

The first study (discussed in chapter 4) is concerned with energy levels. The distribution of spacings between energy level provides a convenient probe to discriminate thermalizing from localized quantum systems. Here, the focus is on the intermediate statistics for systems that are neither thermal nor many-body localized. These statistics are shown to be well described by the Gaussian beta ensemble, an interpolating scheme known from the mathematical discipline random matrix theory.

The second study (discussed in chapter 5) discusses the spectral form factor, which is a quantity that can be used to discriminate between localized and delocalized systems. It is argued that the conventional interpretation can be affected by a constraint imposed by the value of the probability that two energy levels are infinitesimally close to each other. An alternative way of interpreting the spectral form factor is proposed.

The third study (discussed in chapter 6) focuses on eigenstates. Inspired by a previously initiated line of research, it is investigated how well eigenstates of the system can be mapped onto eigenstates of a non-interacting system. Many-body localization is observed in disordered systems for which the disorder is sufficiently strong. The main result is the observation of signatures of localization at a disorder strength in which the model is typically considered as thermal.

The last study (discussed in chapter 7) is about entanglement of eigenstates. Loosely speaking, entanglement defines the degree of ‘quantumness’ of a state. The more entanglement, the less well a state can be described by classical physics. Entanglement of a state is fully characterized by the entanglement spectrum. It is shown that the distribution of the smallest elements – carrying the largest physical weight – obey Gumbel statistics. These statistics originate from the field of extreme value statistics, and have been observed for a wide range of physical phenomena.

Polulair-wetenschappelijke samenvatting

De thermische fysica is van toepassing op de meeste alledaagse voorwerpen. Een bekend voorbeeld hiervan is een metalen staaf die aan de ene kant wordt opgewarmt en aan de andere kant wordt afgekoeld. De staaf zal, wanneer het verschil in temperatuur niet actief in stand wordt gehouden, na verloop van tijd homogeen dezelfde temperatuur aannemen. Dit verschijnsel kan worden waargenomen wanneer een object bepaalde, vrij generieke eigenschappen heeft.

Localisatie van deeltjes met wisselwerking ('many-body localization') is een toestand waarin geen themalisatie plaatsvindt. Als gevolg van een kwantummechanisch interferentie-effect gedragen wisselwerkende deeltjes in een dergelijke fase zich alsof ze onafhankelijk van elkaar zijn. Localisatie van deeltjes met wisselwerking is circa 15 jaar geleden ontdekt en is sindsdien onderwerp van veelvuldig onderzoek. Dit proefschrift behandelt een aantal studies naar dit verschijnsel.

Het is bekend dat de verdeling van afstanden tussen energieniveaus indicatief is voor of een systeem wel of niet thermaliseert. De eerste studie (besproken in hoofdstuk 4) richt zich op de verdeling voor systemen die noch thermisch, noch gelocaliseerd zijn. Deze 'tussen-statistiek' blijkt goed te kunnen worden beschreven door het Gaussische beta-ensemble, bekend uit de tak van de wiskunde die zich bezighoudt met toevalsmatrices.

De 'spectral form factor' is een grootheid die gebruikt kan worden om gelocaliseerde van gedelocaliseerde systemen te onderscheiden. In de tweede studie (besproken in hoofdstuk 5) wordt beargumenteerd dat de conventionele interpretatie gevoelig is voor de kans dat twee energieniveaus zich infinitesimaal dicht bij elkaar bevinden. Er wordt een alternatieve manier van interpreteren voorgesteld.

De derde studie (besproken in hoofdstuk 6) richt zich op eigentoestanden. Onderzocht wordt in hoeverre de eigentoestanden van een systeem in een gelocaliseerde toestand voor deeltjes met wisselwerking kunnen worden beschreven als een gelocaliseerde toestand voor onafhankelijke deeltjes. Het resultaat hint op het optreden van niet-triviale verschijnselen voor systemen die noch thermisch, noch gelocaliseerd zijn.

De laatste studie (besproken in hoofdstuk 7) richt zich op de mate waarin eigentoestanden verstrengeld zijn, wat wordt beschreven door het 'entanglement spectrum'. Deze studie laat zien dat de kleinste (fysisch belangrijkste) elementen van deze spectra Gumbel-statistiek vertonen. Dit resultaat geeft een kwantitatieve, parameter-vrije karakterisering van eigentoestanden van gelocaliseerde, wisselwerkende systemen.

Acknowledgements

This dissertation marks the end of an interesting and exciting journey. Here, I would like to speak out my gratitude to a number of people who made this possible, both scientifically and non-scientifically.

In the first place, I would like to thank my supervisors Vladimir Gritsev and Vadim Cheianov for their guidance, help, and freedom to pursue my own interests. For both, your encyclopedic knowledge of physics and critical eye has been of inevitable value. I feel privileged to be part of your groups, and will certainly miss the great atmosphere. I hope we can keep collaborating in the future.

Next, I would like to thank the current and former members of the condensed matter theory group for their collegiality and conviviality. Bernard, Edan, Jasper, Jean-Sébastien, Kareljan, Philippe, Vladimir, Alvis, Ananya, Axel, Corentin, Enej, Eoin, Jiří, Natalia, Neil, Piotr, Sangwoo, Sasha, Shan, Vincenzo, Ana, Bart, Bart, Boris, Daniel, Geert, Ido, Jans, Joris, Jorran, Koen, Luka, Moos, Patrick, Pieter, Rebekka, Robbie, Schelto, Sergio, Ward, and Yuan – thank you!

Over the last years, I have been visiting Leiden numerous times. I always felt very welcome there, in particular thanks to Aurélien, Cameron, Savvas, Tereza, and Yaroslav. I hope to see you again at a later moment.

Also in the role of teaching assistant, I have enjoyed my job. I would like to thank Eric Laenen, Erik Verlinde, Greg Stephens, Kareljan Schoutens, Jan de Boer, as well as my fellow assistants for the pleasant collaborations. In my role as thesis (co-)supervisor I would like to thank Han Peters and Jean-Sébastien Caux. Also, the (many) students who made this well-spent time receive acknowledgement.

Another shout-out goes to my office mates, who made a significant contribution to the joyful experience the last few years have been. In view of the ‘great lockdown’ the world is currently facing, I would like to mention the colleagues I should currently share the office with, Beatrix, Peng, and Vassilis.

Before concluding, I would acknowledge Rudolf Sprik. Rudolf, thank you for introducing me to quantum chaos, random matrix theory and everything related as a master student – looking back, this paved the way for this dissertation in many aspects.

Finally, I would like to thank the people who were involved in all this at a non-scientific level. First and foremost, this journey would not have been such great without my parents and brother. A final ‘thank you’ goes to the members of my beloved amateur orchestra for the pleasant weekly repetitions.

